The Pennsylvania State University

The Graduate School

College of Engineering

STRUCTURAL MODIFICATION OF NANOPOROUS CARBON WITH SINGLE WALL CARBON NANOTUBE

A Thesis in

Chemical Engineering

by

Bo Yi

© 2007 Bo Yi

Submitted in Partial Fulfillment
of the Requirements
for the Degree of

Doctor of Philosophy

August, 2007

The thesis of Bo Yi was reviewed and approved* by the following:

Henry C. Foley
Professor of Chemical Engineering
Thesis Adviser
Chair of Committee

Seong H. Kim
Assistant Professor of Chemical Engineering

Darrel Velogol
Associate Professor of Chemical Engineering

Elizabeth C. Dickey
Associate Professor of Materials Science and Engineering

Andrew L. Zydney
Professor of Chemical Engineering
Head of the Department of Mechanical Engineering

*Signatures are on file in the Graduate School.

Abstract

A novel CC nanocomposite was synthesized by pyrolysis of well dispersed individual functionalized SWNTs in a thermosetting resin, poly(furfuryl alcohol) (PFA). Strong interaction between SWNT and nanoporous carbon derived from PFA (PFA-NPC) was obtained with this strategy and the integrity of SWNTs was maintained after heat treatment.

Usually, it is challenging to separate SWNT bundles and disperse them in preparation of composites. 50 wt% SWNT/NPC composites prepared with solution blending showed mass transfer rate of ~140% higher than the original NPC. The improvement was not significant due to poor dispersion and the bundle structure of SWNTs. Functionalization of SWNTs successfully separated the SWNT bundles and solved the problems of dispersion. In this process, the SWNTs were first functionalized with sulfonic acid groups (SA-SWNT) on sidewall. Then they were converted to PFA-grafted SWNT (PFA-SWNT) by in situ polymerization of furfuryl alcohol (FA). NPC/SWNT nanocomposite was generated by pyrolysis of PFA-SWNT at 600˚C.

The structural transformation of NPC/SWNT at high temperature was studied by heating it at temperatures from 1200 to 2000 ˚C in vacuum and characterized with HRTEM and Raman spectra. It was found that NPC and SWNT coalesce upon heat treatment and NPC tended to graphitize along the axis of neighboring nanotubes at

temperature higher than 1400 ˚C. Complete graphitization of NPC and SWNTs was obtained at 2000 ˚C, when the NPC transformed to graphitic nanoribbons (GNRs) and SWNT or DWNT collapsed within the confines of the GNR.

The mass transfer rate in 0.05 wt% SWNT/NPC nanocomposite was ~2 times higher than that in the pure NPC. Similar improvement required SWNT concentration of ~60 wt% in the SWNT/NPC composites prepared by solution blending. SWNT/NPC nanocomposite fibers prepared from 0.1 wt% SA-SWNT/FA had ~13% increase of Young's modulus over the pure NPC fibers when they were pyrolyzed at 400 – 1600 ºC. The augment was slightly higher than Halpin-Tsai's model prediction for composites with randomly dispersed fibers, indicating that the strong interaction between NPC and SWNT strengthened the material.

TABLE OF CONTENTS

LIST OF FIGURES . . . . . ….... ix

LIST OF TABLES….. xv

ACKNOWLEDGMENTS…. xvi

Chapter 1 Introduction……. 1

1.1 Structure and applications of NPC . . . . ….……..... …...3

1.2 Properties of SWNT……. . . . . …. . . . ..…... 8

1.2.1 Discovery of SWNT . . . ..…..... …….. . . . . …..8

1.2.2 Structure and properties of SWNT……. ……. . . . …. . . . . ….. 9

1.2.3 Preparation of SWNT……..13

1.3 CC composites and graphitization of pyrolyzed PFA… ..…... . . . . ….14

1.3.1 CC composites……..……. ……. . . . …. 14

1.3.2 Graphitization of pyrolyzed PFA in CC composites….……..15

1.4 Preparation of SWNT composites and nanocomposites…... 16

1.4.1 Preparation of SWNT composites…… ……. . . . …. . . . . ….16

1.4.2 Preparation of SWNT nanocomposites…….……..19

1.5 Organization of the thesis……... 25

Chapter 2 General experiments and characterization methods……27

2.1 CH_3Cl adsorption…… . . . . ….……..... . . . . ….27

2.1.1 Apparatus…… . . . ..…..... …….. . . . . …27

2.1.2 Pore size calculation…….……. ……. . . . …. 28

2.1.3 Mass transfer rate and modeling..……32

2.2 Morphology and structures in nanoscale…… ..…... 39

2.2.1 TEM……..……. ……. . . . …. . . . . ……..40

2.2.2 SEM….…….……...41

2.3 Raman spectra…….…...…... . . . . ….42

Chapter 3 Synthesis of SWNT/NPC composites by dispersing SWNT in PFA solution…..… .. . . ….…..… 49

3.1 Introduction……. 49

3.2 Experiments……. . . . . …. 50

3.2.1 Preparation . . . . ……. . …. 50

3.2.2 Characterization……..…….51

3.2.3 CH_3Cl adsorption …….……. ……. . . . …. . . ……... 51

3.3 Results and discussions . . . . …. 52

3.3.1 SEM images. . . . . ……. . …. 52

3.3.2 TEM images. . . . . .. ……. . . . . …. . . . . ……... . 54

3.3.3 Raman spectra. . . . . ……. .. ……. . . . . …. . . . . …. 55

3.3.4 Pore size distribution (PSD)……..….……..57

3.3.5 Mass transfer rate……...……..64

3.4 Summary and conclusions……..……. 69

Chapter 4 Functionalization of SWNT and preparation of NPC/SWNT nanocomposite……...… 70

4.1 Introduction……. 70

4.2 Experiments……. . . . . …. 74

4.2.1 Materials. . . . ……. . . . . …….. 74

4.2.2 Purification of SWNT. . . . ……. . . . . …... 75

4.2.3 Functionalization of SWNT with sulfonic acid group.. 76

4.2.4 Synthesis of PFA-SWNT…….…….. 76

4.2.4 Synthesis of NPC/SWNT……..... 77

4.2.5 Characterization……..……..... 77

4.3 Results and discussions 79
4.3.1 Purification of HiPco SWNT. 79
4.3.2 Functionalization of SWNT with sulfonic acid group. 83
4.3.3 Synthesis and characterization of PFA-SWNT. 88
4.3.4 Synthesis and characterization of NPC/SWNT nanocomposite. 93
4.4 Summary and conclusions. 97

Chapter 5 Deformation of NPC/SWNT nanocomposite at high temperature. 98

5.1 Introduction. 98
5.2 Experiments. 101
5.2.1 Preparation. 101
5.2.2 Characterization. 101
5.3 Results and discussion 102
5.3.1 HRTEM images. 102
5.3.2 Raman spectra. 108
5.4 Summary and conclusions. 114

Chapter 6 Properties of SWNT/NPC nanocomposites prepared
with SA-SWNT 116

6.1 Introduction. 116
6.2 mass transfer rate in SWNT/NPC nanocomposites. 119
6.2.1 Preparation of SWNT/NPC nanocomposites. 119
6.2.2 CH_3Cl adsorption. 119
6.2.3 Results and discussion 119
6.3 Mechanical properties of SWNT/NPC nanocomposites. 126
6.3.1 Preparation of SWNT/NPC nanocomposite fibers. 126
6.3.2 Mechanical properties measurement. 128
6.3.3 Characterization. 128
6.3.4 Results and discussion. 128

6.4 Summary and conclusions……..……. 135

Chapter 7 Conclusions and future work…… … 136

BIBLIOGRAPHY…… 140

LIST OF FIGURES

Figure **1.1** Model of the structure of polymeric carbon. ……. 3

Figure **1.2** Schematic molecule structure of (a) FA (a); (b) linear PFA, and (c) crosslinking in PFA…….…4

Figure **1.3** Conceptual model of structural evolution of PFA-NPC……6

Figure **1.4** A structure model of PFA-NPC consisting of four layered turbostratic carbon sheets based on its PDF experiments. Typically 10 turbostratic carbon sheets were used to calculate the PDF…….....7

Figure **1.5** TEM image of CNT reported by Endo and coworkers in 1976…….....9

Figure **1.6** Three types of SWNTs formed by folding the graphene sheet along the different chiral vectors $\boldsymbol{C}_h$……10

Figure **1.7** TEM image of laser ablation prepared SWNT bundle……13

Figure **1.8** Schematic illustrations of (A) conventional; (B) intercalated; (C) ordered exfoliated; and (D) disordered exfoliated polymer–clay nanocomposite……20

Figure **1.9** (a) Functionalization of SWNTs with diazonium reagents in oleum. (b) Scheme of kinetic model displaying the reaction of 4-chlorobezene diazonium salt with a SWNT. There are three possible states of the diazonium reagent during the SWNT functionalization: (A) free diazonium salt in solution, (B) adsorbed on nanotube surface and (C) covalently bound to nanotube…...…….23

Figure **2.1** Scheme of the CH_3Cl adsorption apparatus…….27

Figure **2.2** Idealized geometry of slit-shaped pore…….....30

Figure **2.3** Scheme of mass transfer in NPC microdomain……33

Figure **2.4** Comparison of the LDF approximations with the exact solution of the pore model……..……37

Figure **2.5** signals generated when a high energy beam of electrons interacts with a thin specimen. The directions shown for each signal only indicate, in a relative manner, where the signal is strongest or where it is detected……39

Figure **2.6** Illustration of interaction volumes for various electron-specimen interactions. The secondary electrons emerge from depth of 50-500 Å……..40

Figure **2.7** Theoretically calculated Raman active mode eigenvectors and frequencies for a (10, 10) nanotube. The red arrows indicate the magnitude and direction of the appropriate C atom vibrations, and eigenvectors shown correspond to the seven most intense modes in Raman spectra. The unit cell is shown schematically in the upper right corner……...45

Figure **2.8** Revised Katauru plot based on experiment data of HiPco produced SWNT related the transition energy and the SWNT diameter. (+) and (-) refer to high and low energy transition respectively. v and c refer to valence and conduction band respectively…….……46

Figure **2.9** Raman spectra of NPC from pyrolysis of PFA at 600 °C. Excitation wavelength of 514.5 nm was used……48

Figure **3.1** SEM images of carbon derived from (a) PFA, (b) 14 wt% SWNT/PFA, (c) 39 wt% SWNT/PFA, (d) 50 wt% SWNT/PFA, (e) 80 wt% SWNT/PFA and (f) AP-SWNT (Scale bars 1μm)…….…...52

Figure **3.2** HRTEM images of (a) AP-SWNT and (b) 39 wt% SWNT/NPC composite. The arrows were pointed to the SWNT bundles covered with NPC. (Scale bars 25 nm)……54

Figure **3.3** Raman spectra of AP-SWNT (Carbolex) and the SWNT/NPC composites. The excitation wavelength is 1064 nm. The RBM intensities and G band intensities with respect to SWNT concentration in composite carbon are shown in the inset……56

Figure **3.4** PSD of (a) NPC-PFA, 14 wt% and 50 wt% SWNT/NPC composites; (b) 80 wt% SWNT/NPC composite and AP-SWNT……58

Figure **3.5** Ultramicropore (l < 0.7 nm), micropore (0.7 nm < l < 2 nm) and mesopore (2 nm < l < 50 nm)) volume evolution with SWNT concentration in composite carbons…….……59

Figure **3.6** Scheme of different adsorption sites on SWNT bundles: inside tube (A); interstitial channel (B); groove (C); and surface (D)……...60

Figure **3.7** Scheme of structure of (a) SWNT/NPC composite carbon with NPC and SWNT (b) as the major component……..……62

Figure **3.8** Normalized CH3Cl fractional uptakes in PFA-NPC, SWNT/NPC composites and AP-SWNT at 30 ºC and 40 mmHg……...……64

Figure **3.9** Fractional uptake of (a) PFA-NPC; (b) 14 wt% SWNT/NPC; (c) 50 wt% SWNT/NPC; (d) 80 wt% SWNT/NPC and (e) AP-SWNT fitted with barrier resistance model and to the pore resistance model respectively ……65

Figure **3.10** Evolution of pore mouth resistance kb versus the SWNT concentration in composite carbon……..…67

Figure **4.1** Scheme of functionalization of SWNT with sulfonic acid groups……...……73

Figure **4.2** Scheme of preparation of PFA wrapped SWNT (PFA-SWNT) and NPC/SWNT……...74

Figure **4.3** TPO of AP-SWNT, pre-SWNT and p-SWNT in flowing air……..79

Figure **4.4** DTPO of (a) AP-SWNT, (b) pre-SWNT, and (c) p-SWNT……81

Figure **4.5** HRTEM image of p-SWNT……82

Figure **4.6** Raman spectra of p-SWNT (a); p-SWNT treated with oleum only (b); SA-SWNT (c); SA-SWNT after annealing in Ar at 600°C for 1h (d). For comparison, all the spectra were normalized with their strongest G band and RBM were strengthened by 3 times……84

Figure **4.7** HRTEM image of SA-SWNT. Thin bundles of SWNTs with 2-4 nanotubes can be seen……..87

Figure **4.8** Photograph of (a) PFA-SWNT and (b) SA-SWNT in water. PFA-SWNT showed a clear supernatant and precipitate versus SA-SWNT with a dark supernatant due to dispersion and solubility. Water contact angles of (c) PFA-SWNT and (d) SA-SWNT Water contact angles of (c) PFA-SWNT and (d) SA-SWNT films……89

Figure **4.9** SEM image of membrane of (a) SA-SWNT and (b) PFA-SWNT……90

Figure **4.10** Raman spectra of PFA-SWNT. The spectra were normalized with the strongest G band and RBM were strengthened by 3 times……91

Figure **4.11** (a) IR spectra of p-SWNT (A), SA-SWNT (B) and PFA-SWNT (C); (b) expanded region of 3000~2800, highlighting the enhancement of C-H stretch; and (c) expanded region of 1200~1000, showing appearance of ether linkage and shift of sulfonic acid group stretch……92

Figure **4.12** Raman spectra of NPC/SWNT. The spectra were normalized with the strongest G band and RBM were strengthened by 3 times……93

Figure **4.13** HRTEM of SWNT/NPC nanocomposite (a) SWNT bundles covered with NPC (b) individual SWNT surrounded with NPC. The white triangles are pointed to the gap between NPC and SWNT……96

Figure **5.1** HRTEM image of PFA-NPC before HTT……..……102

Figure **5.2** HRTEM images of (a) pure NPC treated at 1200˚C; (b)-(d) NPC/SWNT treated at 1200˚C. The arrows are pointed to the graphene sheets derived from NPC oriented along the SWNT axis or circumference……..……..103

Figure **5.3** HRTEM images of NPC/SWNT treated at (a) 1400˚C; (b) 1600˚C; (c) 1800˚C and (d) pure NPC annealed at 1800˚C. The arrows are pointed to the multilayer carbon shells come from NPC graphitization….……..……..105

Figure **5.4** HRTEM images of (a) pure NPC and (b-d) NPC/SWNT each annealed at 2000 ˚C. The arrows are pointed to the “neck” between GNC and nanobulbs ……..……..107

Figure **5.5** Raman spectra of NPC/SWNT after HTT. All the spectra were normalized with the strongest G bands. The RBM features from metallic tubes and semiconducting tubes are marked as “m” and “s” respectively. RBM of NPC/SWNT treated at 2000 ˚C was not shown because it was too weak to recognize ……..……..109

Figure **5.6** Scheme of NPC/SWNT nanocomposite deformation under HTT…...……..115

Figure **6.1** Schematic structure of (a) NPC, (b) SWNT/NPC composite with SWNT bundle; and (c) SWNT/NPC nanocomposite with individual SWNT ……..118

Figure **6.2** (a) PSD and (b) cumulative pore volume of nanocomposite carbon prepared from SA-SWNT/FA and FA-NPC ……..120

Figure **6.3** Ultramicropore (l < 7 Å), micropore (7 Å < l < 2 nm) and mesopore (2 nm < l < 30 nm)) volume evolution with SWNT concentration in nanocomposite carbon prepared from SA-SWNT dispersed in FA ……...……..121

Figure **6.4** Normalized transient uptake $\frac{w(t)-w_{k-1}*}{w_k*-w_{k-1}*}$ of SWNT/NPC nanocomposite carbon and NPC-FA from 40 torr to 60 torr under 30 °C, where $w(t)$ was the uptake at time t, w_k* was the equilibrium uptake at 60 torr, $w_{k-1}*$was the equilibrium uptake at 40 torr. All of them were fitted with barrier model and the pore mouth mass transfer constant k_b versus SWNT concentration was shown in inset……..……..125

Figure **6.5** Scheme of preparation of SWNT/NPC nanocomposite fibers…….……..126

Figure **6.6** Typical stress-strain profiles of (a) PFA fibers and 0.1wt% SA-SWNT/PFA fibers cured at 100 °C; (b) PFA-NPC fibers and 0.1wt% SA-SWNT/NPC fibers pyrolyzed at 600 °C ……..129

Figure **6.7** Young's moduli of the NPC-PFA and 0.1% SWNT/NPC nanocomposite fibers pyrolyzed at different temperature. Sample prepared at 100 °C were PFA and SA-SWNT/PFA fibers. The enhancement of SWNT for the fibers pyrolyzed at 400 – 1600 °C is shown in the inset ……..130

Figure **6.8** SEM image of SA-SWNT/PFA nanocomposite fiber at the fracture cross-section……...……..131

Figure **6.9** HRTEM image of SWNT/NPC nanocomposite carbon. The white arrows were pointed to the finite graphitic domain and the nanobulb from collapsed SWNTs……..132

Figure **6.10** Fracture strength of PFA, SA-SWNT/PFA fibers cured at 100 °C, and NPC, SWNT/NPC nanocomposite fibers pyrolyzed at 300-600 °C ……..……..133

LIST OF TABLES

Table **1.1** mechanical and thermal properties of nylon 6 - clay composites……...20

Table **3.1** Mass transfer constant in SWNT/NPC nanocomposites……66

Table **4.1** Comparison of Raman factors of RBM of p-SWNT, annealed SA-SWNT and NPC/SWNT……...…..…….…..94

Table **5.1** Raman factors of tangential mode of NPC/SWNT treated at different HTT temperature ……...…..…….….112

ACKNOWLEDGEMENTS

This thesis is the result of five and half years of work. In this long journey, I have been supported by many people. They were accompanied with me not only in my final success, but also in the difficult exploring process. This project would not have been possible without their help and support. It is very pleasant for me to have the opportunity to express my gratitude to all of them.

At first, I would like to express the most sincere gratitude to my advisor, Professor Henry C. Foley, for his guidance during my research. His dense interest and enthusiasm in science had motivated all of his students, including me. He is a wealth of idea and creativity. His insights in carbon science had inspired many critical ideas in this project. Besides the guidance in research, I am also grateful to Dr. Foley for his encouragement and patience in my PhD program. It was his warm words that helped me to recover from the depression and resume the research when I was frustrated. He is a great friend for me to learn not only the research strategies, but also the life wisdoms.

I feel deep grateful to Dr. Ramakrishnan Rajagopalan, who promoted a number of valuable ideas in this project. He is the one who kept tracking the progress of the project and tried to make it keep going with faster paces. He was always available whenever I need advices and help. The extensive discussions with Ram covered almost every detail in this project.

I would also like to thank my many colleagues for creating an interacting and

enthusiastic research atmosphere. I am especially grateful to Kevin McNamara, Anna Merritt, Chris Burket, Pratik Mankidy, Billy-Paul Mathew Holbrook, and Krishna Dronavajjala. They gave me valuable comments and suggestions in my writing and presentations. We also shared lot of happy experiences like traveling, camping, dining, and even wine tasting trips…… I will always remember the happy days when we were together.

There are several people who deserve special thanks for providing help in the experiments outside of Foley's group. The Raman spectra in this project were taken in Professor Peter Eklund's group by Dr. Un Jeong Kim and Xiaoming Liu. I also learnt a lot about the spectra interpretation in the discussions with them. HRTEM was provided by MCL. Dr. Joe Kulik was always warmhearted to help me in HRTEM operations.

Finally, I would like to thank my family. Hao Cui, my husband, always supported me with his encouragement, patience, and hard working. Rosanne, my beloved daughter, made me start to feel the real preciousness and happiness of life. Her birth was one of the most important and joyful events in my life. My parents made a lot of efforts in my education. I am proud that I finally fulfill their dream. My in-laws have been affectionately taking care of my baby for a long time without any complain. I want to say thanks to all of them.

Chapter1

Introduction

Nanoporous carbon (NPC) is an amorphous carbon derived from controlled pyrolysis of synthetic or natural precursors. It has a narrow pore sizes distributed in the sub-nanometer range, which provides strong size and shape dependent effects in the diffusion and adsorption of small gas molecules. [1] The NPC derived from poly(furfuryl alcohol) (PFA-NPC) is a promising material for applications such as a catalyst support, [2-4] as a membrane, [5, 6] in the production of supercapacitors, [7] as well for deployment as binder in carbon/carbon (CC) composites. [8] This variety of potential and realized applications arises from PFA-NPC different properties including its microporosity, chemical inertness, thermal stability and mechanical properties. Modification of the NPC, e.g. its porosity, tendency to graphitization and, its molecular structure, is necessary for new and better applications for this carbon material.

As a new form of carbon receiving a great deal of interest for both of fundamental and applied research, carbon nanotubes (CNTs), especially single wall carbon nanotubes (SWNTs), have exceptional electronic [9] and mechanical properties [10], which make them attractive candidates as constituents of new high performance composites. [11, 12] Among the many kinds of composites that can be envisioned as having novel properties, CC composites consisting of SWNTs and carbon matrix are among the most intriguing. The combination of NPC with SWNT may not only produce a novel CC composite, but it also provide new insight into the nature of the interaction between two allotropes of carbon.

In this thesis, the SWNT/NPC composite and nanocomposite carbon with SWNT and NPC are prepared by solution blending and covalent functionalization of the SWNTs, respectively. Both of them were characterized to study the structural modification effect of SWNTs to the host material, NPC. The thermal deformation of the NPC/SWNT nanocomposite and the interaction between these two forms of carbon were studied after thermal processing in different temperature regimes in order to better understand the interaction at the interface between the two forms of carbon.

1.1 Structure and application of NPC

The nanoporous carbon (NPC) is globally amorphous but at the local level of tens of nanometers the feature of the structure are quite regular. This best demonstrated by the almost anomalously narrow pore size distribution typically centered around 0.5 nm. This is anomalous because unlike zeolites and other crystalline porous materials, the microporosity of most of the NPC does not arise from long-range order structures, but instead from the regular misalignment of aromatic microdomains as shown figure **1.1**. [8] The regularity in the misalignment results from the fact that the great majority of the carbon atoms present (>95 mol%) are in an sp2 trigonal configuration with small but real deviations around the bond angle (120º) and bond lengths for such carbon or carbon bonds.

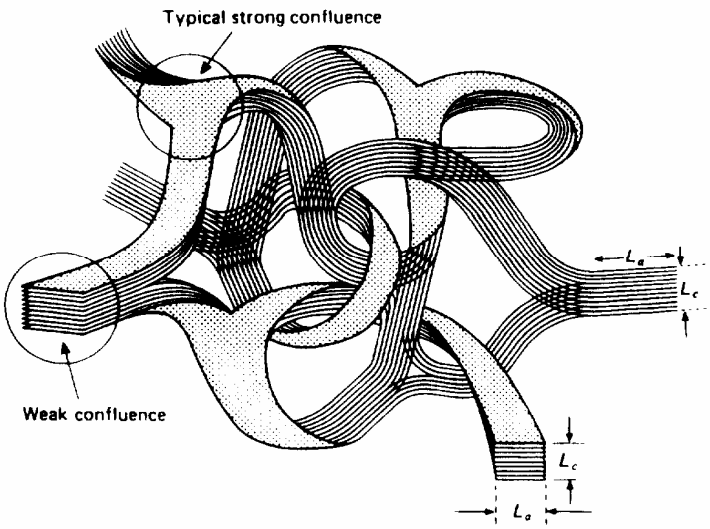

Figure **1.1** Model of the structure of polymeric carbon. (Adapted from [8])

Compared with zeolites, NPC is thermally more stable and it is inert to strong non-oxidizing acids and bases. [1] The narrow distribution of micropores of NPC gives rise strong variations in diffusion rates and extents of adsorption to molecules on the basis of their size and shape. Thus NPC provides kinetic separation of some gases. In such separations, the gases are discriminated on the basis of their global rates of adsorption rather than on the different extents of their degrees of equilibrium adsorption. An important commercial application of this property is the pressure swing adsorption (PSA) process for air separation. In this process, despite the fact that the extent of N_2 and O_2 adsorption at equilibrium are almost the same on NPC, N_2 can be effectively recovered from air because O_2 transport through the micropores with rates that are two or three orders of magnitude higher than those of N_2. [13]

The NPC materials are prepared by controlled pyrolysis of synthetic or natural precursors that generate solid that is mostly carbon. Synthetic precursors, including poly(acrylonitrile) (PAN), poly(vinylidene chloride) (PVDC) and PFA, can produce NPC with higher purity than that of natural precursors.[1] In this thesis, PFA has been used as the precursor for the NPC used to make SWNT/NPC composites and nanocomposites.

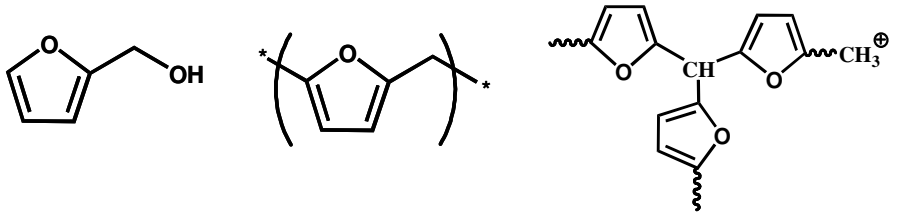

(a) (b) (c)

Figure **1.2** Schematic molecule structure of (a) FA; (b) linear PFA, and (c) crosslinking in PFA.

PFA is a thermosetting polymer derived from the acid-catalyzed condensation of furfuryl alcohol (FA) (figure **1.2**a). Cross-linking (figure **1.2**c) is an inevitable feature in the process of FA polymerization. The C-C bonds that make up the crosslinking are retained at very high temperature (>2000ºC) and the carbon derived from PFA is generally considered as "nongraphitizing" because highly ordered graphite cannot be obtained from it even after prolonged heat treatment at temperature as high as 2800 ˚C. [14, 15] Upon heating under inert gas (or vacuum) at 400-800°C, the polymer decomposes to give off H_2O, CH_4, CO_2, CO and H_2 to yield NPC solid. Mariwala and Foley described the pyrolysis and pore forming process of PFA-NPC (figure **1.3**). [16] In this process, a chaotic but not truly amorphous (i.e. full random) structure consisting of amorphous carbon and some aromatic microdomains is formed at low temperatures of 200-500 °C, leading to mesopores formation. When PFA is pyrolyzed at higher temperatures (600-800 °C) and/or for a longer time, the aromatic microdomains become larger in size by forming a slightly more ordered structure in the short range, but the PFA-NPC is still highly disordered over the long range. As the pyrolysis temperature increases to above 1200 °C, aromatic microdomains continued to grow and rearranged to more ordered and more densely packed structures; meanwhile, the micropores resulting from the spacing between aromatic microdomains starts to collapse.

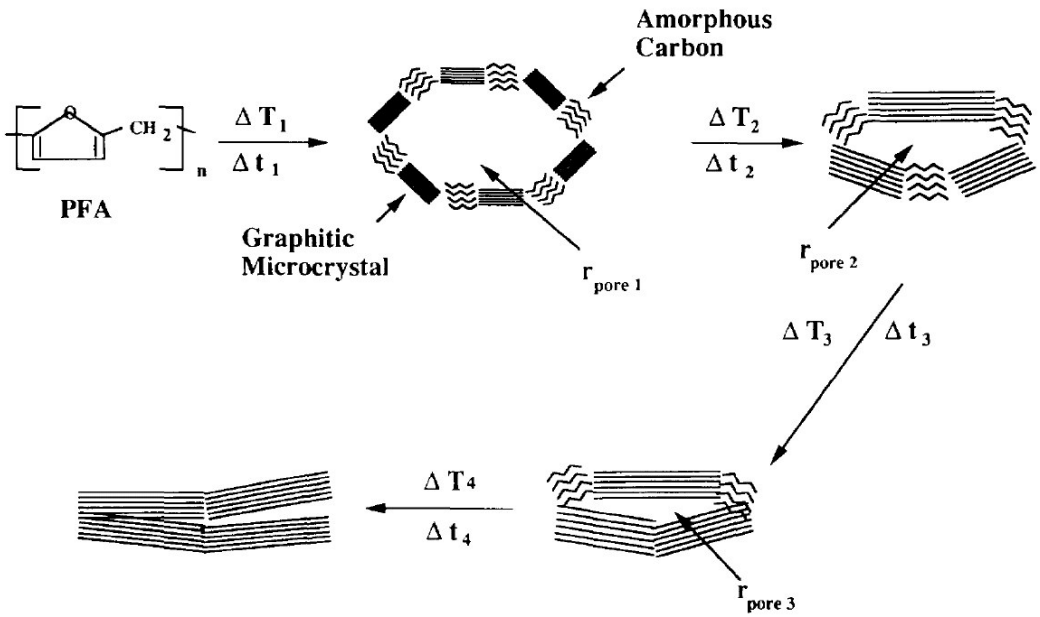

Figure **1.3** Conceptual model of structural evolution of PFA-NPC. [16]

The high-resolution transmission microscopy (HRTEM) images reveal that the carbon prepared at 600-800 °C has a network of layered and corrugated domains with spacing between 3.7-5 Å, which is higher than that of graphite (3.35 Å). [17] According to the IUPAC standard, pores are classified into 3 categories, namely micropore (l < 2 nm), mesopores (2 nm < l < 50 nm) and macropores (l > 50 nm). These spacing between the curved domains create the micropores in NPC which have a narrow pore size distribution and a mode of about 4.8 Å. [18] The structure model of PFA-NPC based on its pair distribution function (PDF) is shown in figure **1.4**, which it is composed of misaligned layers of curved graphene carbon sheets. This structure is consistent with the HRTEM observations. [19]

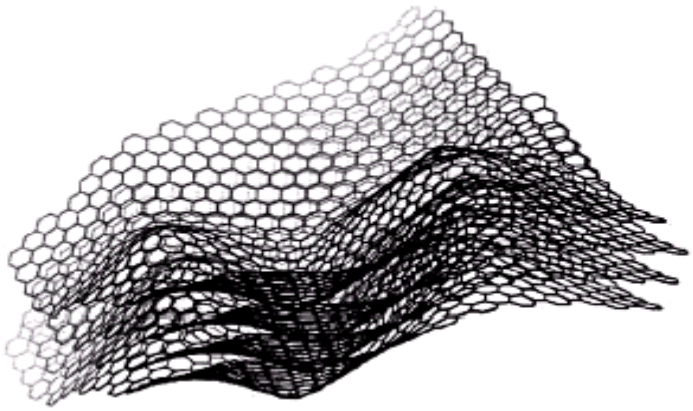

Figure **1.4** A structure model of PFA-NPC consisting of four layered turbostratic carbon sheets based on its PDF experiments. Typically 10 turbostratic carbon sheets were used to calculate the PDF. (Adapted from [19])

PFA-NPC has been widely investigated for use as membranes, catalyst supports or even as a catalyst in its own right. An NPC membrane with very good small molecule discrimination properties can be prepared by carefully coating PFA onto a porous stainless steel support and pyrolysing. [5, 6] The PFA-NPC solid can be used as a catalyst support for metals, such as Pt, [2-4] Fe [20] and alkali metals [21]. PFA-NPC itself can also be used as a dehydrogenation catalyst to convert ethylbenzene to styrene. [22] Due to its high apparent surface area arising from its microporosity, PFA-NPC has potential for application as supercapacitors. [7] But these applications can be limited by the low mass transport rates into and out of the micropores. Thus research in this thesis has focused on modifying the structure of NPC for better mass transfer and wider application.

1.2 Properties of SWNT

Carbon nanotubes (CNTs) are a new form of carbon with very different structures from graphite and diamond. There are two types of CNTs, multi-walled carbon nanotube (MWNTs) and single walled carbon nanotube (SWNTs). A SWNT can be viewed as a seamless cylinder formed by rolling up a section of a graphene sheet and capped with a half fullerene molecule at each end. The MWNT is made of concentric cylinders with interlayer distance of 3.4 Å. This interlayer spacing is slightly larger than that of the single-crystal graphite (3.35 Å) because there is a severe geometrical constraint in MWNT in forming the concentric seamless cylinders.

1.2.1 Discovery of SWNT

In 1991, Iijima discovered a tubular graphitic carbon, which was later dubbed the MWNT. [23] This was formed in an arc-discharge stuck between a carbon cathode and anode, which produced carbon soot. The initial discovery was made by examination with transmission electron microscopy (TEM) of the solid deposited at the cathode. Later in 1993, Iijima's group [24] and Bethune's group [25] found SWNTs by the same methods, but they did so independently. These discoveries became the keystones of what we now call the field of nanotechnology. However, the observation of CNT can be traced back to a much earlier time. In a paper by Endo and coworkers in 1976, dramatically clear images of CNT were published (figure **1.5**). [26] Based on the diameter of these CNT and given that they were prepared in arc-discharge, it is highly likely that these were in fact the first clear images published of what later became know as MWNTs. In an even earlier paper in 1952 by Russian scientists, TEM images similar to those of CNT were also

reported. [27] Unfortunately, due to the low resolution of the images, none of these authors realized the special tubular structure of these carbons and missed the chance to claim to discover this new form of carbon. Therefore the plethora of experimental and theoretical studies of CNT that has taken place over the last 15 years started only after Iijima's discovery.

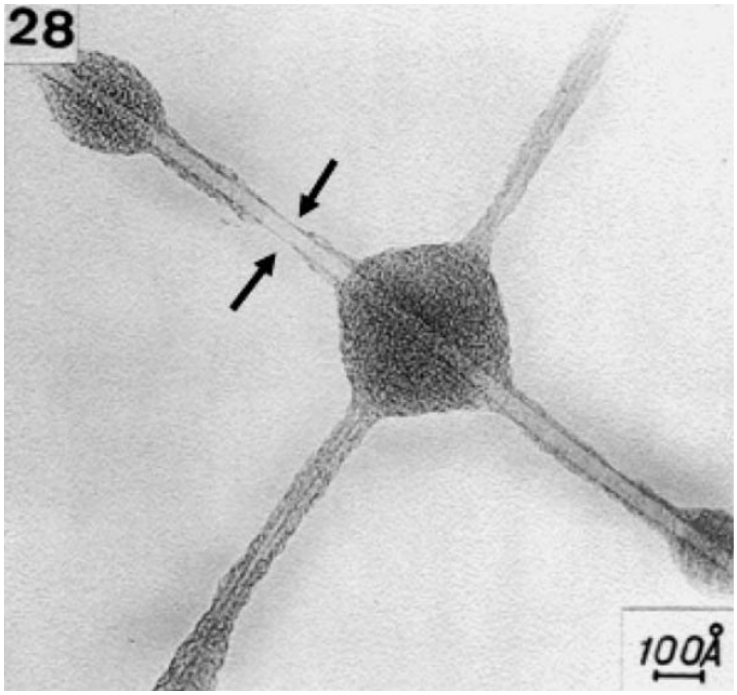

Figure **1.5** TEM image of CNT reported by Endo and coworkers in 1976. (Adapted from [26])

1.2.2 Structure and properties of SWNT

The CNTs have many unique properties due to their special dimensional, structural and topological configuration. The perfect alignment of the C-C bond lattice along the tube axis and the closed topology endows CNTs with in-plane properties of graphite such as high conductivity, chemical inertness, as well as excellent strength and

stiffness. Theory and some experimental results showed that individual SWNTs have very high Young's moduli (640 GPa - 1 TPa) [28-30] and tensile strengths (150 -180 GPa) [31].

A SWNT may have various electronic properties based on its chiral vectors, along which the graphene sheet is folded (figure **1.6**). The chiral vector $\boldsymbol{C}_h = n\mathbf{a}_1 + m\mathbf{a}_2$, where $\mathbf{a}_1$ and $\mathbf{a}_2$ are the graphene primitive vectors and n, m are integers. $\boldsymbol{C}_h$ is generally written as (n, m).

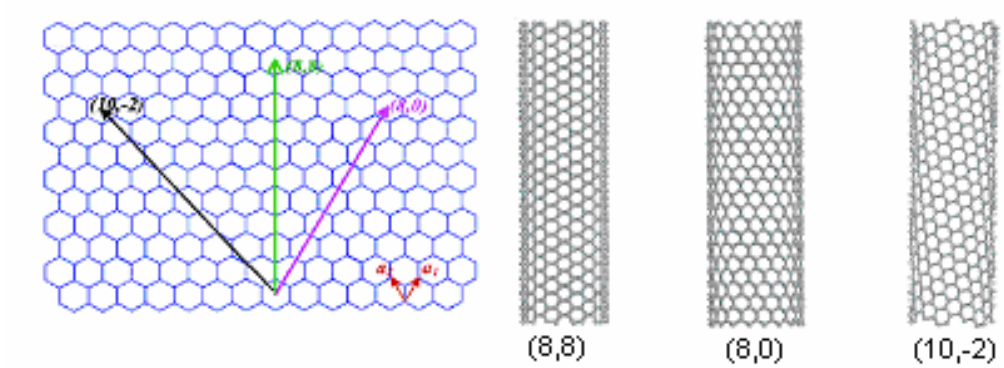

Figure **1.6** Three types of SWNTs formed by folding the graphene sheet along the different chiral vectors $\boldsymbol{C}_h$. (Adapted from [32])

The SWNT diameter d_t can be calculated from the integers n and m as

$$d_t = \frac{C_h}{\pi} = \frac{\sqrt{3\left(m^2 + mn + n^2\right)} \cdot a_{CC}}{\pi} \qquad (\mathbf{1.1})$$

where a_{CC} is the nearest neighbor C-C distance, and C_h is the length of the chiral vector $\boldsymbol{C}_h$. It is usually assumed that SWNT has the same C-C bond length as that of graphite, in which a_{CC} is 1.421 Å. But for a very small SWNT, e.g. a (4, 2) SWNT, calculation of the C-C bond length is necessary due to the high degree of curvature of graphene sheet. [33]

With various chiral vectors, three types of SWNT are formed: "Armchair" formed by folding along (n, n), "zigzag" formed along (n, 0) and chiral SWNT formed along (n, m) ($n \neq m$) as shown in figure **1.6**. [32] Theoretical calculation and STM experiment results show that the SWNT can be either metallic when (n-m)/3 is an integer or semi-conductive when (n - m)/3 is not an integer. [34] However, due to the curvature effect, only the armchair SWNTs are truly metallic, while chiral and zigzag SWNTs with integer (n - m)/3 are metallic at room temperature, but exhibit a very small chirality-dependent energy gap at lower temperatures. [35] Usually these SWNTs are called semi-metallic to differentiate them from metallic SWNTs.

Metallic SWNTs behave as coherent quantum wires since they can transport electrons over long distance without significant scattering and the mean free path in these systems is on the order of microns. [9] The phonon transfer mean free path in SWNT is also high, resulting in a high thermal conductivity of ~6600 W/(m·K) based on theoretical calculations. [36]

Similarly, some theoretical calculations and experiments showed high mass transfer rate through CNT due to the super smooth channels inside SWNT. Skoulidas et al used atomic simulations to predict the diffusive transport rate of CH_4 and H_2 and found the molecular fluxes through SWNT orders of magnitude greater than crystalline zeolites with comparable pore size. [37] They considered the rapid transport of adsorbed gases in SWNTs to arise from the smoothness of the potential energy surface in SWNTs and not strongly dependent on the details of the adsorbate-adsorbent interaction potentials. They also simulated the diffusion of Ar and Ne through SWNT and found the self-diffusivities are one to three orders of magnitude faster in SWNT than in silicalite, depending on

loading. [38] The fluxes of both Ar and Ne are four orders of magnitude greater through CNT membranes than through silicalite membranes of the same thickness. Experimentally, Holt et al fabricated micro-membranes in which aligned CNTs with diameters of less than 2 nm serve as pores and found the gas and water permeability through the membrane are more than three orders higher than the commercial polycarbonate membranes. [39] In addition, the nanosize of CNT, especially SWNT, provides a large surface area. All of these properties are interesting because they suggest novel behavior in applications such as gas adsorption and catalyst supports etc.

Currently, most studies on SWNT composites are focused on the improvement of mechanical, electrical and optical properties. However, using SWNT to improve mass transfer properties has not been reported yet. Since SWNT show improved rates of diffusion and adsorption, it is reasonable to expect it may provide some improvement in mass flux and adsorption capacity in SWNT/NPC nanocomposites.

1.2.3 Preparation of SWNT

SWNTs are mainly prepared by electric arc discharge, [40] laser ablation [41] and chemical vapor deposition (CVD) [42]. Arc discharge and laser ablation methods involve the evaporation of solid carbon source, usually graphite, and condensation of gaseous carbon atoms on metal catalysts. Carbolex Inc. (Broomall, PA) produces SWNTs by the electric arc discharge method with a Ni-Y catalyst. In the CVD process, a catalyst is used to decompose the gaseous carbon source, usually hydrocarbons or CO, into CNTs. Compared to other methods, CVD is better for large scale production because the process is more controllable and the catalysts are less expensive. Carbon Nanotechnology Inc.

(CNI, Huston, TX) produces SWNT with high pressure CO decomposition, a process known as HiPco.

The as-prepared SWNTs are a mixture of SWNTs with different charalities, diameters and lengths together with some impurities of metals, amorphous carbon and graphitic carbon. The SWNTs are usually triangularly assembled in bundles that consist of several tens of nanotubes, as shown in figure **1.7**. [41] The diameter of the SWNT is ~1 nm with distance of ~0.34 nm between each. Theoretical calculations show that the van der Waals force between two neighboring SWNTs is ~950 eV/µm overlap length. [43] For a SWNT embedded in the bundle, the cohesive energy can be as high as 29 keV/µm. [44] The strong interaction between tubes makes it difficult to separate the bundle into individual SWNTs.

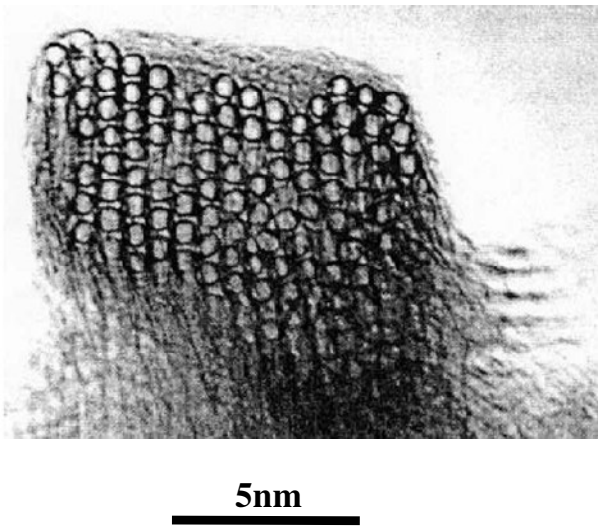

Figure **1.7** TEM image of laser ablation prepared SWNT bundle (adapted from [41])

1.3 CC composite and graphitization of pyrolyzed PFA

1.3.1 CC composites

CC materials are a class of composites similar to the graphite/epoxy family of polymer matrix composites, in which the carbon fibers derived from PAN, pitch, rayon and vapor grown are used to reinforce the brittle carbon matrix. They can be made into a wide variety of forms, from one-dimensional to n-dimensional, depending upon different arrangement and fabrication of carbon fibers in carbon matrix.

CC materials were first studied by NASA in 1953 and were used as high temperature materials in the leading edge of the wings and nose cap of the Space Shuttle orbiter. Due to their low specific weight, low thermal expansion, high thermal resistance and good strength retention at high temperature, CC composites have been widely used as electrodes in both steel making and aluminum production, as moderators for nuclear reactors, rocket nozzles and exhausts, as aircraft brakes, as catalyst support, as adsorbent and many other chemical and electrical applications. [45]

The carbon fibers have a range of Young's modulus of 200-700 GPa and tensile strength around 1.7-4.1 GPa which can be optimized to obtain desired properties in the composites. [45] The diameter of the fibers used in the typical CC composite is about ~10μm. Since the strength and stiffness of the CC composites is largely determined by the fibers' mechanical properties, their improvement required fillers with stronger mechanical properties. Due to their extraordinary properties and much smaller size than carbon fibers, SWNTs would be interesting to augment or replace carbon fibers with SWNT in CC composites to create a nanocomposite. [46]

However, compared with CNT/polymer composites, CNT/carbon composites

have not been extensively studied. One of the CNT/carbon composites was prepared by Andrews et al. They dispersed SWNT in isotropic petroleum pitch matrices to form NT composite carbon fibers. [47] The tensile strength, modulus and electrical conductivity of the host material were increased with adding SWNTs.

1.3.2 Graphitization of pyrolyzed PFA in CC composites

Preparation of SWNT/NPC nanocomposites may not only create a novel CC composite, but also make it possible to study the interaction of SWNT and NPC. Although PFA-NPC is a non-graphitizing carbon, because it cannot be completely graphitized even after prolonged heat treatment at 2800 °C, extensive graphitization below 2800 °C was observed when it was used as a continuous phase or binder phase in CC composite. [48, 49] These effects were highly localized at the boundary between the carbon fiber and PFA-NPC with basal planes along the carbon fiber axis. These orientation effects could be attributed to the stress and strain accumulation caused by large volume shrinkage during heat treatment. The graphitization of PFA-NPC forms an "inter-phase" adjacent to the fibers, which may provide significant effect on the mechanical properties due to efficient load transfer in the composite. [50] For the composite carbon with SWNTs, due to the much smaller size of SWNTs compared to typical carbon fibers, it would be interesting to learn if the interaction of SWNT and NPC would lead to similar templating effect.

1.4 Preparation of SWNT composites and nanocomposites

The CNTs can be prepared as composites with many materials, such as polymers, [51-53] ceramics, [54] metal, [55, 56] and colloidal dispersions [57] to enhance the mechanical, electrical, or optical properties of the host materials. The dispersion and alignment of CNT in the host materials and the interaction between them determine the properties, especially the mechanical and electronic properties, of the composites. [58]

Since PFA was to be used as the NPC precursor in this thesis, the preparation of the SWNT/PFA composites was the first challenge to be considered. The most important issue in the preparation of SWNT/PFA is the problem of how to obtain a uniform dispersion of the SWNT in the PFA polymer in order to develop a strong interaction between them. To find a solution to this problem, it is important to review the strategies deployed by previous researchers in the preparation of CNT/polymer composites and nanocomposites.

1.4.1 Preparation of SWNT composites

(a) Solution blending

The most commonly used approach to prepare SWNT composites is to force the dispersion of the SWNTs in a polymer solution by ultrasonication. A good solvent for preparation of the composite should be compatible with both the polymer and SWNT. Solvents with relatively good solubility for SWNT, such as toluene, [59] dimethylformide (DMF) [52], *o*-dichlorobenzene (DCB) [60] were frequently used. Chang et al blended PS/DCB and SWNT/DCB solution then cast the mixture in a dish and heat to remove solvent. [60] The SWNT/PS composites so obtained showed good improvement in electrical conductivity with a low percolation threshold of less than 0.3

wt%, indicating good dispersion of SWNT.

The advantage of solution blending is that a relatively homogeneous dispersion can be achieved, especially when the composites were made into thin films. The structures of SWNT and polymer usually do not change in the process of fabrication with this method. However, the SWNTs have very low solubility (<10 mg/L) in commonly used organic solvents, such as DMF and toluene. DCB is one of the best organic solvent for SWNT and the solubility of SWNTs in it is 95mg/L. [61] Such a low solubility make it impractical to use sufficient solvent volume to dissolve SWNTs in composite preparation. In most of the solution blending processes, SWNTs are made into suspension in solvent rather than solution. So the SWNTs always tend to agglomerate and settle as soon as the ultrasonication is discontinued. Additionally, the solvent removal step destabilizes the dispersion and causes further sedimentation of SWNTs, resulting in segregation from the polymer matrix and a diminished effect of the SWNT on the polymer in the composite.

(b) Melt blending

Melt blending is an alternative way to prepare SWNT/polymer composites for thermoplastic polymers, such as poly(methyl methacrylate) (PMMA). In this method heat and high shear forces are applied to disperse SWNT in polymer matrix. A small volume of solvent has been used in some instance to improve the dispersion. The solvent can readily evaporate in melting process without causing the segregation of SWNT from polymer.

The combination of solution processing and melt processing may improve both of

the dispersion and alignment of SWNTs in polymer. Haggenmueller et al prepared SWNT/PMMA composite films with the combination of two processes. [62] The composite films were first obtained by mixing SWNT and PMMA in DMF and drying. They were then broken and hot pressed repeatedly to obtain better mixing of the SWNTs and PMMA. Highly aligned SWNT in PMMA could be obtained after 25 melting steps. However, the combination process is not widely used because of its complexity.

Compared with solution blending, the melt blending is less effective in dispersion of nanotubes and this method is limited to low concentration because the high viscosities may limit shear at high nanotube loading. Additionally, it is not useful for thermosetting polymers like PFA.

(c) In situ polymerization under ultrasonication

In situ polymerization under ultrasonication is a better way to disperse CNT because the polymerization and agitation of CNT occur at the same time, which helps to prevent the nanotubes from segregating out of the polymer.

Park et al prepared SWNT/polyimide (CP2) composite films by in situ polymerization. [63] They blended the monomers, 1, 3-bis(3-aminophenoxy) benzene (APB) with a SWNT/DMF before adding the dianhydride, 2,2-bis(3,4-anhydro-dicarboxyphenyl) hexafluoropropane (6FDA) to start polymerization. A better dispersion of SWNT bundles in the polymer was achieved than direct mixing SWNT/DMF with CP2. The composite films showed electrical, optical and mechanical properties enhancement. Jia et al prepared MWNT/PMMA composites by using 2,2'-azobis-isobutyronitrile (AIBN) to open MWNTs's π-bonds of the CNTs to initiate reaction with

MMA. [64] In their work, a strong interaction between the MWNTs and PMMA was produced with the C-C bond between MWNT and PMMA, but the dispersion of the CNTs in the polymer is rather poor because the CNTs can only react with a limited number of polymer molecules and it might obstruct the further polymerization of MMA. So the mechanical properties of the composites are low.

Usually, a stronger interaction can be achieved through in situ polymerization than directly dispersing in polymer, but it requires that the CNT compatible with both the monomers and polymers. Here the dispersion of CNTs is a potential problem. Therefore, it is not applicable to all of the polymers. Also, since solvents are usually needed in this method, it also has the redistribution problem.

1.4.2 Preparation of SWNT nanocomposites

The as-prepared SWNT exist as bundles with strong affinity between the tubes. With methods discussed above focused on dispersing the SWNTs, but despite this the SWNT bundles were not effectively exfoliated (broken down to single tubes), so they were still present in the composites in the agglomerate forms.

The benefits of exfoliating SWNT bundles into individual tubes is obvious: (1) an effective improvement in properties should be achieved at lower loading levels; (2) the structure of the host material can be effectively modified in nanoscale with individual SWNTs. Currently there are not many convincing reports comparing the SWNT composites and nanocomposites, because the SWNT properties are varied from different preparation methods, different manufacturers, or even different batches from the same manufacturer. However, an analogue of SWNT/polymer composites, the clay/polymer

composites, clearly shows the effect of decreasing the size of fillers (Table **1.1**). The properties improvement of the composites of nylon 6 and clay nanocomposite make clear size effect. These remarkable properties enhancement of nanocomposites is the result of the changes in composition and structure at the nanoscale (figure **1.8**). Similarly, to distinguish the composites made with SWNT bundles and the composite with individual SWNTs, they will be called "composite" and "nanocomposite" respectively in this thesis.

Table **1.1** mechanical and thermal properties of nylon 6 - clay composites [65-67]

Composite type	wt% clay	Tensile strength (Mpa)	Tensile modulus (Mpa)	Impact (kJ/m^2)	HDT (°C) at 18.5 kg/cm^2
Pristine polymer	0	69	1.1	2.3	65
"Micro" (tactoids)	5.0	61	1.0	2.2	89
"Nano" (exfoliated)	4.2	107	2.1	2.8	145

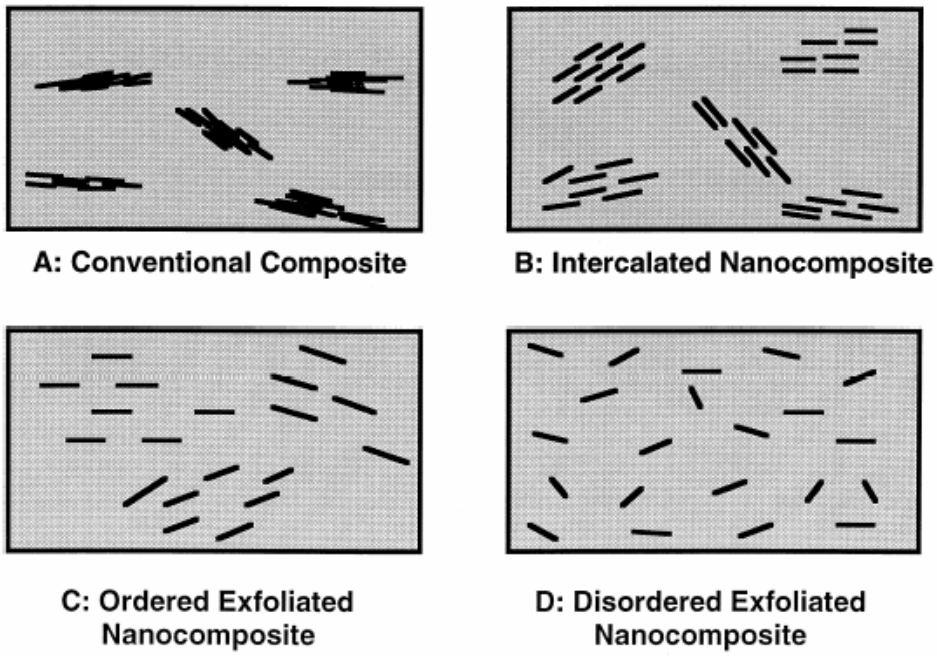

Figure **1.8** Schematic illustrations of (A) conventional; (B) intercalated; (C) ordered exfoliated; and (D) disordered exfoliated polymer–clay nanocomposite. (Adapted from [68])

Many chemists have explored several strategies to exfoliate the SWNT bundles into individual SWNTs in order to improve their solubility in solvents, especially in water, via covalent or noncovalent functionalization.

(a) Noncovalent functionalization

Noncovalent functionalization involves wrapping the SWNTs with polymers, surfactant molecules, or other forms of macromolecules. This strategy can preserve the unique physical properties of the SWNT.

Ionic surfactants have been widely used to disperse SWNT in water. [69, 70] Strano et al studied the process of SWNT dispersing in the sodium dodecyl sulfate (SDS) aqueous solution with Raman and fluorescent spectroscopy. [71] They described the mechanism of exfoliation as: the free SDS molecules promoted the formation of gaps or spaces at the bundle ends then the spaces propagated along the tube length, thereby the individual SWNT was separated from the bundle. Although isolated SWNTs were found in SDS solution, they were at very low concentration in equilibrium with the SWNT bundles. So the surfactant-assistant method has little value in preparing SWNT nanocomposites.

O'Connell et al. reported that SWNTs could be reversibly wrapped with a variety of linear polymers such as polyvinyl pyrrolidone (PVP) and polystyrene sulfonate (PSS) in water. [44] The wrapping may change the hydrophobic SWNT surface and exfoliated it from the bundle so that it could be soluble in water. Solubility in the g/L concentration range can be obtained with PVP wrapping.

Polysaccharides are another type of linear polymer that can wrap and solubilize individual SWNTs in water. Starch [72] and gum Arabic [73] have been reported to have

the ability to exfoliate and stabilize SWNTs.

Even though the noncovalent attachment does not alter the structure of the SWNTs, which is good, at the same time the interactions between the wrapping molecule and the nanotube are weak. Therefore, in a nanocomposite of this kind, the low load transfer efficiency between SWNT and polymer matrix would be poor. Additionally, only specific class of polymers, i.e. linear polymers, can be attached to the SWNTs with these strategies. It is not practical to prepare SWNT/PFA nanocomposite with this strategy because PFA is a hydrophobic crosslinking polymer.

(b) Covalent functionalization

Since the surface of a SWNT is highly inert, the covalent functionalization usually happens under severe conditions. The first reports about the SWNT covalent functionalization were under strong oxidative conditions. [74] For example, the mixture of sulfuric acid and nitric acid reacts with SWNTs to "open" their ends and generate functional groups, such as carboxylic acid, anhydride, quinone and ester groups at the ends. [75, 76] Interestingly, a similar reaction on MWNTs also happens during ultra-sonication. [77] These "defects" formation in such ways is helpful in solubilization of SWNTs by disrupting their inert surface. However, the distribution of the functional groups and the grafting density are not readily controlled in these oxidative processes.

Recently, several covalent strategies with specific functional groups and significant functionalization densities were reported, including fluorination with elemental fluorine, [78] ozonation, [79] cycloaddition with nitrene, carbene, or radicals, [80-82] Bingel reaction, [83] and electro-chemical reduction of diazonium salts [84-88]. Among all of these strategies, the method using diazonium salts as developed by Tour et

al could create aryl functional groups on the SWNT, which is quite interesting for eventual preparation of SWNT/NPC nanocomposites. By Tour's method, the diazonium reagents, generally produced by mixing of aniline with nitrite, react with SWNTs to functionalize the SWNT with aryl groups as shown in figure **1.9**. [86] Fuming sulfuric acid (oleum) was employed because SWNT can disperse in it as individual tubes with concentration up to 10 wt%.

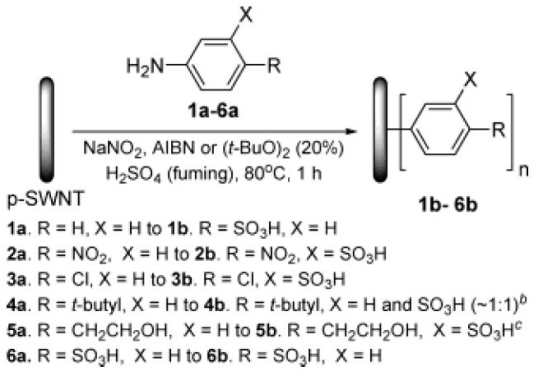

(a)

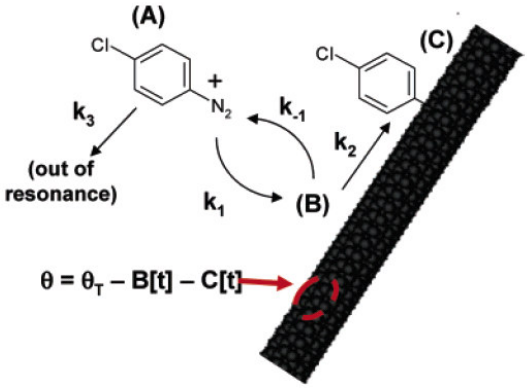

(b)

Figure **1.9** (a) Functionalization of SWNTs with diazonium reagents in oleum. [86]
(b) Scheme of kinetic model displaying the reaction of 4-chlorobezene diazonium salt with a SWNT. There are three possible states of the diazonium reagent during the SWNT functionalization: (A) free diazonium salt in solution, (B) adsorbed on nanotube surface and (C) covalently bound to nanotube. [89]

With covalent functionalization, the functional groups on SWNT can be designed to have good compatibility with the polymer matrix. This fabrication strategy also can be readily extended to a wide range of polymers. Additionally, covalent functionalization may effectively improve the interaction between SWNTs and polymer through bonding. Molecular simulations by Frankland et al indicated that the shear strength of the polymer-nanotube interface can be increased by over an order of magnitude with grafting density of only ~0.3%. [90] Experimentally, Geng et al used fluorinated SWNT to produce nanocomposite films with poly(ethylene oxide) (PEO). [91] The nanocomposite with 1 wt % fluorinated SWNTs (F-SWNTs) had 3 times higher yield strength than that of PEO and elastic modulus increased 45%. Gao et al. showed that the Young's modulus of nylon-6 fiber increase by 53% by adding 1 wt% carboxylic acid functionalized SWNT (SWNT-COOH). [92] The excellent mechanical properties enhancement came from the good dispersion and grafting of nylon chains on the SWNT. The monomer, caprolactam, was an excellent solvent for SWNT-COOH and this allows the effective dispersal of the SWNTs within it. Nylon chains were grafted to the SWNTs through condensation reactions between the carboxylic-acid group on SWNT and the terminal amine group of nylon chains, thus creating strong bonding between SWNTs and the polymer. In fact, at low SWNT loadings (<0.5 wt %) the experimental Young's moduli and the tensile strength of these composite nylon fibers were higher than the theoretical predictions for randomly dispersed composites. This suggested that the covalent bonding at the nanotube/polymer interface can be very effective in strengthening the material. Dyke et al fabricated poly (dimethyl-siloxane) (PDMS) composites with functionalized SWNT. [93] The functional group was designed to be compatible with the polymer matrix. The tensile

modulus and strength were significantly increased without obvious change in elongation at break.

In summary, covalent functionalization is of great interest in making SWNT/ polymer by designing the functional groups on SWNT compatible with polymer so that a high dispersion of SWNTs in polymer and strong bonding between them can be created. This strategy will be used in this thesis to prepare SWNT/NPC nanocomposites.

1.5 Organization of the thesis

The goal of this thesis is:

(1) To develop novel CC composites with SWNT and NPC;

(2) To prepare SWNT/NPC composites and nanocomposites, to compare their improvements in mass transfer and discuss the NPC structure change with SWNTs;

(3) To study the interaction between these two carbon allotropes in the novel CC nanocomposites.

In Chapter 2, the general experiments and characterization tools used to investigate the carbon materials are introduced. The pore structures of SWNT/NPC composites were probed with pore size distribution (PSD) and mass transfer rate. Their morphology and nanostructure were characterized with scanning electron microscopy (SEM) and transmission electron microscopy (TEM). Raman spectra were used as an important tool in studying the properties of carbon materials, especially SWNT.

In Chapter 3, SWNT/NPC composites prepared with solution blending were characterized with the methods introduced in Chapter 2. The structure of the composites

was discussed mainly based on the PSD and mass transfer rate evolution with respect to the SWNT concentration.

To exfoliate the SWNT bundles and enhance the interaction between SWNT and NPC, functionalization of SWNT was studied in Chapter 4. Arylsulfonic acid functionalized SWNT (SA-SWNT) was first prepared via the diazonium salt method. The PFA-grafted SWNT (PFA-SWNT) was fabricated by in situ polymerization of FA with the SA-SWNT as a catalyst. To study the interaction between NPC and SWNT, a NPC/SWNT nanocomposite was produced by pyrolysis of isolated PFA-SWNT. The thermal deformation of NPC/SWNT was studied in Chapter 5 to investigate if there is any templating effect of SWNTs on NPC graphitization as that of carbon fibers. In Chapter 6, the SWNT/NPC nanocomposites were produced by dispersing SA-SWNT in FA. How the SWNT change the mass transfer and mechanical properties of NPC with small doping amount is discussed.

Chapter2

General experiments and characterization methods

2.1 CH_3Cl Adsorption

2.1.1 Apparatus

The pore size distribution (PSD) and the mass transfer rate through the micropores are important properties of NPC and the SWNT/NPC composite carbons. Both of them can be obtained from CH_3Cl adsorption data. The scheme of the adsorption apparatus is shown in figure **2.1**.

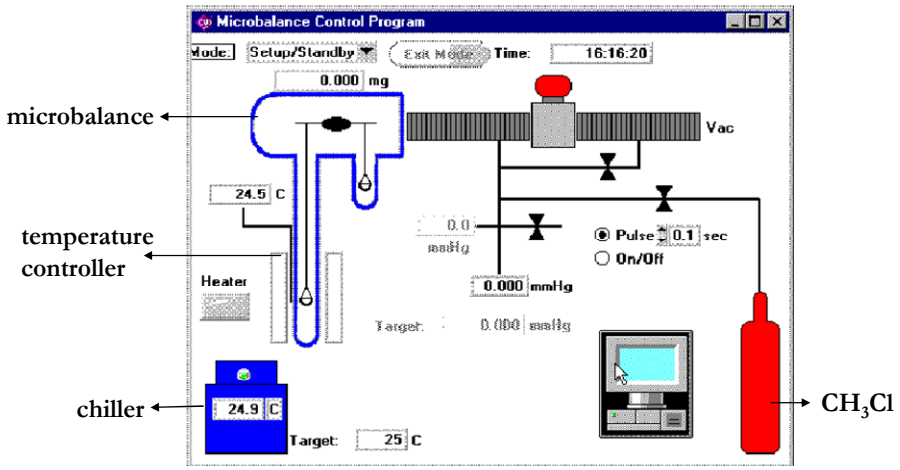

Figure **2.1** Scheme of the CH_3Cl adsorption apparatus.

The apparatus consists of a microbalance (MB-300), vacuum line, vent line, CH_3Cl line, a chiller and a computer to control temperature, pressure and record data. Prior to adsorption process started, the sample was loaded in the microbalance and degassed by pumping down and baking out at high temperature (~350 ºC) for 2-8 hours. The Auto Adsorption mode is used, in which the isotherm with a series of preset temperature (T) and pressure (P) is recorded. In this process, the isothermal conditions are achieved by pumping the liquid in the chiller tank (mixture of ethylene glycol and water) into the jacket outside of sample cell; the pressure was controlled by the valve in the CH_3Cl line, which is opened and closed by the computer. Once the equilibrium at a (T, P) point is obtained, the system proceeds to the next one until the program is completed. At the same time, the sample uptake was taken from the microbalance. With a series of adsorption equilibrium data, the pore size distribution (PSD) can be obtained. The details of PSD calculation will be introduced in section **2.1.2**.

2.1.2 Pore size calculation

The adsorption of gas molecules in a porous material occurs in several stages as the relative vapor pressure P/P_0 increases. When P/P_0 is very low, gas molecules are adsorbed in micropores and form 1-3 layers of adsorbed phase. Adsorption in mesopores happens when P/P_0 increases and the adsorbed material behaves like a liquid in a process termed “capillary condensation”.

For a specific relative pressure P/P_0, the pores with sizes below l_K will be filled at adsorption equilibrium. And the accumulative pore volume V_K (cc/g) of sizes below l_K can be calculated by

$$V_K = \frac{w_K}{\rho_K} \Big/ w_C \qquad \textbf{(2.1)}$$

where w_K is the mass uptake at equilibrium, which is measured with the microbalance; ρ_K is the density of the adsorbed phase, which can be taken as the density of the bulk liquid phase at that temperature; and w_C is the mass of the adsorbent. Assuming the PSD function to be $g(l)$, the relationship between V_K and l_K is

$$V_K = \int_0^{l_K} g(l)\,dl \qquad \textbf{(2.2)}$$

So we have

$$g(l) = \frac{dV}{dl} \qquad \textbf{(2.3)}$$

Practically, the PSD is calculated by

$$g(l_K) = \left.\frac{dV}{dl}\right|_{l=l_K} = \frac{V_K - V_{K-1}}{l_K - l_{K-1}} \qquad \textbf{(2.4)}$$

or PSD with unit of (cc/g) calculated by

$$\left.\frac{dV}{d\ln(l)}\right|_{l=l_K} = \frac{(V_K - V_{K-1})l_K}{l_K - l_{K-1}} \qquad \textbf{(2.5)}$$

when $l_K - l_{K-1}$ is reasonably small.

The pore size cannot be determined directly but rather it must be calculated from a model of the adsorbed phase in an ideal pore at fixed temperature, pressure and equilibrium. For carbons having pores less than 1 nm in dimension, their micropore sizes (<2nm) can be computed from each relative pressure by Horvath-Kawazoe (H-K) model. [94] In this model, the micropores are assumed to be slit-shaped as shown in figure **2.2**.

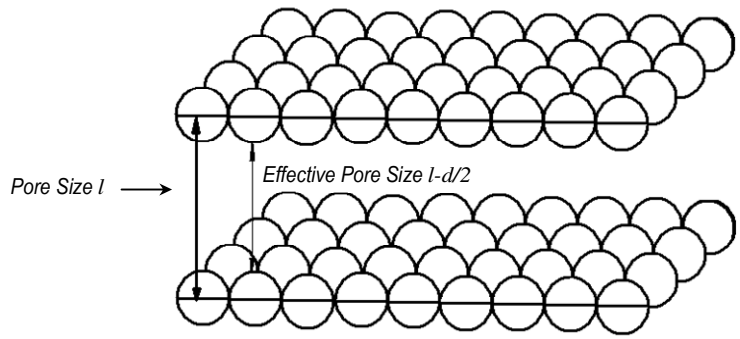

Figure **2.2** Idealized geometry of slit-shaped pore.

The free energy change upon adsorption in these pores is related to the adsorbent-adsorbate interaction energy, which is derived from 6-12 Lennard-Jones potential. An approximation in the model is that compared to the enthalpy of adsorption at equilibrium, the entropy term contribution is small enough in magnitude to be taken as negligible. Hence the free energy of the ideal adsorbed phase at a given micropore size l can be calculated by [94]

$$RT\ln\left(\frac{P}{P_0}\right) = N_{AV}\frac{N_a A_a + N_A A_A}{l-d}\left[\frac{1}{3\left(l-d/2\right)^3} - \frac{1}{3\left(d/2\right)^3} - \frac{\sigma^6}{9\left(l-d/2\right)^9} + \frac{\sigma^6}{9\left(d/2\right)^9}\right] \quad (\mathbf{2.6})$$

where P is the pressure at adsorption equilibrium; P_0 is the saturation pressure, which is a function of temperature; N_a and N_A are the area densities of adsorbate molecules and adsorbent molecules respectively; A_a and A_A are Kirkwood-Muller dispersion constants, which were related with the polarizability and magnetic susceptibility of both adsorbent and adsorbate; d is the diameter of the adsorbent atom, i.e. C atom; and σ is the L-J parameter.

The gas adsorbed in the mesopores (2 nm< l <50 nm) is treated differently; it is taken to behave as a "capillary condensed" phase. There is a condensed fluid meniscus formed in the pore which is in equilibrium with gas phase above it. The curvature of the pore can be calculated from the relative pressure by Kelvin equation. It relates the free energy change to the capillary condensation and calculates the pore radius r by

$$\ln\left(\frac{P}{P_0}\right) = -\frac{2\gamma \cdot V_L}{RT}\frac{\cos\theta}{r} \qquad (\mathbf{2.7})$$

where γ is the surface tension of the adsorbate, CH_3Cl, V_L is the molar volume of the liquid adsorbate, θ is the liquid-solid contact angle (assumed to be 0).

Thus, by taking a series of adsorption equilibrium data, the pore size at each point can be caulculated with a combination of the H-K model (Eq **2.6**) and the Kelvin model (Eq **2.7**) for mesopores (2 nm < l < 50 nm). The accumulative pore volume at corresponding pore size can be calculated from the mass uptake (Eq **2.1**).

For NPC and the composite carbons, the assumptions of H-K model are reasonable approximations because the micropores in the NPC are in fact approximately slit-shaped pores from HRTEM images. Also, since H-K model gives reliable PSD for SWNTs, [18] it can be considered as a reliable model for guiding the synthesis and characterization of the SWNT/NPC composites.

In the present experiments, CH_3Cl is used as adsorbate, instead of commonly used adsorbate, N_2. There are many advantages to use CH_3Cl compared with N_2 for PSD measurements. First of all, since CH_3Cl has much higher boiling point than N_2, P_0 is reasonably low at room temperature. Thus it becomes possible to measure the microporosity under room temperature and moderately low pressure, as well as the mesoporosity under moderately low temperature and sub-atmosphere. Generally the

ultramicropore and micropore size distribution can be obtained at 30 ºC and 3.5-200 torr, and mesopore size distribution can be obtained at -25 ºC and 200-600 torr with CH_3Cl adsorption. Experiments have shown these results were consistent with the PSD from N_2 adsorption under 77K. [18] Secondly, the mass transfer rates of CH_3Cl in these measurements are much higher than those of N_2 since it takes place at higher temperature. For some samples with negligible mesopores and macropores, e.g. NPC-PFA, the mass transfer of N_2 is too slow at 77K to probe the micropores, but with CH_3Cl the adsorption take place with relatively high transport rates and at moderate temperature making the approach to equilibrium in the micropores attainable in acceptable experimental time frames.

2.1.3 Mass transfer rate and modeling

Besides PSD, the microbalance system can also be used for adsorption rate, i.e. mass transfer rate studies. By setting the system at a certain temperature and pressure, and by recording the transient CH_3Cl uptake values, the adsorption rate can be obtained.

The NPC can be considered as numerous microdomains interconnected with some macropores, more or less depending on the synthesis method. [95-97] The mass transfer (net adsorption) rate in NPC is controlled by the transport through the narrow molecularly sized pores in the microdomains, and the resistance can be decomposed into two components: the barrier resistance confined at the micropore mouth and the pore diffusion resistance distributed in the micropore interior. The micropores of NPC were ink bottle shaped with narrow pore opening whose size is comparable to the molecular size, [1] so the pore mouth resistance is an important factor in mass transfer through

NPC. The micropores of NPC are originated from the spacing between the turbostratic layers. [19] There is considerable resistance for molecule diffusion in these pores due to the corrugated channels.

To develop a mass transfer model through NPC and SWNT/NPC, following assumptions are made

1) The NPC microdomains are spherical (figure **2.3**) and the SWNT/NPC composites have the similar microstructure. This geometric assumption is made because NPC microdomains have similar sizes in each dimension. It is also assumed that the micropores are evenly distributed and of the same dimension throughout the microdomain, i.e. a pseudo-homogeneous assumption which is a good one based on HRTEM images.

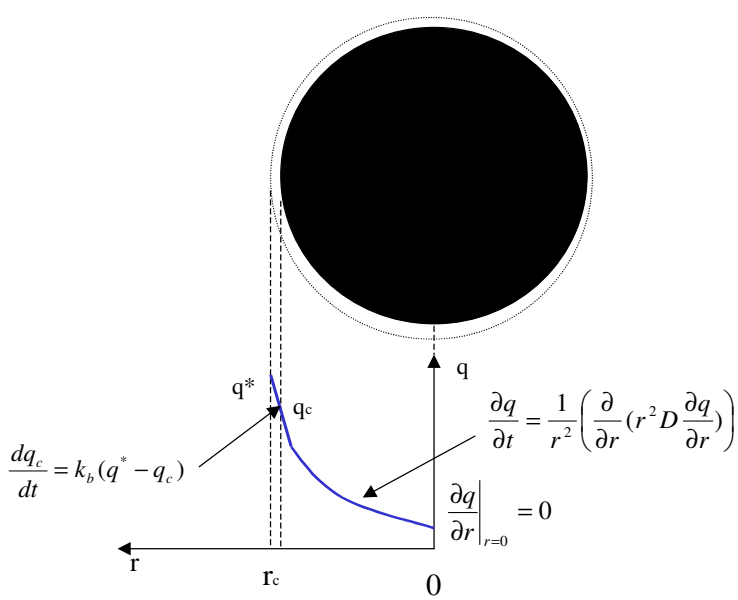

Figure **2.3** Scheme of mass transfer in NPC microdomain.

2) The mass transfer at pore mouth is modeled as thin film diffusion and can be described by

$$\frac{\partial \bar{q}}{\partial t} = k_b [q^* - q|_{r=r_c}] \qquad \textbf{(2.8)}$$

where k_b is the pore mouth mass transfer constant; q is the adsorbate concentration at time t with a distance r to the center of microdomain; q^* is the equilibrium adsorbate concentration, which is related with temperature and pressure only; r_c is the radius of the NPC microdomain, and $\bar{q}$ is the average adsorbate concentration, which is linearly correlated with the uptake of sample at time t, $w(t)$

$$\bar{q} = \frac{w(t)/M}{w_C} \qquad \textbf{(2.9)}$$

where M is the molecular weight of adsorbate.

3) There is no mass transfer at the center of NPC microdomain.

$$\left.\frac{\partial q}{\partial r}\right|_{r=0} = 0 \qquad \textbf{(2.10)}$$

4) There is no adsorbate on NPC when adsorption starts.

$$q|_{t=0} = 0 \qquad \textbf{(2.11)}$$

5) The mass transfer inside pores follows Fick's law.

Although the mechanism of diffusion in micropore is complex, it is practical to use Fick's law to describe the total flow through the NPC microdomain. [95, 96, 98] So the diffusion inside the NPC microdomain can be described as

$$\frac{\partial q}{\partial t} = \frac{1}{r^2}\left(\frac{\partial}{\partial r}(r^2 D \frac{\partial q}{\partial r})\right) \qquad \textbf{(2.12)}$$

where and D is the diffusivity inside NPC. In the spherical microdomain,

$$\bar{q} = \frac{3}{r_c^{\,3}} \int_0^{r_c} q \cdot r^2 dr \qquad \textbf{(2.13)}$$

To solve Eq **2.8** and **2.12**, two extreme cases are considered:

1. Barrier model

When the gas diffusion is controlled only by the barrier resistance, the resistance to gas molecule diffusion inside the micropores is considered to be much lower and hence the rate there is not limiting. Instead the diffusion experiences the highest resistance as it goes through the pore entrance, and q inside NPC microdomains tend to be uniform, hence

$$q\big|_{r=r_c} = \bar{q} \qquad \textbf{(2.14)}$$

Eq **2.8** becomes

$$\frac{d\bar{q}}{dt} = k_b (q^* - \bar{q}) \qquad \textbf{(2.15)}$$

Transform Eq **2.15** and integrate from 0 to t, the uptake change with time can be obtained

$$\ln\left(1 - \frac{\bar{q}}{q^*}\right) = -k_b t \qquad \textbf{(2.16)}$$

According to eq **2.9**, $\frac{\bar{q}}{q^*}$ is simply equal to fractional uptake $\frac{w(t)}{w*}$, where $w*$ is the equilibrium uptake. So the pore mouth mass transfer constant k_b can be obtained by fitting $\ln\left(1 - \frac{w(t)}{w*}\right)$ with respect to adsorption time.

2. Pore model

When the gas molecule transfers through the micropore entrance with much less resistance than it encounters when it diffuses inside the NPC micropores, then

$$q\big|_{r=r_c,\ \ t>0} = q^* \qquad \textbf{(2.17)}$$

With this boundary condition, the exact solution to Eq **2.12** can be obtained [98]

$$\bar{q} = q^* - 6q^* \sum_{n=1}^{\infty} \frac{1}{(n\pi)^2} \cdot e^{-(n\pi)^2 \frac{Dt}{r_c^2}} \qquad \textbf{(2.18a)}$$

or

$$1 - \frac{\bar{q}}{q^*} = 6 \sum_{n=1}^{\infty} \frac{1}{(n\pi)^2} \cdot e^{-(n\pi)^2 \frac{Dt}{r_c^2}} \qquad \textbf{(2.18b)}$$

By fitting the fractional uptake $\frac{w(t)}{w*}$ versus t with Eq **2.16** and Eq **2.18** respectively, one can tell whether the resistance at pore mouth or the diffusion inside micropores controls the mass transfer in NPC.

3. Combination of barrier model and pore model

In general conditions, the mass transfer may be controlled by both factors. A nearly exact solution of this case can be obtained by computer simulation, but this requires large amount of calculation; nearly as good a solution can obtained by a simple approximation. The so-called linear driving force (LDF) approach is often used to approximate the exact solution for pore diffusion [99] by imposing a quadratic form for the adsorbate concentration profile at time t:

$$q = a(t) + b(t)r^2 \qquad \textbf{(2.19a)}$$

A more generalized concentration profile is given by

$$q = a(t) + b(t)r^n \qquad \textbf{(2.19b)}$$

where n is an integer ≥ 2. The comparison of these approximations with the exact solution was plotted in figure **2.4**. It can be found that in short time range, the LDF approximation with high n is closer to the exact solution than with low n, but the low n value fits better at longer time range.

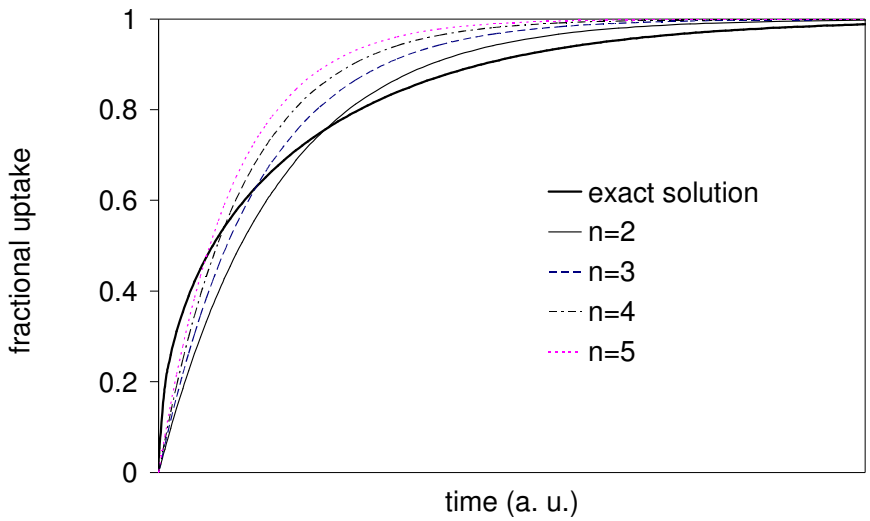

Figure **2.4** Comparison of the LDF approximations with the exact solution of the pore model.

From Eq **2.19b** and boundary conditions the concentration profile can be obtained

$$q = q^* - \frac{(n+3)}{n}[q^* - \bar{q}] \cdot [1 - (\frac{r}{r_c})^n] \qquad \textbf{(2.20)}$$

Combining Eq **2.20** and Eq **2.12**

$$\frac{\partial \bar{q}}{\partial t} = \frac{3(n+3)D}{r_c^{\,2}}[q^* - \bar{q}] \qquad \textbf{(2.21)}$$

Transforming Eq **2.21** and integrate from 0 to t leads to

$$\ln\left(1-\frac{\bar{q}}{q^*}\right)=-\frac{3(n+3)D}{r_c^{\,2}}t \qquad \textbf{(2.22)}$$

Assuming that the pore diffusion rate constant can be related to the diffusivity and microdomain radius as $k_p=\frac{3(n+3)D}{r_c^{\,2}}$, then an equation similar equation as Eq **2.16** can be obtained

$$\ln\left(1-\frac{\bar{q}}{q^*}\right)=-k_p t \qquad \textbf{(2.23)}$$

For the case that pore mouth resistance and micropore interior diffusion resistance are comparable, it is straight forward to show that

$$\ln\left(1-\frac{\bar{q}}{q^*}\right)=-\frac{t}{\frac{1}{k_b}+\frac{1}{k_p}}=k_t t \qquad \textbf{(2.24)}$$

where $\frac{1}{k_t}=\frac{1}{k_b}+\frac{1}{k_p}$.

Thus, with LDF approximation, the mass transfer rate of different materials can be compared based on $\ln\left(1-\frac{w(t)}{w^*}\right)$ and k_t.

2.2 Morphology and structures in nanoscales

When an electron beam interacts with a specimen, there are several secondary signals generated as shown in figure **2.5**. [100] These signals emerge from the sample within a few nanometers to several microns from the surface, depending on the beam parameters, e.g. energy, and sample properties, e.g. atomic number. The emerging signals can be detected with TEM, SEM, Raman spectroscopy, etc. and used to characterize the specimen.

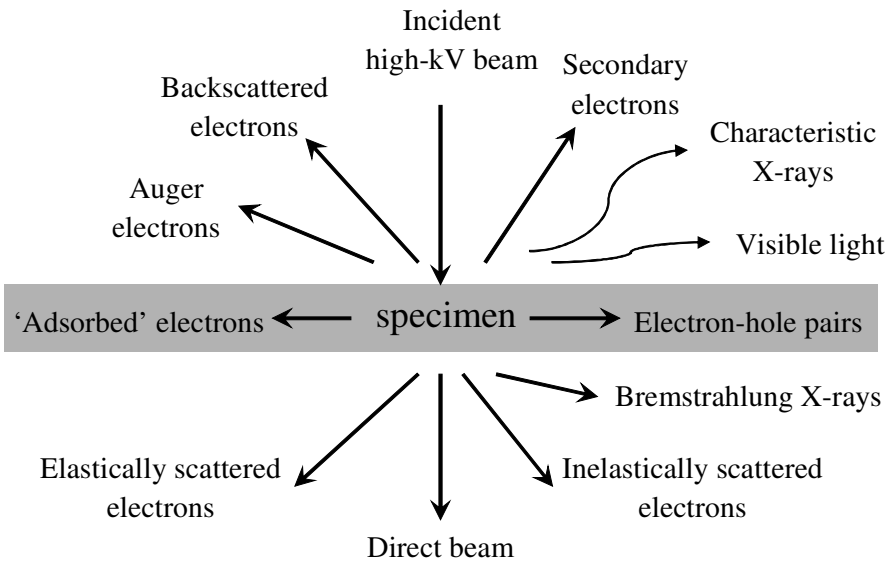

Figure **2.5** signals generated when a high energy beam of electrons interacts with a thin specimen. The directions shown for each signal only indicate, in a relative manner, where the signal is strongest or where it is detected. [100]

Based on the depth from which they emerge, the various signals have different interaction volumes arising from their different energy regimes as shown figure **2.6**. Some signals, such as Auger electrons and secondary electrons provide the information

from the sample surface only, while backscattered electron and characteristic X-rays can probe and provide information from much deeper within the sample.

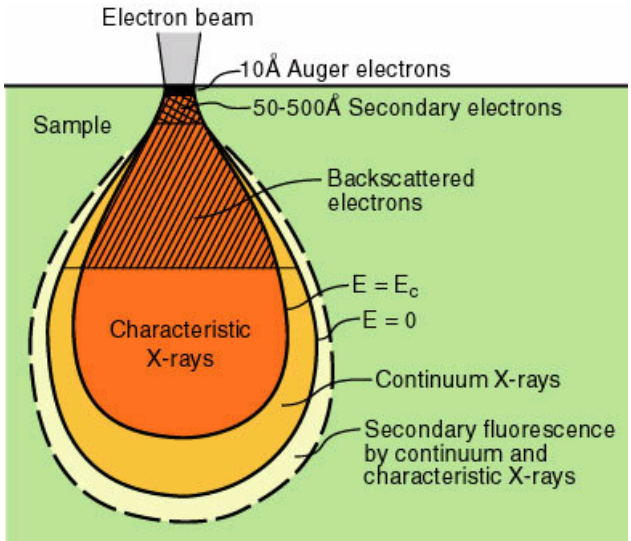

Figure **2.6** Illustration of interaction volumes for various electron-specimen interactions. The secondary electrons emerge from depth of 50-500 Å. [101]

In the present study, the morphology and nanostructure of NPC-PFA, SWNT, and their composites were characterized with transmission electron microscope (TEM) and scanning electron microscope (SEM).

2.2.1 TEM

Most of the secondary signals shown figure **2.5** can be detected by TEM with different operation modes. Information such as crystalline structures, defects, strain fields and chemical compositions at sub-nanometer length scales can be provided. In this thesis, the high resolution transmission electron microscopy (HRTEM) imaging was used. In this mode, the electron beam was generated from a LaB_6 or field emission electron gun

with high energy (generally 200 kV) and transmitted to the specimen through a series of electromagnetic lenses. In HRTEM mode, the electrons beam is broad and almost parallel in the plane of the specimen and transmitted through it. By adjusting the strength of intermediate lens and objective lens, the electron beam works in such a way that it projects the high resolution image of the specimen on the viewing screen with magnification of ~10^6.

Since the transmitted electrons are detected in HRTEM, the sample should be very thin, typically within tens of nm. Usually the SWNT samples can be prepared by dispersing them in organic solvent by ultrasonication, then dropping the suspension on the holey carbon-coated grids. Since NPC is a "hard" carbon and the crosslinking bonds cannot be broken by ultrasonication, preparation of the TEM sample requires that it ground with an agate mortar and pestle in an organic solvent to make a suspension of small particles. In this thesis, the HRTEM images were taken with a JEOL LaB_6 or JEOL 2010F operating at 200kV. The point to point resolution was ~2Å.

2.2.2 SEM

SEM was used to characterize the surface morphology of SWNT, NPC and their composites. In the operation of the SEM, a voltage between the sample and the filament is applied, resulting in electron emission for the filament, and the electrons are guided to the sample by a series of electromagnetic lenses in the electron column. To cause an effective electron emission, the sample is required to be conducting. Nonconductive specimens, e.g. NPC-PFA, are examined after coating with a thin layer (thickness < 20

nm) of Au by vacuum “sputtering” for less than 1 minute. The samples also require grinding for better focusing.

Secondary electrons are the most common signal used for investigation of surface morphology. They are produced as a result of the weakly bound electrons in the conduction band of the sample which is exited by the incident electron and then escapes from the sample surface. Since secondary electrons are low energy (<50eV), only those formed within the first few nanometers of the sample surface have enough energy to escape and be detected. Some backscattered electrons may also create secondary electrons which provide information from much deeper within the material. [102] The SEM image is the result of mapping the intensity of the secondary electron emission from the sample by scanning across the surface. The spatial resolution is mainly limited by the size of the electron probe. At the same time, the electric current density in the probe must be sufficient in magnitude to have the requisite signal to noise ratio. To optimize the resolution, a small but powerful electron probe is needed. The small objective aperture and short working distance are also use in imaging operations. In this thesis, the SEM images were obtained on a Hitachi S3000-H SEM operated under high vacuum and 5 kV.

2.3 Raman spectra

Raman spectra are collected by irradiating a specimen with a powerful laser source to generate Raman scattering. During a Raman scattering, an electron in the specimen is excited from the valence energy band to the conduction energy band by absorbing a photon from incident light, then the excited electron is scattered by emitting (or absorbing) phonons and relaxes to the valence band by emitting photons. The

generally observed Raman spectra are from the scattered photons whose energy is smaller than that of the incident photons. Their energy difference is the energy of the scattered phonon. By measuring the intensity of the scattered light versus its frequency downshift (energy loss), the Raman spectra are obtained.

Raman spectra of SWNTs provide a lot of information about their phonon structure and electron structure. Because the mechanical properties, elastic properties, and thermal properties of SWNTs are strongly influenced by phonons, information about the structure and properties of SWNTs can be obtained from their Raman spectra. The SWNT has a unique one-dimensional (1D) structure with one atom in thickness, a few tens of atoms in circumference, and many microns in length. The 1D confinement of electronic and phonon states results in the so called van Hove singularities in the density of states (DOS). Whenever the energy of the incident photons matches the joint van Hove singularity in the DOS, resonant Raman enhancement happens. Due to the diverse characters of van Hove singularities in SWNT and the 1D confinement, strong Raman scattering intensity is observed. [103] It makes Raman microscopy an extremely powerful tool, even for an isolated individual SWNT, to observe the vibrational properties of SWNTs.

The number of emitted phonons before relaxation of the lattice can be one, two, or more, which are called one-phonon, two-phonon or multi-phonon Raman processes respectively. The Raman processes can also be classified as first-order and second-order process based on whether the photon direction is changed or not in scattering. Generally, the Raman spectra of SWNTs include (1) the first-order Raman process involving one-phonon emission; (2) second-order involving one-phonon emission and (3) second-order

involving two-phonon resonant Raman processes.[35]

There is only one first-order Raman feature in graphite, the so-called G band located around 1582 cm^{-1}, which is associated with the symmetric sp^2 hybridized carbon network vibration. With the rolled-up graphene sheets, the SWNTs have similar first-order Raman spectra, G band, but it is composed with several features, including the Raman active modes with frequencies of 1584cm^{-1}, 1585 cm^{-1} and 1590 cm^{-1} shown in figure **2.7**. These features arise from different tangential vibration modes of C atoms in perfect sp^2 network. [104] This sharp and strong mode can be found in the Raman spectrum of any SWNT and they are almost independent of the laser excitation wavelength. There are also other features in G band associate with the resonant Raman enhancement from the separation between the van Hove singularities in the valence and conduction bands of the DOS. These generally appear as a broad band from ~1500 to 1600 cm^{-1}. [105]

Besides the G band around 1590 cm^{-1}, the SWNTs have another first-order mode, the radial breathing mode (RBM). This is a bond-stretching out-of-plane phonon mode for which all the carbon atoms move coherently in the radial direction as the Raman active mode with frequency of 165 cm^{-1} shown in figure **2.7**. [104] The RBMs are usually present in the range of 100-500 cm^{-1}. Since they are uniquely observed in the Raman spectra of SWNT, their presence is considered as a signature of SWNT.

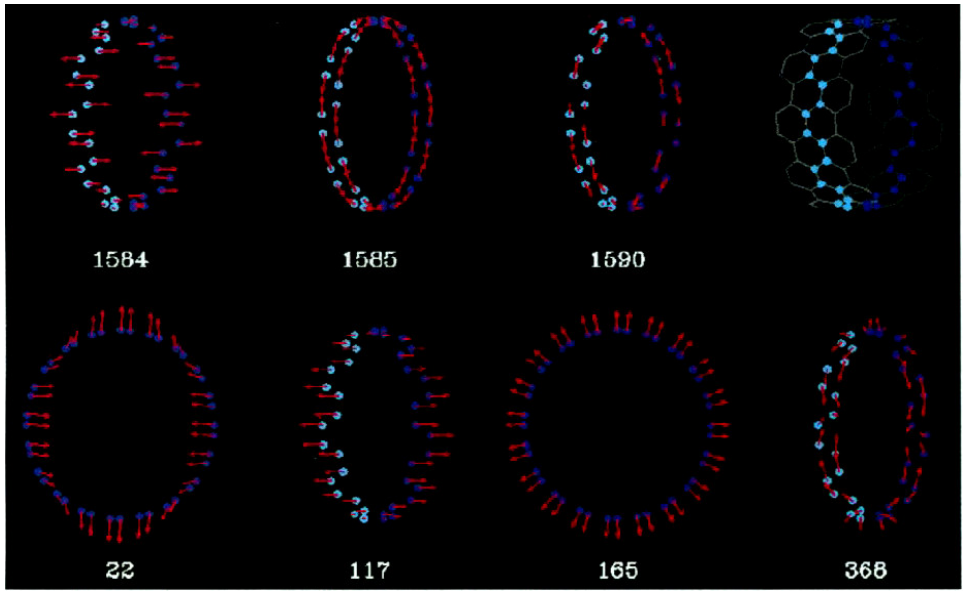

Figure **2.7** Theoretically calculated Raman active mode eigenvectors and frequencies for a (10, 10) nanotube. The red arrows indicate the magnitude and direction of the appropriate C atom vibrations, and eigenvectors shown correspond to the seven most intense modes in Raman spectra. The unit cell is shown schematically in the upper right corner. (Adapted from [104])

Theoretically, the RBM frequency is inversely proportional to the tube diameter and is expressed as

$$\omega_R(cm^{-1}) \approx C / d_t(nm) \qquad (\mathbf{2.25})$$

where C is a constant of value 224. [106] For a (10, 10) SWNT, the diameter is 1.36 nm, and the theoretical calculated ω_R is 165 cm^{-1} as shown in figure **2.7**. But in reality, the SWNTs are typically present as SWNT bundles, for which the tube-tube interaction needs to be accounted. The interaction within a bundle has been predicted to cause a ~6-20 cm^{-1} upshift in ω_R with respect to that of the isolated SWNT based on different theoretical calculations. [107-109] In this thesis, nanotube diameter d_t is calculated from the RBM frequency ω_R with [110]

$$\omega_R(cm^{-1}) \approx 224 / d_t(nm) + 14 \qquad (\mathbf{2.26})$$

The intensity of the RBM is dependent on the excitation wavelength because it is a resonant Raman scattering process, in which configurations whose band gaps match the excitation energy are preferentially excited. The Katauru plot relates the electronic transitions to the SWNT diameters and reveals that the incident light selectively interacts with different types of SWNTs. [111] By means of Katauru plot, Raman spectra from metallic SWNTs and semiconductive SWNTs can be distinguished as shown in figure **2.8**. [112]

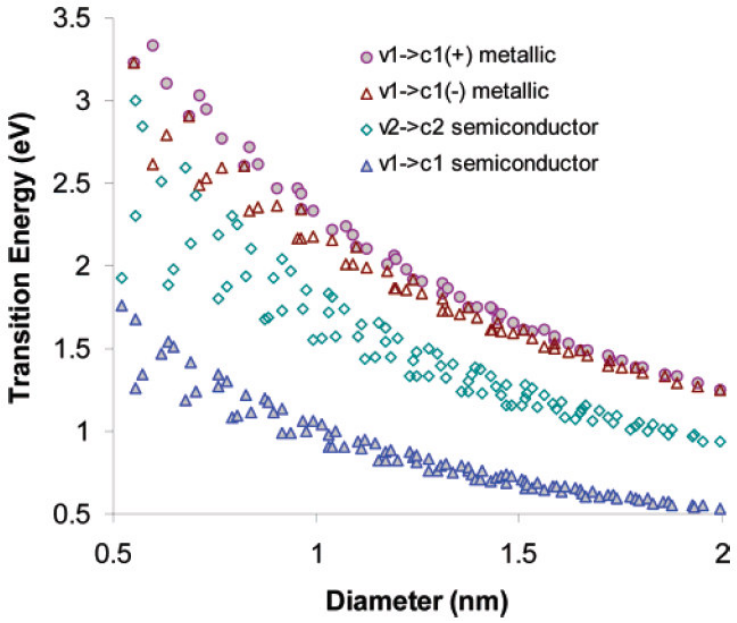

Figure **2.8** Revised Katauru plot based on experiment data of HiPco produced SWNT related the transition energy and the SWNT diameter. (+) and (-) refer to high and low energy transition respectively. *v* and *c* refer to valence and conduction band respectively. (Adapted from [112])

The RBM intensity is also sensitive to bonding, defects and charge transfer. It can be used as an indicator for the periodicity of sp^2 network in SWNTs.

The so called D band associated with the scattering of an electron via phonon

emission by the disordered sp^2 network is also important in studying the SWNT properties, especially functionalization of the sidewalls, because any change on the nanotube wall that affects its periodicity may strengthen the D band scattering. It is a weak band involving the one-phonon second-order Raman process. The D band frequency is in the range of 1250-1450 cm^{-1} and dependent on the laser excitation energy. This behavior is called "dispersive". [113-116] The D band frequency in graphite changes by 53 cm^{-1} with the laser energy changes by 1 eV. [35]

All forms of carbon show D band and G band in their Raman spectra with different intensities and frequencies. Graphite has very weak or even unrecognizable D band; [115] amorphous carbon has comparable weak D band and G band. [117] Usually the G band frequency is ~1582 cm^{-1} in graphite, and ~1591 cm^{-1} in SWNT. It is the case that while the Raman spectra of graphite and SWNT are frequently reported, those of NPC are not so common. The following is the Raman spectra of NPC by the pyrolysis of PFA at 600 °C taken with laser wavelength of 514.5 nm (energy of 2.41 eV). The PFA-NPC has G band around 1605 cm^{-1} and D band around 1350 cm^{-1} as shown in figure **2.9**.

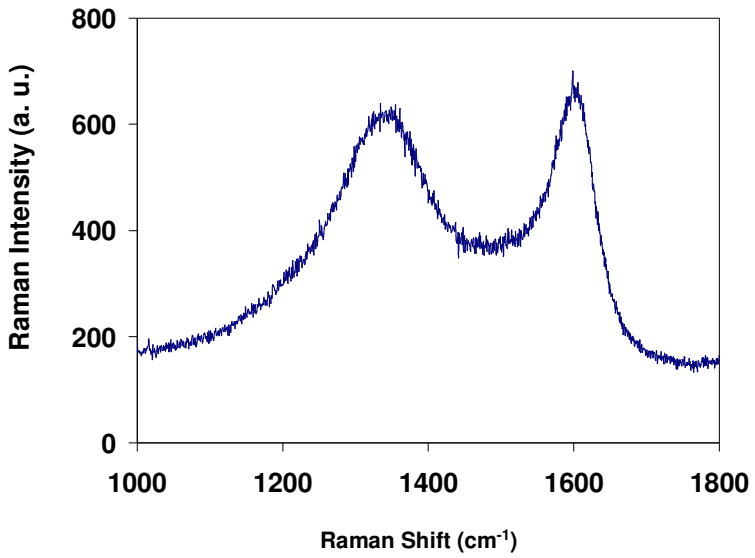

Figure **2.9** Raman spectra of NPC from pyrolysis of PFA at 600 °C. Excitation wavelength of 514.5 nm was used.

Chapter 3

Synthesis of SWNT/NPC Composites by Dispersing SWNT in PFA Solution

3.1 Introduction

In this Chapter, SWNT/NPC composites were made by a simple liquid phase blending process, in which the SWNTs were forced to disperse in a PFA/acetone solution by ultrasonication; the dispersion so made was then subjected to pyrolysis. The SWNT concentration in the composite was adjusted simply by changing the SWNT ratio to PFA. Scanning electron microscopy (SEM) and high resolution transmission electron microscopy (HRTEM) images and Raman spectra were used to characterize the composite carbons. Pore size distribution (PSD) of the composite carbons and mass transfer rate through them were measured by CH_3Cl adsorption. A structural picture of the SWNT/NPC composites was developed based on these characterization data and gas adsorption properties.

3.2 Experiments

3.2.1 Preparation

As prepared SWNT (AP-SWNT) (Carbolex Inc) was used to fabricate the SWNT/NPC composites. The AP-SWNT was produced by electric arc-discharge method with Ni-Y as the catalyst. PFA (Monomer-Polymer and Dajac Laboratory Inc) was dissolved in acetone to make a ~10 wt% solution, then the SWNT powder were added in with different weight ratios to PFA. The mixture was put into an ultrasonic bath for more than 10 h to obtain suspensions of SWNT. The mixture was then poured into a quartz boat and pyrolyzed in a tube furnace with a continuous flow of argon at 600 ºC for 8 h. The products were ground into powder and sieved for further analysis.

The SWNT concentration in the composite carbon was calculated from the SWNT/PFA ratio in precursor. The following assumptions were made for the calculations: the carbon yield of PFA is 33 % and it did not change with addition of SWNTs; and there was no weight loss for SWNT in blending and pyrolysis. Both assumptions were reasonable based on experiment data. The resulting composite carbons had SWNT concentration range from 14 - 80 wt%.

3.2.2 Characterization

The morphologies of the composite carbons, PFA-NPC and AP-SWNT samples were characterized with SEM and HRTEM. The samples for SEM were grounded into fine powder and affixed to a carbon tape. All of the carbon samples for imaging were coated with gold by sputtering for 45 sec prior to imaging. The SEM images were obtained with a Hitachi S3000-H SEM operated with 5 kV beam. Particles of the AP-SWNT and a ~39 wt% SWNT/NPC composite were suspended in acetone and ground in an agate mortar. The suspension was then dropped on the holey carbon-coated grid for the TEM study. HRTEM images were taken with JEOL 2010 LaB6 under 200 kV.

Samples for Raman spectroscopy consisted of thin films formed by dropping a suspension of the pulverized sample on glass slides. Raman spectra of the carbons were obtained with a BOMAN DA3+ Fourior transform (FT) spectrometer and an excitation wavelength of 1064 nm.

3.2.3 CH_3Cl adsorption

The pore size distribution (PSD) of the AP-SWNT, PFA-NPC and their composite carbons was obtained with CH_3Cl adsorption at -25 – 30 °C and 3.5 – 700 torr. The mass transfer rate of CH_3Cl through the composite carbon was studied with the microbalance. The system temperature was set at 30 °C and CH_3Cl was dosed into the sample in manual control mode until the pressure was 40 torr. The instantaneous CH_3Cl uptake values were recorded each minute and the adsorption rates were compared with model introduced in chapter 2.

3.3 Results and discussions

3.3.1 SEM images

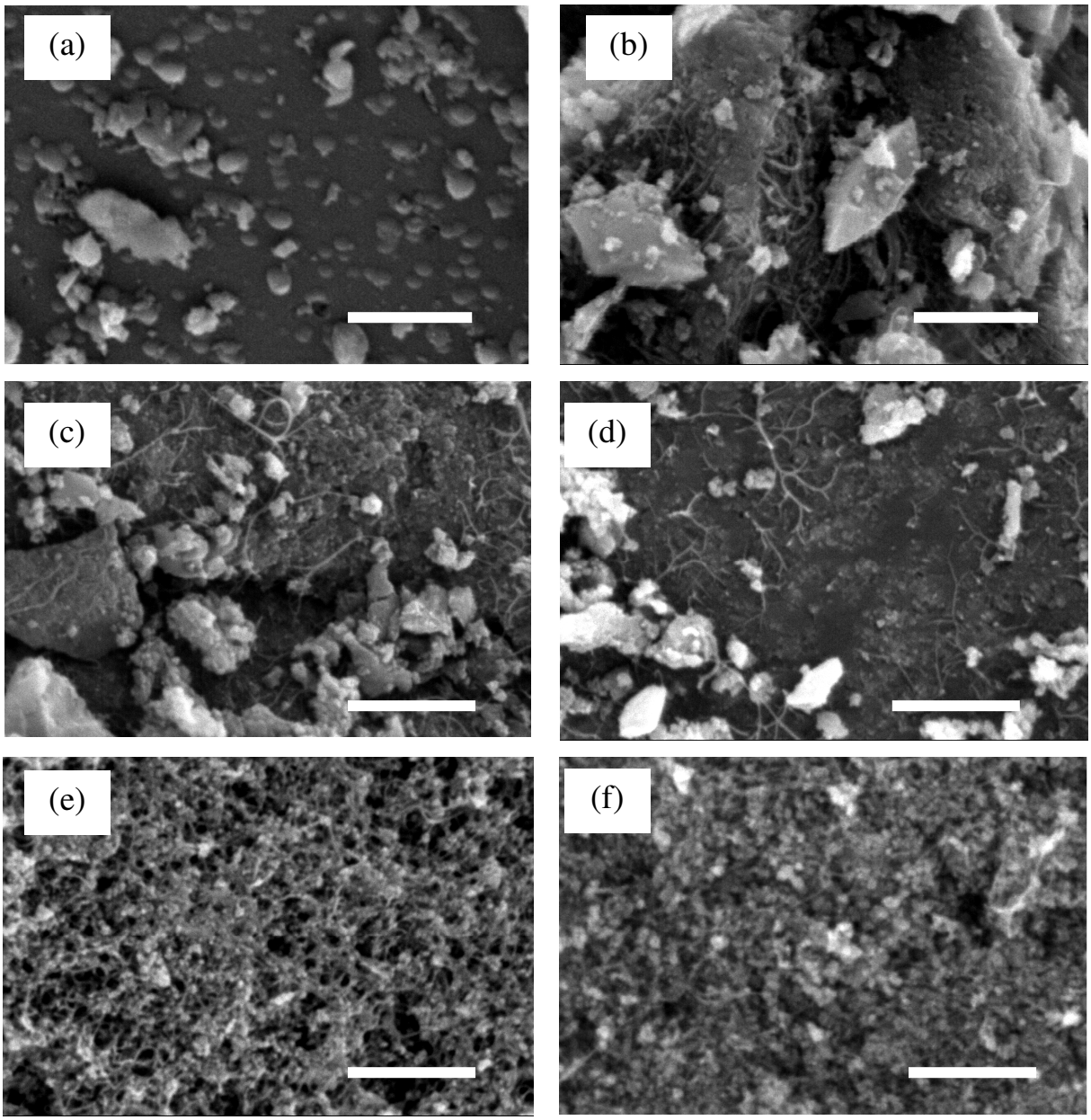

Figure **3.1** SEM images of carbon derived from (a) PFA, (b) 14 wt% SWNT/PFA, (c) 39 wt% SWNT/PFA, (d) 50 wt% SWNT/PFA, (e) 80 wt% SWNT/PFA and (f) AP-SWNT (Scale bars 1μm)

Figure **3.1** shows SEM images of the PFA-NPC, the composite carbons and AP-SWNT. In the image of PFA-NPC is a glassy carbon and looks smooth and featureless, while in the composite carbon and the AP-SWNT nanotube samples, bundles could be seen clearly. These images confirmed that the SWNT bundles survived after ultrasonication but most especially after pyrolysis of the polymer. In the composites made with SWNT concentrations of 14 wt%, 39 wt%, and 50 wt%, the SWNTs were embedded in NPC, with apparently similar structures despite the different SWNT concentrations. When the SWNT concentration became very high, (~80 wt %), the bundles formed a network to which the NPC particles clearly adhere. In the SEM images of the composite carbons, the SWNT bundles were more evident than in the images of the AP-SWNT sample. This was because the SWNT bundles were dispersed by the process of ultrasonication which was used to drive them into the PFA solution, thus they became easier to observe than they were even in the AP-SWNT starting material. Additionally, the impurities, especially the catalyst particles with higher conductivity than SWNTs, present in the AP-SWNT sample actually covered the SWNT bundles and made them harder to image and observe in the SEM.

Although SWNT bundles were embedded in the NPC, from multiple SEM observations they were not uniformly distributed, especially in the composites with low nanotube concentration, e.g. composites with 14 wt% SWNT. It was obvious that there were regions abundant in nanotubes but also many regions that were completely lacking in any nanotubes. This is clearly due to SWNT settling during pyrolysis, since this step lasted for more than 10 hours after ultrasonication stopped.

3.3.2 TEM images

TEM images of AP-SWNT and a 39 wt% SWNT/NPC composite are shown in figure **3.2**. In both samples, SWNT bundles of ~10 nm can be seen, showing the integrity of the SWNT bundle after ultrasonication and pyrolysis. In the composite carbon, it can be seen that the SWNT bundles were covered with some amorphous carbon, which had the same morphology as NPC. It showed that the SWNT bundles could be partially "wetted" by PFA. There were some impurities in AP-SWNT. The bright spots were the catalyst particles remaining from the preparation of SWNT. These impurities also existed in the composite carbon.

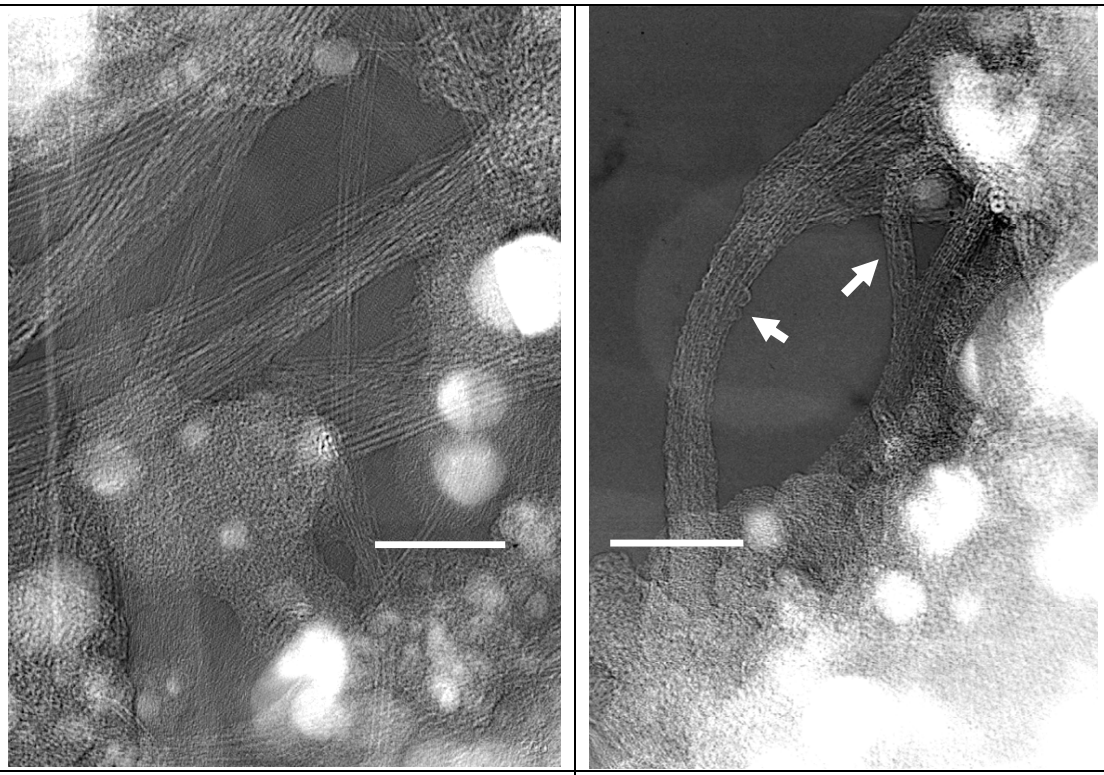

(a) (b)

Figure **3.2** HRTEM images of (a) AP-SWNT and (b) 39 wt% SWNT/NPC composite. The arrows were pointed to the SWNT bundles covered with NPC. (Scale bars 25 nm)

3.3.3 Raman spectra

Raman spectroscopy is a powerful tool to provide deep insight into the structural features of SWNTs because it is so sensitive to even minor changes, as introduced in Chapter 2. Raman spectra of the AP-SWNT and the 14 wt%, 50 wt% and 80 wt% SWNT/NPC composite carbons are shown in figure **3.3**.

There was a single peak at ~160 cm^{-1} in the RBM of AP-SWNT, showing that the SWNTs excited by wavelength of 1064 nm had an average diameter of 1.51 nm according to Eq **2.16**. [110] The intensity of the RBM is sensitive to bonding, defects and charge transfer. If there is any chemical bonding between SWNT and NPC, which would perturb the perfect periodicity of sp^2 network comprising the SWNT walls, then the RBM intensity would decrease dramatically. The RBM of the composite carbons was not as strong as in the AP-SWNT. To investigate the changes quantitatively, the RBM intensity with respect to the SWNT concentration was plotted in the inset. It can be seen that the intensity of RMB increased almost linearly with the SWNT concentration in the composites. Therefore, the lower intensity of the RBM in the composite carbon compared to AP-SWNT could be attributed simply to the lower concentrations than in the native sample, rather than to interactions between SWNT and NPC. Additionally, the frequencies of the RBM of the composite carbons were the same as those of AP-SWNT. The spectra gave no indication that the SWNT bundles were either segregated or chemically bonded with NPC.

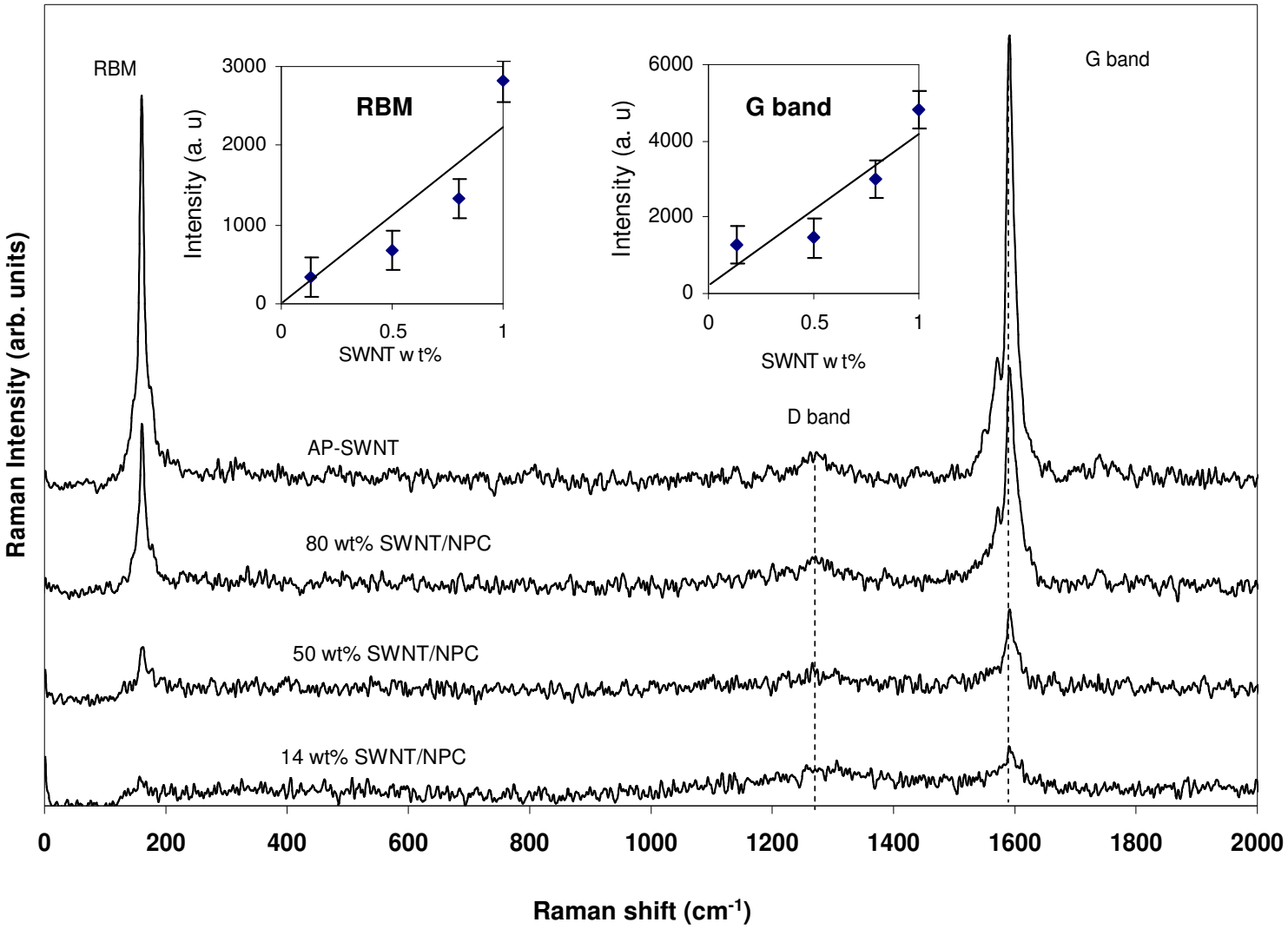

Figure **3.3** Raman spectra of AP-SWNT (Carbolex) and the SWNT/NPC composites. The excitation wavelength is 1064 nm. The RBM intensities and G band intensities with respect to SWNT concentration in composite carbon are shown in the inset.

In the tangential mode, there was a weak D band in spectrum of the native AP-SWNT sample, indicating a small amount of defects and impurities. For the composite samples, the intensity of the G band increased with SWNT concentration, as that occurred with the RBM. Actually, the NPC had a much weaker G band than that of SWNT, so it contributed little in the composite carbon thus SWNT concentration in the composite determined the intensity of the G band. The relative intensity of D band to G band, I_D/I_G, increased with decreasing SWNT concentration because the NPC has more disorder and a higher I_D/I_G ratio than SWNTs. Similar to the RBM, the frequencies and widths of both G band and D band did not change in the composite carbons compared with AP-SWNT.

In summary, the Raman spectra of the composite carbons confirmed that the SWNT bundles were intact after pyrolysis, which is consistent with the conclusions from the SEM and TEM studies.

3.3.4 Pore size distribution (PSD)

The PSD of PFA-NPC, AP-SWNT, and carbon composites derived from AP-SWNT/PFA solution blending are shown in figure **3.4**. For all of the composite carbons, regardless of the concentration of SWNTs in the precursor, a sharp peak around 5Å appeared, which was a feature due to NPC and indicated the normal formation of NPC micropores in all of these composites. When the SWNT concentration was less than 50 wt%, the composite carbons showed the properties of NPC only with very few mesopores (figure **3.4**a). None of the composites had the mesoporosity of the native SWNT sample (figure **3.4**b). Only when the concentration of SWNTs in NPC becomes very high (~80

wt%, Fig **3.4**b), does the composite carbon begin to show some of the mesoporosity of the SWNTs.

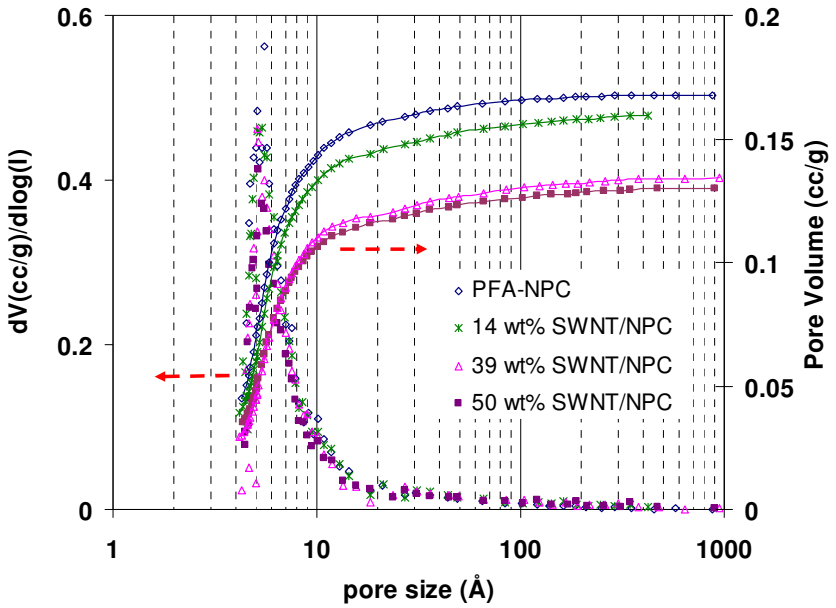

(a)

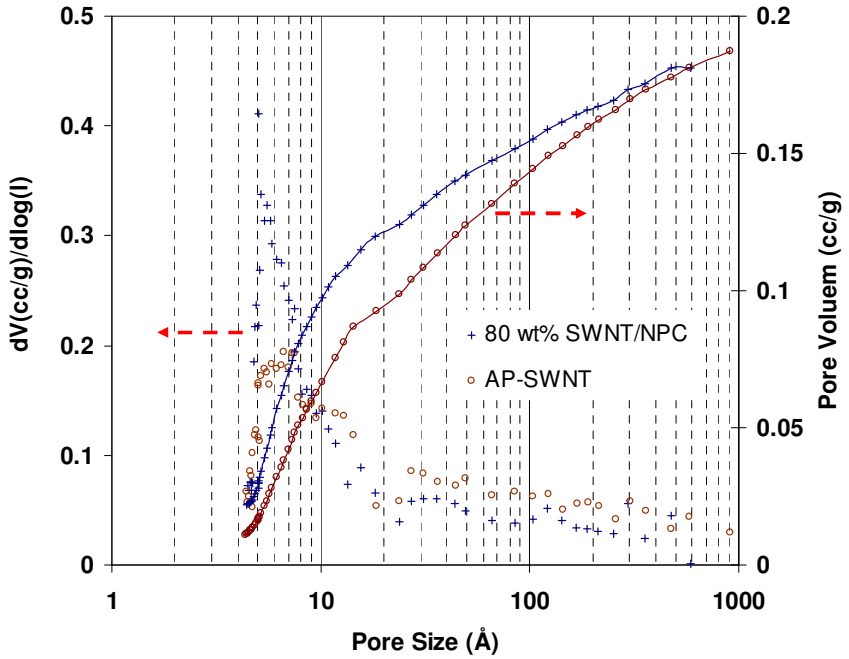

(b)

Figure **3.4** PSD of (a) NPC-PFA, 14 wt%, 39wt%, and 50 wt% SWNT/NPC composites; (b) 80 wt% SWNT/NPC composite and AP-SWNT.

The cumulative pore volumes of the composites decreased with the addition of SWNTs when their concentrations were less than 50 wt% in total. It can be seen that the lower pore volumes in the composite carbons when compared to that of the PFA-NPC was simply a result of a decrease in mass of the micropore rich phase. To study the pore volume evolution with respect to the SWNT concentration, the ultramicropore was defined here as the pores with size below 0.7 nm. The ultramicropore, micropore and mesopore volumes of the composites versus the SWNT concentration are plotted in figure **3.5**.

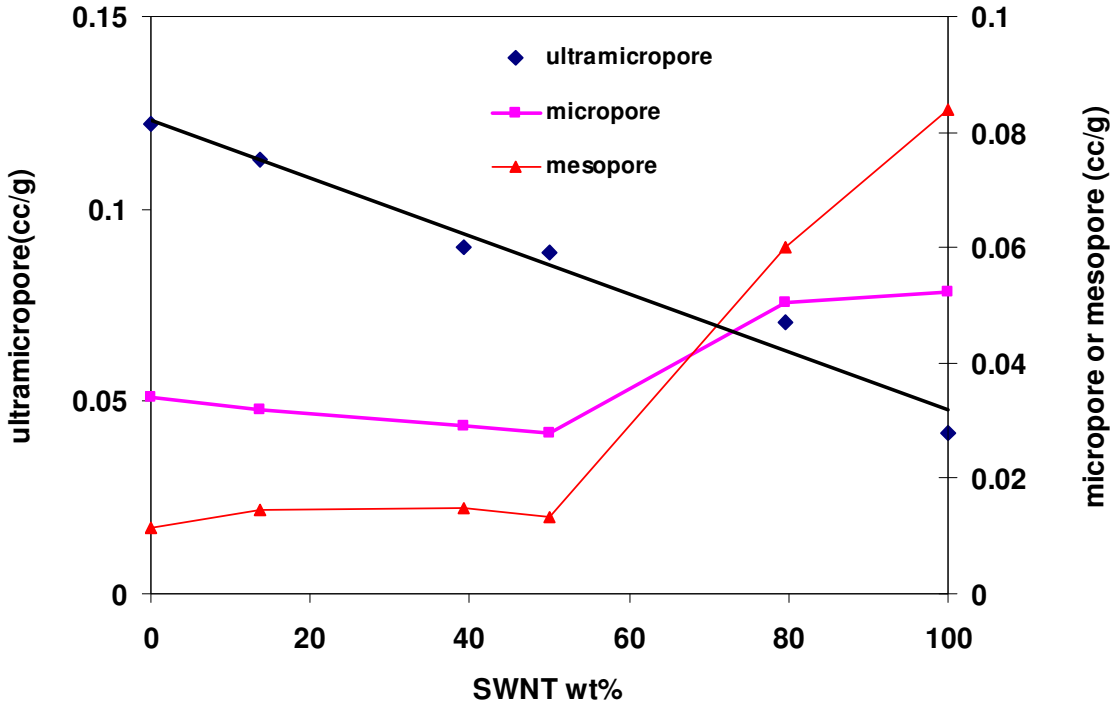

Figure **3.5** Ultramicropore ($l < 0.7$ nm), micropore (0.7 nm $< l <$ 2 nm) and mesopore (2 nm $< l <$ 50 nm)) volume evolution with SWNT concentration in composite carbons.

The ultramicropore volume decreased linearly with the SWNT concentration. In other words, it was the simple addition of the fractional contribution from the two components. This indicates that the structures of SWNT and NPC at the nanoscale are not changed by being in the composites. The micropore (0.7 nm < l < 2 nm) volume decreased slightly when SWNT concentration was lower than 50 wt%; but increased when SWNT concentration became higher. The mesopore volume showed a similar trend to that of the micropore volume; it remained nearly constant at low SWNT concentrations, then increased linearly in high concentration range.

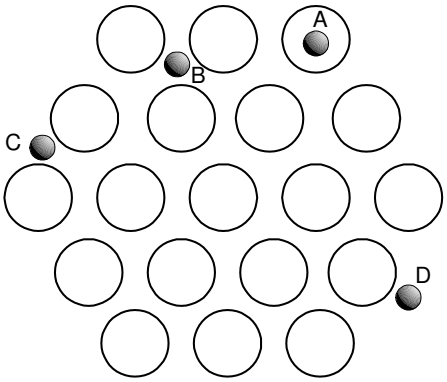

Figure **3.6** Scheme of different adsorption sites on SWNT bundles: inside tube (A); interstitial channel (B); groove (C); and surface (D). [118]

To analyze the structure of the composite carbons from the PSD data, the adsorption on SWNT bundles needs to be reviewed first. The adsorption sites of SWNT bundles can be inside the tubes (A), in the interstitial triangular channels (B), in the grooves (C) and at the surface (D) of the bundle (figure **3.6**). Because the length of a SWNT is in the range of μms, the adsorption sites of B, C and D can be considered as slit pores. Although the site A is cylindrical, the slit pore approximation only causes a pore

size error of less than 0.3 nm. [119] Therefore, the pore size calculation used above can provide meaningful information about these adsorption sites.

Type A sites are available only when the SWNT is open-ended. Usually, in the as prepared SWNT, more than 90% of the SWNTs are close ended and the "open" SWNTs have dangling bonds at the end, so the gas molecules are blocked from entry. Raman spectra showed the AP-SWNT had an average diameter of ~1.5nm, but there was no sharp peak around 1.5nm in its PSD (figure **3.4**b). This confirmed that the SWNT were close ended and that the CH_3Cl was not adsorbed inside the nanotubes.

The distance between the neighboring SWNTs in a bundle is only ~3.4 Å, so the pore size of type B sites is not always big enough for gas molecule to enter. Whether or not the gas can be adsorbed on sites B is dependent on the adsorbate molecule size and shape, adsorption conditions, and the SWNT bundle structures etc. Theoretical calculations and experiments showed that spherical molecules, such as Ne, Ar, Xe and CH_4, cannot be adsorbed on sites B. [120, 121]. A CH_3Cl molecule is nearly spherical with diameter of ~4.2 Å so CH_3Cl at room temperature would not enter sites B either. The PSD of SWNT lacked a sharp ultramicroporous peak corresponding to sites B so adsorption on site B could be neglected.

Sites C and D on the exterior surface of SWNT bundles are always available for adsorption, if they are exposed to gas. For the AP-SWNT sample, most of the CH_3Cl adsorption happened on these sites. The groove sites, C, could be considered as slit pores with continuous and gradually increasing pore size. The pores below 5 Å and the plateau between 5-7.5 Å in the PSD of AP-SWNT could be attributed to these sites. The exterior sites, D, near the grooves contributed to the micropore volume in AP-SWNT. The D sites

that are far from the grooves behave more like planar adsorption sites and contribute to the adsorption attributed to the mesopores. The AP-SWNT sample had an approximately constant *dV/dlog(l)* value for these pores, suggesting that a gas molecule were adsorbed on different position of SWNT bundles' exterior surface with equal probability.

According to the SEM images of the composite carbon, the SWNT bundles were embedded in NPC when SWNT concentration was relatively low; alternatively, when SWNT concentration is high, the SWNT bundles formed a network with nanosize NPC particles adhering to it. The two types of structure can be drawn as figure **3.7**.

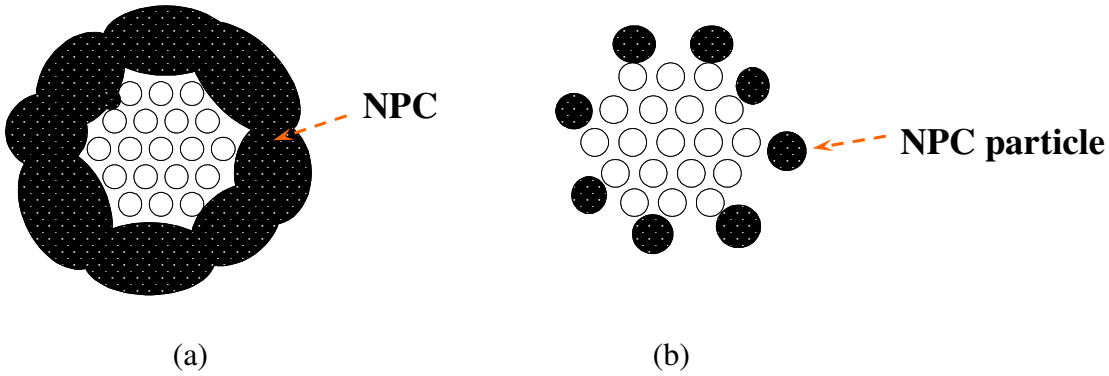

Figure **3.7** Scheme of structure of SWNT/NPC composite carbon with NPC (a) and SWNT (b) as the major component.

It is clear that most of the D sites are blocked in structure (a), when the volume fraction of NPC is sufficient to cover all of the SWNT bundles. The microporosity and mesoporosity of the composites with this structure (14 wt% and 50 wt% SWNT/NPC) were almost the same as those of NPC. The approximately constant mesoporosity also suggested that the size of the NPC microdomain remained the same when it contained SWNT bundles with structure (a) because the mesopores in NPC only emerge at the

edges of the microdomains. However, the linear change in ultramicroporosity with SWNT concentration revealed that the bundle grooves (sites C) were not filled by NPC in the composites. If PFA were tightly bonded with SWNT after blending, it could enter the bundle grooves; then the PFA-NPC occupied these sites after pyrolysis, making the ultramicropore volume lower than it would be for a simple linear addition of SWNT and NPC. Therefore, the linear change of ultramicropore volume provided proof that NPC was loosely attached to the SWNT bundles in these composites.

In the 80 wt% SWNT/NPC composite, SWNT bundles were the major component in the composite and NPC formed particles on it (figure **3.7**b). In this structure, only part of sites D was covered, so the mesopore volume started to increase with SWNT concentration. If the SWNT bundles were split in preparation of the composites, the exterior surface area would increase. For example, when one SWNT bundle splits into two bundles of the same size, the exterior surface theoretically increases by ~$\sqrt{2}$ times. Therefore, one may expect the mesopore volume to be significantly higher than the linear addition of those of NPC and SWNT in structure (b) if SWNT bundles were split. However, the linear volume increase conveyed that the SWNT bundles were intact in the composite. The ultrasonication was not vigorous enough to break up the bundles. The micropores, which were sites D near the grooves, had a little higher volume than that of AP-SWNT, showing these sites were also open without NPC covering as sites C. It also suggested that NPC particles were more loosely attached on the SWNT bundles exterior surface than in structure (a). A slightly higher volume of micropores in 80 wt% SWNT/NPC than in AP-SWNT might come from the removal of some impurity nanoparticles from these sites during ultrasonication.

3.3.5 Mass Transfer rate

The adsorption of CH_3Cl on the PFA-NPC, AP-SWNT and their composite carbons was done at the same temperature and pressure, so that the driving forces for mass transfer were the same for all experiments. According to H-K model, the adsorption at 30ºC and 40 torr was associated with slit pores having sizes below 5.85Å, so any change in the transient uptake data would suggest change in the ultramicropore structures.

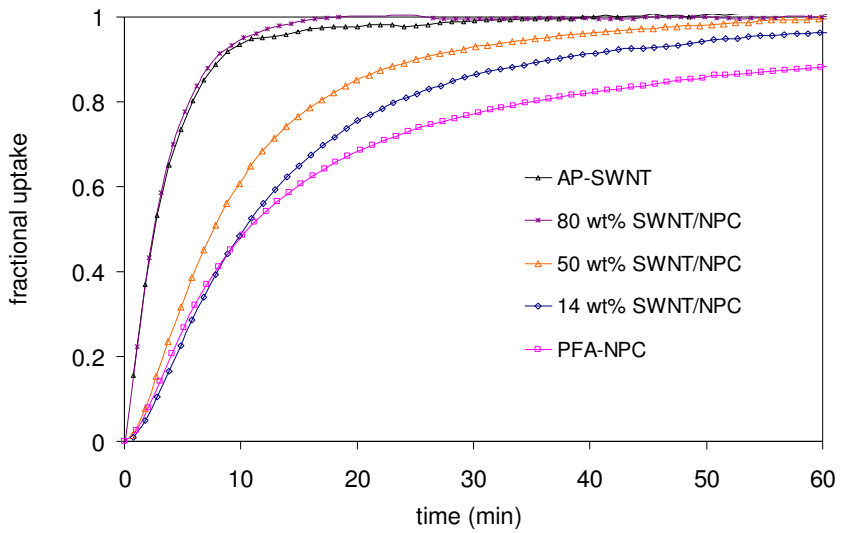

Figure **3.8** Normalized CH_3Cl fractional uptakes in PFA-NPC, SWNT/NPC composites and AP-SWNT at 30 ºC and 40 mmHg.

The fractional uptake $w(t)/w^*$ with respect to the adsorption time was plotted in figure **3.8**. It can be seen that the mass transfer rate changed significantly in the composite carbons compared with PFA-NPC, although some of them had less porosity than NPC (figure **3.4**). The uptake data in figure **3.8** were fitted to the barrier resistance

model and to the pore resistance model as introduced in chapter 2; the results are shown in figure **3.9**.

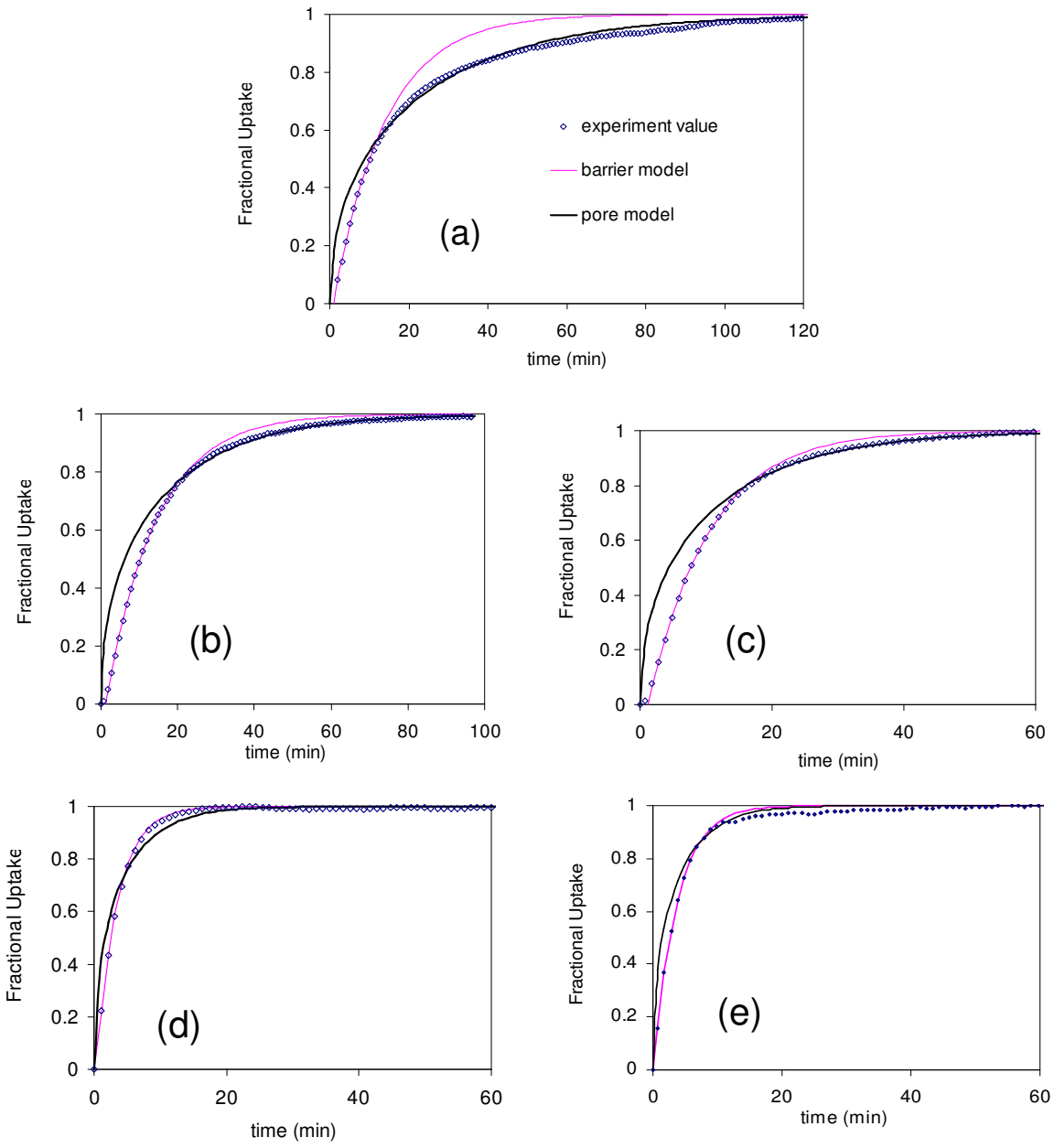

Figure **3.9** Fractional uptake of (a) PFA-NPC; (b) 14 wt% SWNT/NPC; (c) 50 wt% SWNT/NPC; (d) 80 wt% SWNT/NPC and (e) AP-SWNT fitted with barrier resistance model and to the pore resistance model respectively.

For AP-SWNT and the 80 wt% SWNT/NPC composite, the barrier model nearly perfectly fit the transient adsorption data. For the other samples, the barrier model fit the short time range better, while the pore model fit the long time range better. This makes sense intuitively since at short time the greatest resistance to transport of the gas molecules is met overcoming the pore mouth resistance, while at longer times the adsorbate concentration at the pore mouth, q_c, becomes higher, approaches the equilibrium adsorbate concentration q^*, and the mass transfer becomes limited by the resistance to transport due to internal pore diffusion experienced by the majority adsorbed species. Therefore, we may obtain k_b and $\frac{D}{r_c^2}$ from short time range and long time range, respectively. The results are listed in table **3.1**.

Table **3.1** Mass transfer constant in SWNT/NPC nanocomposites

	PFA-NPC	14wt% SWNT/NPC	50 wt% SWNT/NPC	80 wt% SWNT/PFA	SWNT
k_b(min^{-1}) (<15 min)	**0.0757**	**0.0766**	**0.1076**	**0.3161**	**0.2742**
$\frac{D}{r_c^2}$ (min^{-1}) (> 15 min)	**0.00346**	**0.00490**	**0.00703**	**0.01894**	**0.02061**

It was also found that pore model fit NPC-PFA data well from 10 min to 120 min, but for SWNT/NPC composites, the barrier model was always a better fit than pore model even with a low concentration of SWNT (5 wt%). This result suggests that for the SWNT/NPC composites barrier resistance dominates and tends to control the rate until very long time closer to saturation adsorption levels. The best explanation for this is a decrease resistance arising from internal pore diffusion (an increase of diffusivity) within

the microdomains and brought on by the presence of the SWNTs. From Eq **2.18**, it can be seen that the pore diffusion rate increases with $\frac{D}{r_c^2}$. As discussed above, although the size of NPC microdomains might be the same in the composites with SWNT concentration less than 50 wt% as in the AP-SWNT form, the structures were changed by having SWNT bundles inside. The ultramicropores in NPC are slit pores with high tortuosity, while those along the walls and grooves of SWNT bundles are straight channels. The presence of the SWNT bundles leads to much higher average diffusivity in these microdomains when compared to those for microdomains in the NPC alone. Not surprisingly then, with increasing SWNT concentration, there were more ultramicropores arising from nanotubes in the composites, thus resulting in the average diffusivity increasing and the resistance from pore diffusion becoming less and less significant.

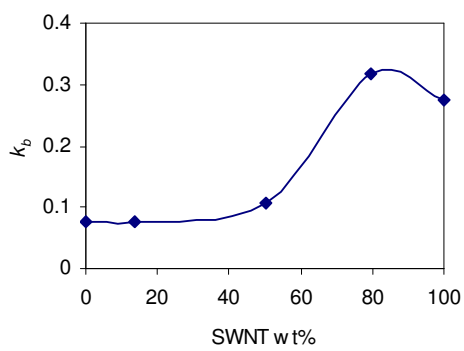

Figure **3.10** Evolution of pore mouth resistance k_b versus the SWNT concentration in composite carbon.

The increase of k_b with SWNT concentration also confirmed there are structural changes in NPC microdomains due to their presence. Unlike the ink bottle structure of the ultramicropores in the microdomains within the NPC, the addition of SWNTs

diminishes resistance at edges and through the microdomain by providing straight channel with low resistance into its interior. However, k_b did not increase sharply when the SWNT concentration was less than 50 wt% in the composite because at such levels of SWNT concentrations, the bundles were embedded in the NPC phase and most of the sites C were covered and thus they did not provide "super highways" to the interior of the microdomains. The k_b in these composites reflects the resistance from the NPC. With increasing SWNT concentration, on average the diffusion lengths within the NPC became shorter and as they did k_b slowly increased. The percolation threshold was between 50 and 80 wt%. The SWNT bundles started to have an open exterior surface in this concentration range and their ultramicropores were easy to access. The higher k_b of the 80 wt% SWNT/NPC composite than the SWNT, corresponds to its higher microporosity than that of SWNT (figure **3.5**), and may also be attributed to the removal of impurities on the bundle surface.

3.4 Summary and conclusions

In summary, the SWNT/NPC composites with various nanotube concentrations were prepared with solution blending of SWNT and PFA in acetone followed by pyrolysis. The SWNT bundles were intact after ultrasonication and pyrolysis. There was no significant exfoliation or splitting of the bundles in the process of preparation. However, the local structure of PFA-NPC was modified by adding SWNT bundles, even though the constituent microdomains remained the same size as those in the pure form when SWNT concentration was less than 50 wt% in the composites. In these composites, the SWNT bundles were embedded in NPC and rendered mostly "in communicado". When SWNT concentration became high, the NPC formed particles that were attached on their exterior surface. The NPC and SWNT were only loosely attached and no chemical bonding between SWNT and NPC was found.

Since the SWNT bundle grooves were straight pores, they had much less diffusion resistance and pore mouth resistance than the ultramicropores of NPC. By modifying NPC structure with SWNT bundles, the pore diffusion resistance became less significant and the mass transfer through composite carbons was controlled by a barrier at the pore mouth. However, the enhancement of pore mouth mass transfer constant k_b was not significant when the SWNT concentration was lower than 50 wt% because most of the bundle grooves were covered with NPC. However, k_b started to increase sharply when SWNT concentration was high enough to have free exterior surface.

Chapter 4

Functionalization of SWNTs and preparation of NPC/SWNT nanocomposite

4.1 Introduction

The as-produced SWNTs are self-assembled in bundles with relatively strong interaction energies between neighboring tubes (~950 eV/μm along the tube-tube contact length). [43] This, plus their inherent non-polarity, makes it difficult to dissolve SWNTs in water, organic solvents or in most polymeric hosts. Therefore, the inability to manipulate and process SWNTs by methods used to make other composites has slowed progress in preparing new nanocomposites.

Some work has been done within the constraints of solubility and dispersion imposed by the properties of the native SWNTs. The most common method used to disperse SWNTs in a polymer is to suspend the nanotubes in a solvent containing the

polymer and then to ultrasonicate the mixture to drive them into a dispersion. [47, 52, 53, 59, 122] Although this is easy and readily done, it is of limited value as a general method of nanocomposite preparation since precipitation and settling of the SWNTs begins to occur almost immediately after sonication is discontinued. Nonetheless, by dispersing the SWNTs in monomer followed by rapid in situ polymerization, polymer-SWNT nanocomposites have been made. [63, 64, 123, 124] However, a homogeneous dispersion within the polymer of the SWNTs is far from guaranteed due to their inherent insolubility.

To approach a more uniform dispersion, the SWNTs should be modified to make their surfaces more compatible with the polymer matrix. It is commonly agreed that nanotubes decorated with polymers that are structurally similar to the polymer matrix should have good compatibility and should lead to much better nanocomposites. [125, 126] Therefore to prepare a well-developed SWNT/NPC composite, the SWNTs will first be dispersed in FA, followed by polymerization of FA to form a polymer around the tubes. The PFA wrapped SWNTs will be pyrolyzed to create a strong carbon-carbon interface between the SWNTs and the NPC. Thus, the dispersion of SWNTs in PFA is achieved by actually decorating the SWNTs with PFA.

Modification of SWNTs with polymers has been widely studied with the ultimate purpose of controlling their solubility and processibility, either through covalent bonding or non-covalent bonding. It has been reported some linear polymers can reversibly wrap SWNTs and make them soluble in water with concentration in the range of grams per liter. [44] The structure of the SWNTs is not altered by such noncovalent attachment.

However, since the interactions between the wrapping molecule and the nanotube are weak, the load transfer between SWNT and polymer matrix would be poor if a nano-composite was prepared with such noncovalent functionalization. Additionally, only specific classes of polymers can be attached on SWNT with these strategies.

On the other hand, a much stronger interaction between SWNTs and a polymer might be achieved by covalent functionalization. Several covalent functionalization strategies were studied recently, including fluorination with elemental fluorine, [78] ozonation, [79] cycloaddition with nitrene, carbene, or radicals, [80-82] by the Bingel reaction, [83] and via electrochemical reduction of diazonium salts [84-88]. After being functionalized using one of these strategies, the SWNTs can then be grafted to some polymers, with their tailored chemical and surface properties, in order to prepare polymer-SWNT nanocomposites. [127-129]

Since PFA is a crosslinking polymer, [130] it would be difficult to wrap it around a SWNT simply through noncovalent interactions. However, through covalent interactions it would be possible for PFA to bond with the SWNTs and to enwrap them. To obtain such a PFA-wrapped SWNT, a functionalized SWNT which is compatible with both of FA and PFA must be utilized. Sulfonic acids, such as para-toluene sulfonic acid (p-TSA), are commonly used as catalyst for FA polymerization, and they have good solubility in both FA and PFA. [131] So it can be expected that a SWNT with pendant sulfonic acid groups should be dispersible in FA and should catalyze FA polymerization. Now quite conveniently, for testing this line of reasoning, SWNTs with arylsulfonic acid groups may be prepared through a diazonium salt functionalization methodology

developed by Tour et al. [84-88] Based on these ideas, a methodology is presented to prepare a SWNT and NPC nanocomposite. In this process, SWNTs made from high pressure CO disproportionation (HiPco) are functionalized with arylsulfonic acid (SA-SWNT, Figure **4.1**), which is similar to p-TSA with a methyl group substituted by a SWNT. The "grafting-to" process begins when the monomer, FA is polymerized by the SA-SWNTs dispersed within it and the produced PFA then graft to these tubes to obtain PFA grafted SWNTs (PFA-SWNTs, Figure **4.2**). A carbon-carbon nanocomposite was then obtained by simple pyrolysis of the PFA-SWNT. Characterization of the PFA-SWNTs and the nanocomposite carbon is presented and discussed.

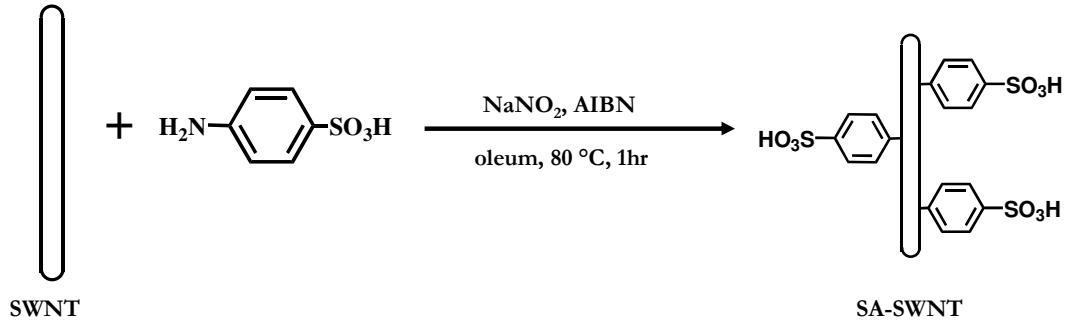

Figure **4.1** Scheme of functionalization of SWNT with sulfonic acid groups.

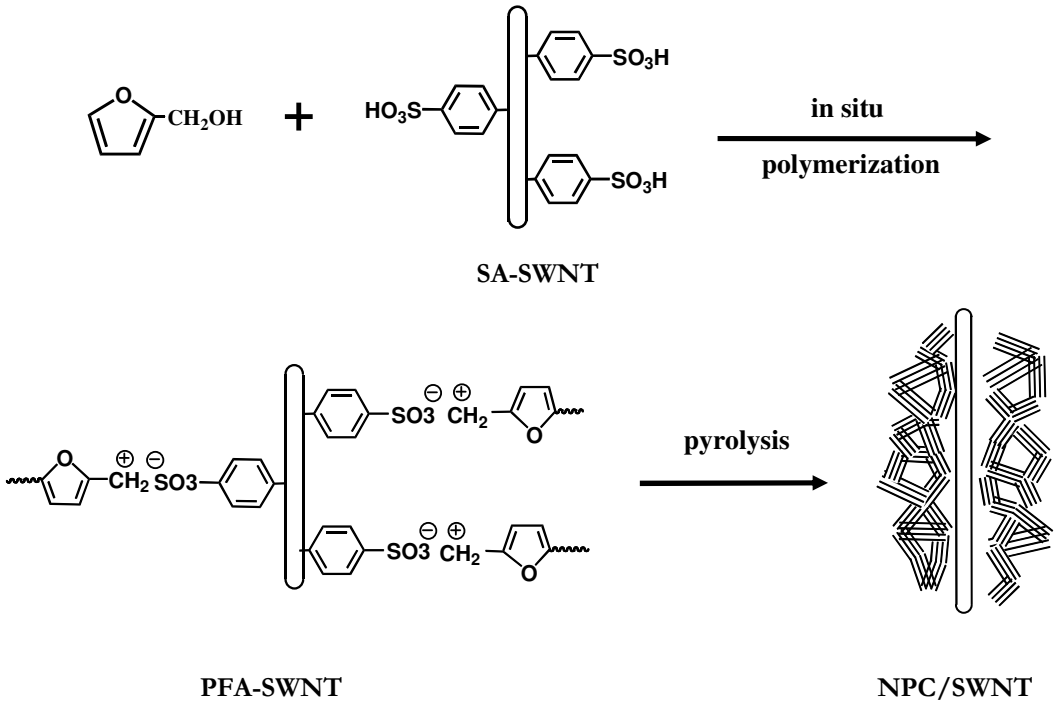

Figure **4.2** Scheme of preparation of PFA wrapped SWNT (PFA-SWNT) and NPC/SWNT.

4.2 Experiments

4.2.1 Materials

HiPco produced Single wall carbon nanotubes (SWNTs) were purchased from Carbon Nanotechnologies, Inc. (Houston, TX). HCl (36.5wt%), Oleum (20% free SO_3, A.C.S regent), sodium nitrite (99.99+%, RegentPlus^{TM}) sulfanilic acid (99% A.C.S regent), 2,2'-azobisisobutyronitrile (98% A.C.S regent), furfuryl alcohol (99%) were purchased from Sigma-Aldrich (Allentown, PA). Polycarbonate track-etch membranes

(0.2μ, Whatman Nuclepore®) and Anodisc filter membranes (0.2μ, Whatman Anodisc®) were obtained from Fisher Scientific (Pittsburgh, PA).

4.2.2 Purification of SWNT

The as-prepared SWNTs usually contain the metallic catalyst particles covered with graphitic carbon shells and other forms of carbon impurities. The oxidative stability of carbon is

Graphitic carbon > SWNT > amorphous carbon

So the amorphous carbon can be selectively removed by controlled oxidation. The graphitic carbon shells may also be partially removed without consuming the SWNTs by the catalytic oxidation resulting from the metal inside them. In the process of purification, the first step is to use wet air oxidation to remove amorphous carbon. This step is also helpful for the next step to remove metal impurities because the graphitic carbon shells surrounding them are catalytically oxidized. The second step is prolonged acid treatment. As a result of acid treatment, the metal particles are removed. There are also some SWNTs "opened" and some dangling bonds formed due to their reactions with oxidative acid. An annealing step is necessary to remove these dangling bonds.

In a typical process of purification, 100mg of AP-SWNT was put in a tube furnace for wet air oxidation. Air passing through a water bubbler at room temperature flowed into the furnace tube at a rate of 200sccm. The SWNTs were heated to 225˚C and kept at this temperature for 18h. The wet air oxidized SWNTs were then driven to disperse in 50ml of concentrated HCl in a 100ml flask by ultrasonication for 1h. This step

was followed by stirring and refluxing at 60˚C for 18h. The SWNT material was recovered after these treatment steps by filtration, washing and drying; the dried solid was labeled as pre-SWNT and characterized with TGA. Finally, the pre-SWNT was heated in Ar at 800˚C for 1h to obtain purified SWNT (p-SWNT).

4.2.3 Functionalization of SWNT with sulfonic acid group

Oleum is used as the solvent in functionalization because the SWNTs disperse as single tubes in it with concentrations up to 10 wt%. [132] In a process of functionalization of SWNTs (figure **4.1**), 50mg of p-SWNTs were stirred in 50ml oleum in a 100ml flask for 3h. Then it was heated to 80˚C and 1.15g sodium nitrite (4 equiv/mol C), 2.886g sulfanilic acid (4 equiv/mol C) and 0.137g AIBN, (0.2 equiv/mol C) were added, kept at 80˚C under stirring for 1 h. The mixture was poured slowly and carefully into more than 500ml water and filtered through a 0.2μ track-etch membrane. The filter cake was washed with acetone and water, repeatedly. After vacuum drying the filter cake at 100˚C overnight, SA-SWNT was collected by peeling off from the membrane.

4.2.4 Synthesis of PFA-SWNT

In 10ml FA 5 mg SA-SWNT were dispersed in a 20 ml vial using a 6mm ultrasonic probe of an ultrasonic processor (PGC Scientifics, 130 W). To reduce spontaneous thermal polymerization, which might cause too fast reaction rate and SWNTs agglomeration, 50% of the maximum amplitude (power) was applied and the vial was kept in an ice bath. A cycle of 5 sec of ultrasonication followed with 5 sec of

pause for heat transfer and re-equilibration of the sample was used. After 5h of ultra-sonication, the suspension was poured in 100ml water and filtered through a 0.2μ Anodic membrane. The filter cake was washed with a large volume of acetone and water repeatedly and then vacuum dried at room temperature. Isolated PFA-SWNT can be obtained by peeling the filter cake from Anodic membrane.

4.2.5 Synthesis of NPC/SWNT

Samples of PFA-SWNT were pyrolyzed in Ar to convert into NPC/SWNT. In this process, 5mg PFA-SWNT was heated to 600˚C with heating rate of 10 ˚C/min and soaked for another 1h in flowing Ar. For comparison, 5mg SA-SWNT was also treated under the same conditions.

4.2.6 Characterization

HiPco SWNT (CNI Inc.), pre-SWNT and p-SWNT were analyzed by temperature programmed oxidation (TPO) using a TA instruments SDT 2960. In this process, each sample was heated in flowing air with a constant heating rate of 5 ºC/min from room temperature to 800 ºC. The instantaneous weight changes with respect to temperature were recorded.

To prepare specimens for HRTEM and Raman spectroscopy, p-SWNT, SA-SWNT, oleum-treated p-SWNT, PFA-SWNT, and annealed SA-SWNT were dispersed in ethyl alcohol with ultrasonic processor for 30 min to create suspension. NPC/SWNT was ground in ethyl alcohol in an agate mortar followed by ultrasonication. HRTEM samples

were made by dropping the suspensions on the holey carbon-coated grids. Samples for Raman spectroscopy were thin films formed by their dispersion on glass slides. HRTEM images were taken with a JEOL 2010F operating at 200 kV. The point to point resolution was ~2Å. Raman spectra were collected under ambient conditions with a Jabin-Yvon Horiba T64000 micro Raman spectrometer. Excitation was provided by an Ar-Kr laser at 1-3 mW incident power. An excitation wavelength of 514.5nm was used.

Thin films of SA-SWNT and PFA-SWNT were prepared by filtering their water suspension through the track-etch membranes or Anodisc membranes. SEM images of the thin films on the track-etch membranes were taken with Hitachi S-3000H operating at 5kV. Both samples were sputtered with gold for 1 min before imaging. Contact angles of water on these materials were measured with a goniometer equipped with CCD camera on the Anodisc membranes.

Infrared spectra of p-SWNT, SA-SWNT and PFA-SWNT were taken using Nexus 670 FT-IR spectrometer. The samples were mixed with KBr and pelletized. The measurements were done in transmission mode.

4.3 Results and Discussions

4.3.1 Purification of HiPco SWNT

The TPO data of SWNTs revealed their oxidative stability at high temperature and the residue after oxidation indicated the ratio of metal impurities in them. The TPO data for AP-SWNT, pre-SWNT and p-SWNT are shown in figure **4.3**. The residue was assumed to be Fe_2O_3 since the metal impurities in HiPco SWNT, namely iron, was oxidized under the heating conditions. The residue was ~8.5 wt% for the AP-SWNT, so it could be calculated that the AP-SWNT contained ~6 wt% Fe. After purification, the residue decreased to ~5 wt% for both pre-SWNT and p-SWNT, indicating that the metal impurities decreased to ~ 3.6 wt%.

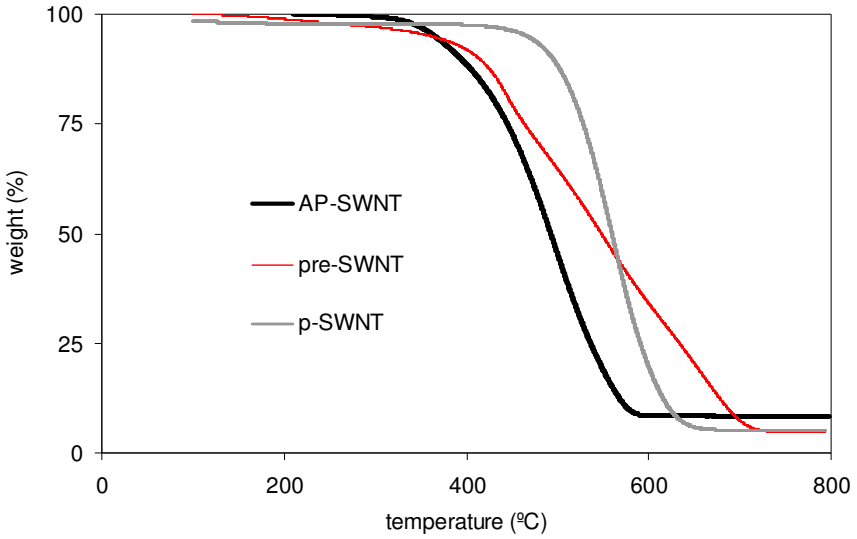

Figure **4.3** TPO of AP-SWNT, pre-SWNT and p-SWNT in flowing air.

The first derivative of TPO with respect to temperature (DTPO) shows the difference in oxidation temperature for various forms of carbon. Usually the amorphous carbon is oxidized at lower temperature than SWNTs and the oxidation temperature for graphitic carbon is the highest. By decomposing the DTPO curve into Gaussians, the ratio of the amounts of different carbons can be roughly calculated from the area under the corresponding Gaussian curves (figure **4.4**). The results showed that there were ~33 wt% amorphous carbon with oxidation peak temperature at 422ºC, ~54 wt% SWNT with oxidation peak temperature at 503ºC, and 7 wt% graphitic carbon with an oxidation peak at 600ºC in AP-SWNT. After wet air oxidation and acid treatment, the amorphous carbon ratio decreased to ~7 wt% and the SWNT ratio increased to ~78 wt%. Due to the removal of metal particles, the oxidation temperature of amorphous carbon, SWNTs and graphitic carbon increased to 441, 538 and 667 ºC, respectively. The biggest peak shift happened in the graphitic carbon because it was the carbon in close contact with the metal particles and its oxidation temperature was most significantly influenced by the metal catalysis in the oxidation. The smallest peak shift was for the amorphous carbon because it generally had no contact with metal particles.

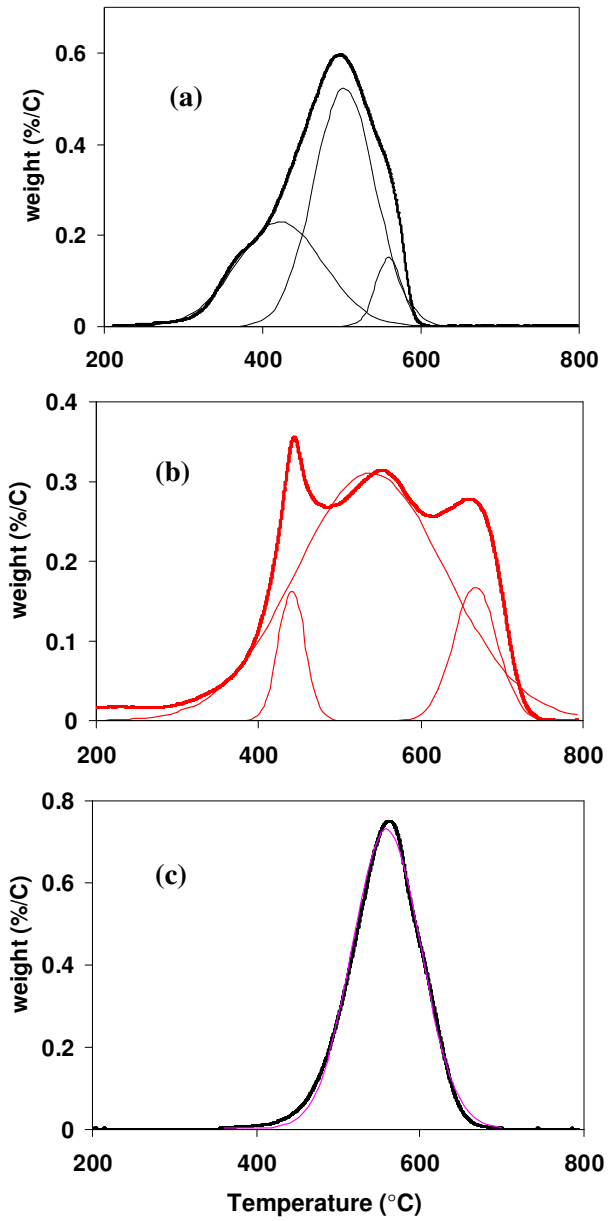

Figure **4.4** DTPO of (a) AP-SWNT, (b) pre-SWNT, and (c) p-SWNT.

An annealing step is necessary to remove the dangling bonds on SWNT formed from the acid treatment. Following annealing, the DTPO of p-SWNT became an almost perfect Gaussian curve centered at 559 °C, showing the removal of amorphous carbon

and graphitic carbon. The increase of oxidation temperature seen in figure **4.3**c could be contributed to the removal of dangling bonds since the SWNTs became more difficult to oxidize when the defects are decreased.

An HRTEM image of p-SWNT is shown in figure **4.5**. Large SWNT bundles with diameters bigger than 10 nm can be seen. Generally, each bundle contained tens to hundreds of nanotubes. Also it is evident that some fullerene-like carbon shells remained, which contributed to the weight loss of p-SWNT under 400 °C (figure **4.3**).

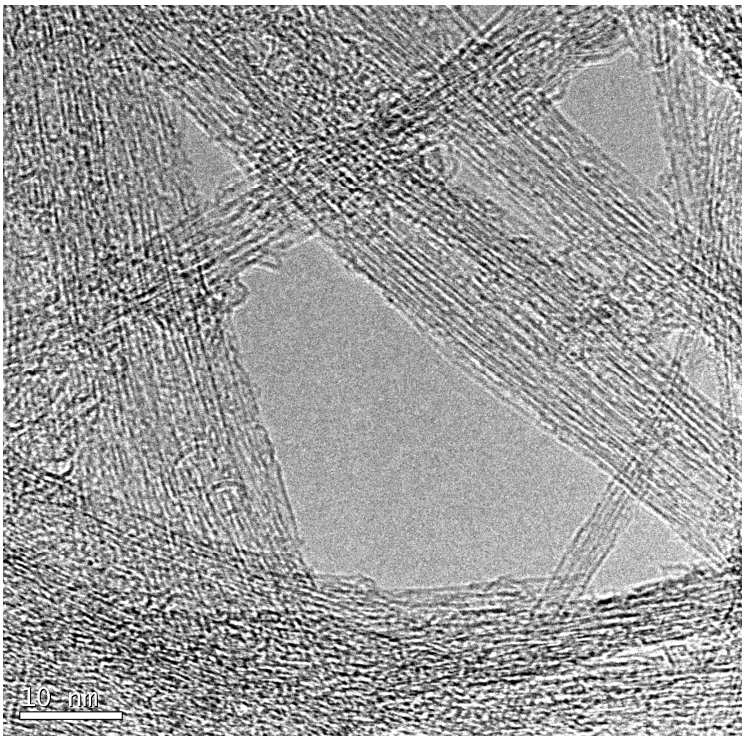

Figure **4.5** HRTEM image of p-SWNT.

4.3.2 Functionalization of SWNTs with sulfonic acid groups on the sidewall

Raman spectroscopy is an important tool in characterization of SWNTs because the Raman resonant scattering in SWNTs is sensitive to their structural changes. The Raman spectra of p-SWNT (a), p-SWNT treated with oleum only (b), SA-SWNT (c), and SA-SWNT annealed in Ar at 600°C for 1h (d) are shown in figure **4.6**. The spectra appear in two panels: 100–400 cm^{-1} associated with the radial breathing mode (RBM) of SWNT and 1250 – 1850 cm^{-1} associated with the tangential mode of SWNT, including the G band and D band. For comparison, all of the spectra are normalized with strongest G band intensity near 1590 cm^{-1}.

By decomposing the RBM of p-SWNTs (figure **4.6**a) with Lorentzians, 4 main bands at 247, 262, 268 and 271 cm^{-1} were obtained. According to Eq **2.26**, they were associated with the radial breathing vibrations of SWNTs with diameters of ~0.96, ~0.90, 0.88 and ~0.87 nm, respectively. On the basis of the accepted Kataura plot, [111, 112] all of these bands are associated with metallic tubes. A relatively weak peak at 186 cm^{-1} is also observed, which was associated with the semi-conducting nanotubes with diameters of ~1.30 nm.

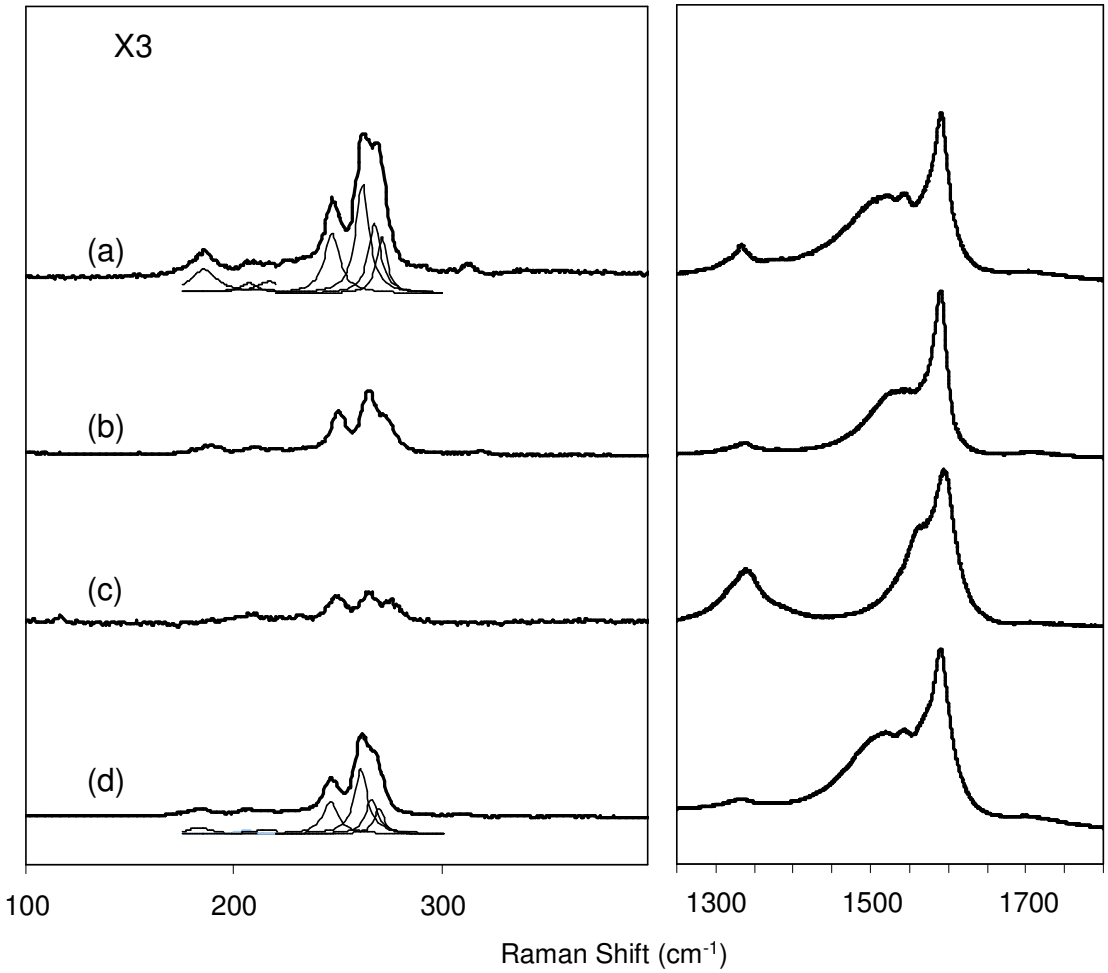

Figure **4.6** Raman spectra of p-SWNT (a); p-SWNT treated with oleum only (b); SA-SWNT (c); SA-SWNT after annealing in Ar at 600°C for 1h (d). For comparison, all the spectra were normalized with their strongest G band and RBM were strengthened by 3 times.

There is a weak D band in p-SWNT, suggesting a small amount of defects and impurities in it, which are also observed from HRTEM. In the G band, p-SWNT has a sharp and strong mode around 1590cm^{-1}. This feature can be found in the Raman spectra of any SWNTs and its frequency is almost independent of the laser excitation

wavelength. However, the broad shoulder with a maximum at ~1520cm^{-1} is not so common and only appears when a specific excitation wavelength is used. Pimenta et al. found this resonance enhancement over the tangential mode, including G and D bands, was related to a broad diameter distribution of *metallic* nanotubes. [105] For a metallic SWNT with diameter *d*, the Raman enhancement will occur whenever the incident or scattered photon is in resonance with $E_{11}(d) = E_{c1}(d) - E_{v1}(d)$, the energy separation between the first pair of electronic density of states (DOS) singularities in the valence (*v*) and conduction (*c*) bands. [133] The overall enhancement is the sum of the contribution from each metallic SWNT with different diameters. In p-SWNT, there are significant amount of metallic nanotubes excited by the wavelength of 514.5nm and their diameters are broadly distributed, resulting in a strong Raman enhancement in the tangential mode.

When the p-SWNT was treated with oleum, it showed G band narrowing (figure **4.6**b). This was because the SWNTs were protonated with oleum and the Raman resonant enhancement was weakened. Although there were RBM decreases in the oleum treated p-SWNT, its D band was weaker than that of p-SWNT. This indicated that SWNTs were not functionalized or oxidized by oleum. The decrease of RBM in oleum treated SWNT was a result of decreasing Raman resonant enhancement.

Further narrowing of the G band and a significant increase in D band intensity were observed upon functionalization (figure **4.6**c). Usually the metallic SWNTs were more reactive than semi-conducting ones when reacting with diazonium salt. [134] After the reaction, the extended π-conjugation of SWNTs was disrupted and the electrons were localized, which caused the disappearance of the van Hove singularity transitions. Since

the Raman enhancement was associated with the energy separation between the first pair of DOS singularities of metallic tubes, it would vanish with loss of the van Hove singularities. The intensity of the D band can be used to probe the degree of functionalization. The strengthened D band indicated the formation of covalent bonds to the SWNTs. Compared with the Raman spectrum of oleum-treated SWNT, it was clear that the disruption of sp^2 network in SA-SWNT was caused by diazonium reagent. Besides the change on the tangential mode, the RBMs also sharply decay due to the attached functional groups.

When the SA-SWNT was heated in Ar at 600˚C for 1 h to remove the functional groups, there was an approximate 20wt% weight loss brought about by this annealing step. This indicated that about one sulfonic acid group was appended per 50 carbon atoms in the SA-SWNT. Elemental analysis using XPS suggested one sulfur atom, i.e. sulfonic acid group per 26 carbon atoms. Although the results differ by a factor of two, this is actually reasonably good agreement between the XPS and TGA measurements when we take into account the fact that XPS is a surface rather than a bulk measurement. The Raman spectrum of the annealed SA-SWNT verified the integrity of the SWNT skeleton. Almost all of the features of p-SWNT were restored, including the RBM, resonance enhancement and weak D band. This indicated that the functionalization did not destroy the skeleton of the SWNT and that the process was reversible.

Images of SA-SWNT were also taken with high resolution transmission electron microscopy (HRTEM). Compared with the purified SWNTs, which are in bundles and which have a tendency to agglomerate into thick membranes, the SA-SWNTs are much

easier to disperse on a carbon grid. They are constituted from much smaller bundles and some isolated tubes due to the exfoliation brought about by functionalization. From comparisons of many images, which are representative, it is clear that the bundles become much smaller and the number of isolated SWNTs increases after functionalization. In Figure **4.7** thin bundles with only 2 - 4 nanotubes on which the functional groups attached can be clearly seen.

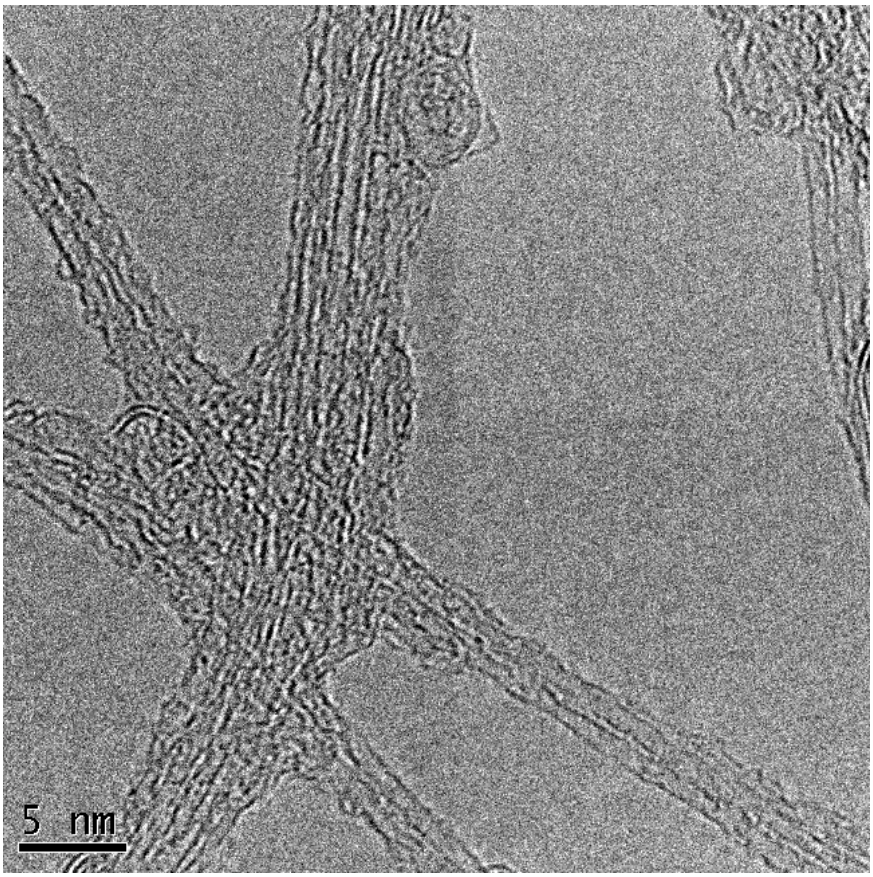

Figure **4.7** HRTEM image of SA-SWNT. Thin bundles of SWNTs with 2-4 nanotubes can be seen.

4.3.3 Synthesis and characterization of PFA-SWNT

Once the PFA-SWNT suspension was obtained by ultrasonication of the SA-SWNT in FA, it was subject to characterizations, such as contact angle, SEM, Raman spectra and FT-IR, to confirm the structure as proposed in figure **4.2**.

After SA-SWNTs were ultrasonicated in FA and poured into large amount of water, a significant change in the water solubility was observed upon wrapping of PFA around the SWNT (figure **4.8**a, b). Due to the hydrophilic nature of the sulfonic acid group, SA-SWNTs were well dispersed in water and the solution was dark; however, after being treated with FA (PFA-SWNT), they became insoluble and the solution was clear with the nanotubes lying at the bottom of the vessel. Since FA is miscible with water, the insolubility of the PFA-SWNT in water was due to the formation of PFA on the tube, since the PFA is quite hydrophobic.

Contact angles of water on a film of SA-SWNT versus on a film of PFA-SWNT were measured to confirm that a transition from hydrophilic to hydrophobic had occurred on SA-SWNT after being treated with FA (figure **4.8**c, d). For this objective, films of SA-SWNT and PFA-SWNT were prepared by casting them from a water suspension onto a 0.2 μ Anodisc filter membrane. The film of PFA-SWNT was washed thoroughly with water and acetone repeatedly to remove monomer FA and unattached PFA. The contact angle of water the SA-SWNT was ~40˚. The film of PFA-SWNT was hydrophobic with a much higher water contact angle of 90±5˚.

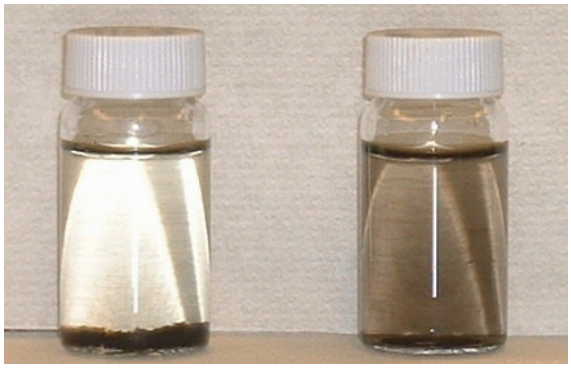

(a) (b)

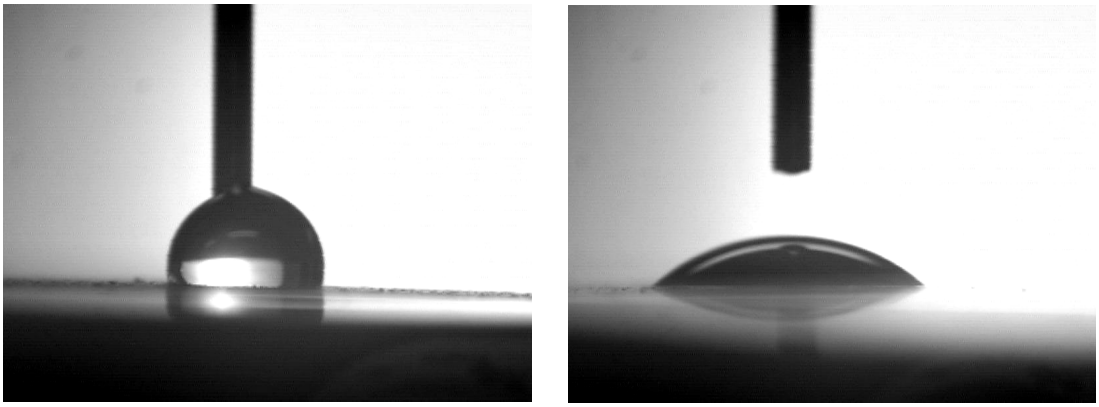

(c) (d)

Figure **4.8** Photograph of (a) PFA-SWNT and (b) SA-SWNT in water. PFA-SWNT showed a clear supernatant and precipitate versus SA-SWNT with a dark supernatant due to dispersion and solubility. Water contact angles of (c) PFA-SWNT and (d) SA-SWNT films.

Scanning electron microscopy (SEM) images were taken of both films on track-etch membranes (figure **4.9**). The morphology is similar for both SA-SWNT and PFA-SWNT. Bundles of SWNTs could be seen on both films without obvious size changes. The images of the washed PFA-SWNT membrane confirmed that the hydrophobic character did not arise through a simple covering of the nanotube mat by bulk PFA, thereby changing the contact angle.

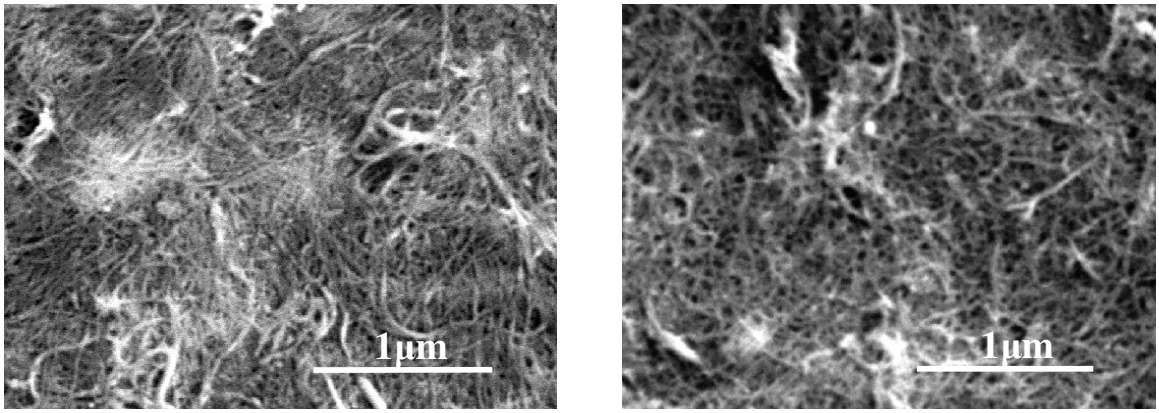

(a) (b)

Figure **4.9** SEM image of membrane of (a) SA-SWNT and (b) PFA-SWNT.

All of the above results indicated that PFA was formed on the surface of the SWNT after FA treatment and that the polymer was strongly bonded with SWNT because it could not be removed even after extensive washing and filtration.

Raman and FT-IR spectra were taken for isolated PFA-SWNT to investigate its structure. The Raman spectrum of PFA-SWNT (figure **4.10**) does not show a significant difference in either RBM or the tangential mode versus the SA-SWNT. The intensity ratio of the D band to G band (I_D/I_G) was almost the same with that of SA-SWNT (figure **4.6**c), suggesting that PFA wrapping did not alter the hybridization of the carbon atoms within the SWNT framework. It was consistent with the scheme shown in figure **4.2**, in which the PFA was only attached on the end of the sulfonic acid group. It was also observed that the RBM of PFA-SWNT became even weaker than SA-SWNT. This would be expected if the attachment of the macromolecule would restrict the radial breathing mode of the SWNTs more than the arylsulfonic acid group alone, a conclusion which seems logical.

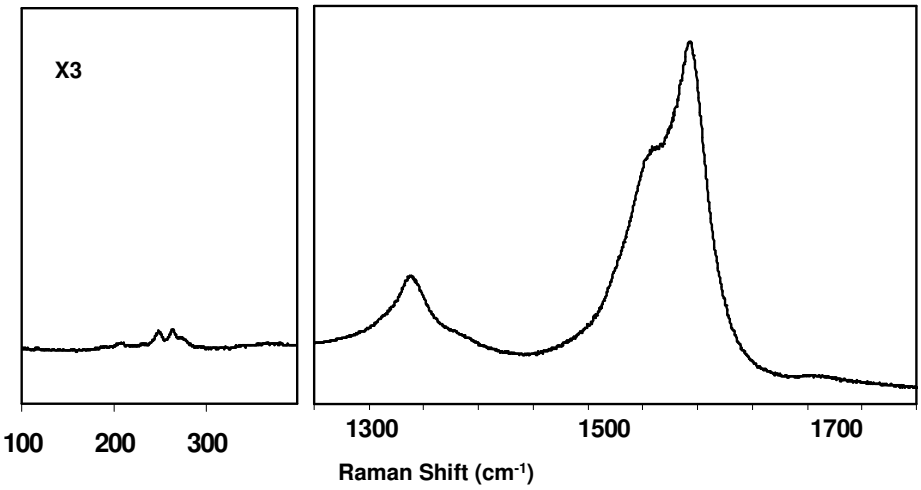

Figure **4.10** Raman spectra of PFA-SWNT. The spectra were normalized with the strongest G band and RBM were strengthened by 3 times.

IR spectroscopy is a useful tool in identifying the functional groups appended to the SWNTs. [76] Figure **4.11** shows the IR spectra of p-SWNT (A), SA-SWNT (B) and the PFA-SWNT (C). The large IR band observed at ca. ~3400cm^{-1} was attributed to asymmetrical stretching vibrations of traces of water adsorbed in the KBr pellet used for the analysis. The aromatic C=C stretch at 1627cm^{-1} is commonly seen in IR spectra of SWNTs. After functionalization, new bands at 1081 and 1045 cm^{-1} appeared which corresponded to the sulfonic acid group. It was interesting to note that the bands for PFA-SWNT shifted to lower frequencies by about 20 cm^{-1} compared with SA-SWNT. This clearly suggested that there could be ionic attractions between the sulfonic acid groups and the growing chains of PFA. The new signal at 1112 cm^{-1} was from the ether linkage in PFA, which is a proof of FA polymerization. Enhancement of the C-H stretching mode at 2922 and 2853 cm^{-1} also confirmed the existence of PFA.

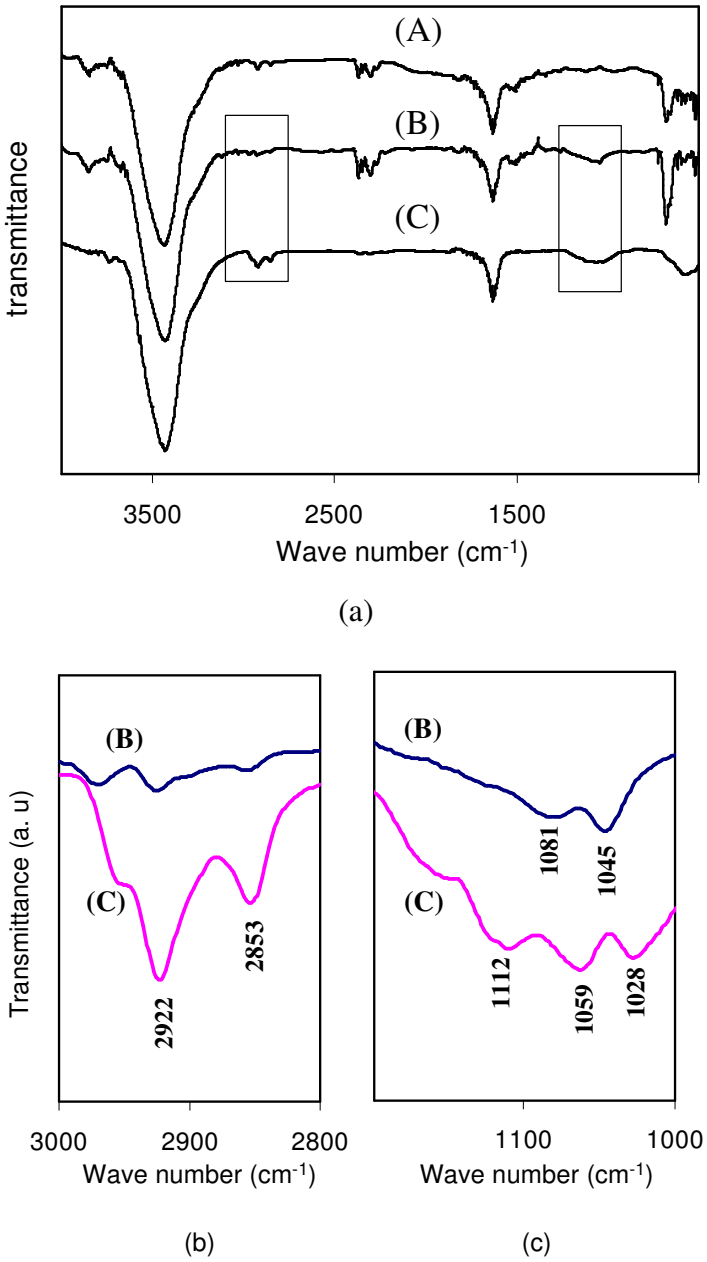

Figure **4.11** (a) IR spectra of p-SWNT (A), SA-SWNT (B) and PFA-SWNT (C); (b) expanded region of 3000~2800, highlighting the enhancement of C-H stretch; and (c) expanded region of 1200~1000, showing appearance of ether linkage and shift of sulfonic acid group stretch.

4.3.4 Synthesis and characterization of NPC/SWNT nanocomposite

PFA-SWNT was pyrolyzed under the same conditions as used to anneal the SA-SWNT. Upon pyrolysis, the PFA wrapped around the SA-SWNT was converted into NPC. The resulting NPC/SWNT nanocomposite was characterized with HRTEM and Raman.

The Raman spectrum of NPC/SWNT showed strong RBMs, as did the p-SWNT and the annealed SA-SWNT (figure **4.6**d). Although wrapped with PFA, the heat treatment in inert gas could still cleave the arylsulfonic acid group from the SA-SWNT to restore the spectroscopic signature of the p-SWNT. The restoration of the RBMs means that the SWNTs are intact after ultrasonication and, more importantly, even after pyrolysis.

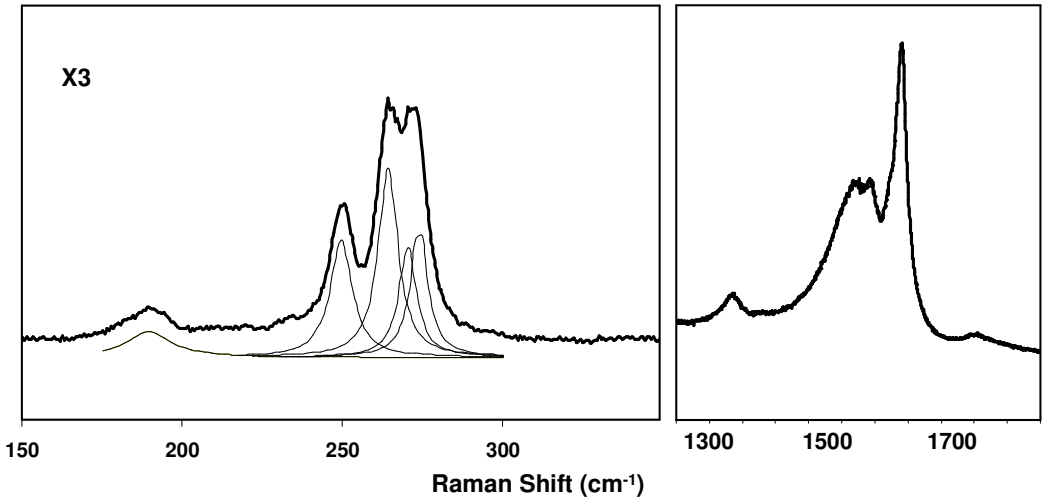

Figure **4.12** Raman spectra of NPC/SWNT. The spectra were normalized with the strongest G band and RBM were strengthened by 3 times.

By decomposing the RBM with Lorentzians, it was found that all the bands of NPC/SWNT were shifted to higher wavenumbers compared with p-SWNT and FWHM kept almost the same (Table **4.1**). All of RBM of the metallic SWNTs shift by 2-3 cm^{-1} and the semiconducting SWNTs with diameters of 1.30 nm shift by 5 cm^{-1}. These shifts were attributed to molecular forces being exerted by the NPC on the SWNT. Since the RBMs of NPC/SWNT have intensities comparable to that of the p-SWNT and annealed SA-SWNT, it is assumed that there is no chemical bonding between the SWNTs and the NPC. However, the existence of NPC around the SWNT may restrict the C-C stretching along the radial axis, leading to higher energy emission from the same modes. Compared with the SWNT/NPC composites prepared in chapter 3, in which the RBM had no frequency change, it was obvious that there was strong interaction between NPC and SWNTs through pyrolysis of PFA grafted SWNTs. Very small downshifts of RBM frequencies were observed for the annealed SA-SWNT. It was attributed to the splitting up of the SWNT bundles, resulting in smaller interaction between tubes.

Table **4.1** Comparison of Raman factors of RBM of p-SWNT, annealed SA-SWNT and NPC/SWNT.

RBM / **Sample**	1		2		3		4		5	
	ω	**FWHM**	**ω**	**FWHM**	**ω**	**FWHM**	**ω**	**FWHM**	**ω**	FWHM
p-SWNT	185	13.7	247	9.0	262	7.6	268	7.1	271	5.9
Annealed SA-SWNT	184	13.9	246	8.7	261	7.5	266	7.2	270	5.7
NPC/SWNT	190	15.9	250	8.3	264	7.5	270	6.7	274	6.4

ω: Raman frequency
FWHM: frequency width at half maximum

In the tangential mode, by comparing the spectra of NPC/SWNT (figure **4.12**) with the annealed SA-SWNT (figure **4.6**d), it was found that NPC/SWNT had a slightly stronger D band than the annealed SA-SWNT. Although the NPC had a higher I_D/I_G than that of SWNT, the absolute tangential mode intensity was much lower due to lack of van Hove singularities in NPC. Hence, when the amount of NPC and SWNT is comparable in the composite, the NPC component contributes little to the overall intensity of tangential mode of the composite. Although the exact concentration of NPC in the NPC/SWNT nanocomposite cannot be measured directly, the approximate weight ratio of NPC to SWNT can be calculated by the weight change during the synthesis of the NPC/SWNT nanocomposite. Usually, this ratio is from 1:1 to 2:1 in the nanocomposite prepared with the method described above. So the D band increase could not be attributed to the existence of NPC only. Actually, when PFA-SWNT was pyrolyzed, there was volume shrinkage of the PFA, which may cause stress between the NPC and the SWNT. This stress will disrupt the symmetry of the graphene plane. Therefore it is more likely that the small enhancement in the D band intensity is caused by the molecular interaction between NPC and SWNT.

The NPC/SWNT nanocomposite retains the thin bundle structure similar to that of the SA-SWNT as shown in the HRTEM images (figure **4.13**). A high magnification image of NPC/SWNT reveals that SWNTs are covered with some amorphous carbon. In another image showing an individual SWNT, it can be seen that there is a gap of 3-4Å between the NPC and the SWNT (figure **4.13b**). This indicates a van der Waals interaction rather than covalent bonding between the two components. This is consistent

with the hypothesis made based upon the Raman spectra. All of these images imply that a continuous phase was formed between these two distinct types of carbon. Thus the preparation of a nanocomposite carbon with SWNT becomes possible by modifying the SWNT with carbonizable polymer.

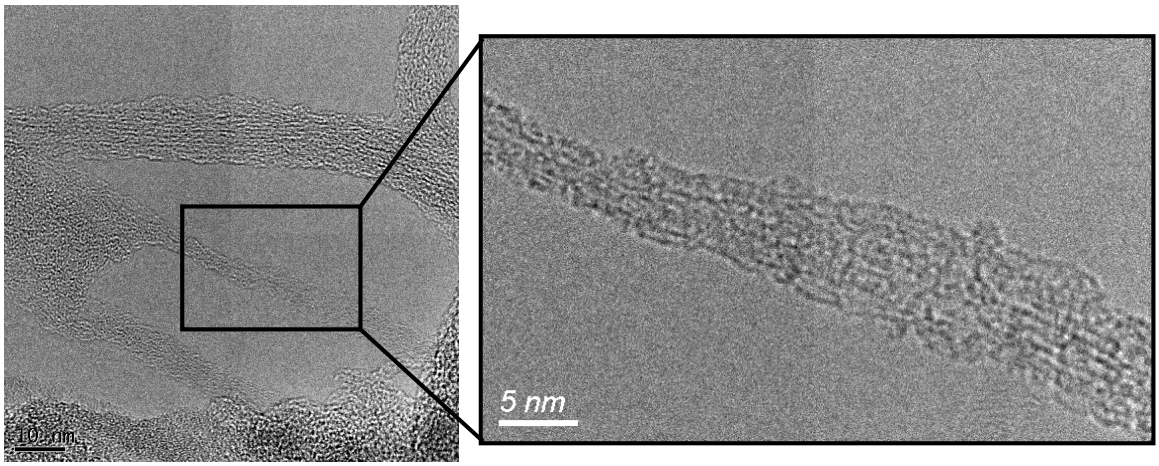

(a)

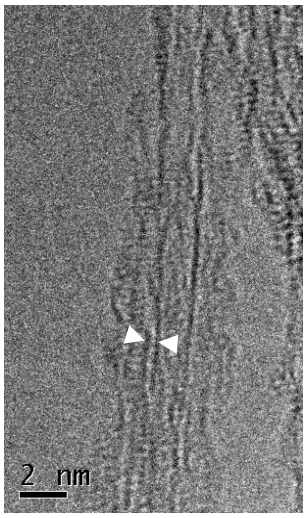

(b)

Figure **4.13** HRTEM of SWNT/NPC nanocomposite (a) SWNT bundles covered with NPC (b) individual SWNT surrounded with NPC. The white triangles are pointed to the gap between NPC and SWNT.

4.4 Summary and conclusions

A novel nanocomposite carbon was prepared by grafting a carbonizable polymer to SWNT. The SWNTs were first functionalized with a sulfonic acid group, which acted as a catalyst for FA polymerization, allowing the formation of PFA-wrapped SWNT (PFA-SWNT). Contact angle measurements and SEM images showed that the surface properties of the SWNTs were changed after being treated with FA. The IR spectrum provided further evidence of formation of PFA and electrostatic attraction between the sulfonic acid group and PFA. The formation of PFA-SWNT provided a way to overcome the inherently low interaction between pure SWNTs and the carbon precursor. Pyrolysis of the PFA-SWNT produced a nanocomposite carbon with NPC covering the SWNT. This procedure leads to intimate contact between the NPC and SWNT without affecting the integrity of the SWNT. A continuous phase is formed between the NPC and the SWNT which prevents the segregation of the SWNT from the NPC matrix. This suggests potential application of the PFA-wrapped SWNT in the preparation of advanced C/C nanocomposites.

Chapter 5

Deformation of NPC/SWNT nanocomposite at high temperature

5.1 Introduction

Carbon nanotubes, especially single wall carbon nanotubes (SWNTs), exhibit unusual mechanical and electronic properties, [9, 10, 35] which have made them the focus of much research – both fundamental and applied. [11, 135, 136] Although the CNTs have been subjected to extensive investigation, some of their basic properties remain obscure. For example, their behavior at high temperature and the structural deformations that result from such treatment are not fully understood, even though some experimental and theoretical studies of thermal stability of SWNTs have been undertaken. [137-144] These recent studies have shown that, smaller diameter SWNTs coalesce into larger diameter nanotubes at temperatures between ~1300-1400 ˚C, and these gradually transform to even more stable and more ordered structures – especially multiwall nanotubes (MWNTs). When treated at temperatures in excess of ~1600 ˚C

MWNTs or graphitic nanoribbons (GNR) are observed to form. Under even more forcing conditions, at temperatures higher than 2000 ˚C, all these intermediate and thermodynamically unstable allotropes of carbon tend to graphitize completely. The van der Waals force between nanotubes [145] may play an important role in the processes of deformation and coalescence that take place between them. Whereas, the interaction of SWNTs with each other has begun to be assessed, their interactions with other forms of carbon at high temperature have not been carefully studied; but it is just such interactions that are of critical importance to many of the applications envisioned for the SWNTs [43] For example the SWNTs are of considerable interest for preparing composites [11, 12] and among the many kinds of composites that could be very useful are carbon-carbon (CC) nanocomposites. Such materials may be multifunctional e.g. at one and the same time fulfilling the role of a structural element and while also being electronically active. This kind of multifunctionality could be among the more intriguing aspects of SWNTs. Therefore before applications of this kind can be pursued rationally, it is important to study the interaction and chemistry of SWNTs with other materials and in particular with other forms of carbon.

In the preparation of composites with SWNT, a strong interface between SWNTs and the host matrix would be necessary for good load transfer. [46, 146, 147] We have reported that a continuous interface was obtained in a nanoporous carbon (NPC)/SWNT nanocomposite, which was prepared by pyrolysis at 600 ^{o}C of the poly(furfuryl alcohol) (PFA) functionalized SWNTs. [148]

Because PFA is a crosslinking polymer, the NPC derived from it has a complex three-dimensional (3D) but non-crystalline, porous structure. Many very strong carbon-

carbon bonds need to be broken and rearranged in succession in order to graphitize PFA-derived carbon. Highly ordered graphite cannot be obtained from PFA-derived carbon even after prolonged heat treatment at 2800 ˚C. For this reason and based on decades of empirical versification, PFA-derived carbon has been dubbed “non-graphitizing” quite appropriately by scientists and technologists alike. However, PFA-derived NPC can be graphitized at temperatures in the vicinity of 2800 ˚C when it surrounds the carbon fibers included in “traditional” carbon-carbon (CC) composites. [49, 149] When alignment of the basal planes in the graphite derived from PFA-carbon occurs parallel to the fiber axis,, this creates a strong interface between the carbon fiber and the host carbon and excellent mechanical properties. It is the strength of this interface that controls the overall properties of the composite and not solely the intrinsic strength of the fibers. [150] Hence knowing whether graphitization can occur and understanding its causes in such systems is of more than just fundamental interest. However, at the fundamental level, it is considered that the formation of graphite at the micro-fiber interface in a CC composite occurs because during the heating process stress and strain accumulates at the boundary between the fiber and the NPC. It is these localized forces that cause graphitization to take place in the non-graphitizing carbon. The question then becomes is it reasonable to expect the same sort of effect to happen in a NPC/SWNT nanocomposite, since the SWNT would have to cause a similar effect to that of the carbon fiber, although it is many orders of magnitude smaller in diameter. The answer to this question is at the core of creating new nanoscale carbon composite structures. In this chapter, the deformation of the NPC/SWNT nanocomposites at temperatures between 1200 - 2000 ˚C is reported.

5.2 Experiments

5.2.1 Preparation

The NPC/SWNT nanocomposite was heat treated in a high-temperature vacuum furnace ("Red Devil" R. D. Webb Inc.). Preparation of the NPC/SWNT was described in Chapter 4. In a typical process of heat treatment, ~5mg of NPC/SWNT were placed in the furnace and degassed at 10^{-5} Torr and 200 ˚C overnight. After degassing, the furnace was heated to the target temperature at a rate of 10 ˚C/min and kept at that target temperature for 2 h. Samples were prepared in this way with final heat treatment temperatures (HTT) of 1200 ˚C, 1400 ˚C, 1600 ˚C, 1800 ˚C and 2000 ˚C. Pure NPC samples prepared from PFA were also treated at 1200 ˚C, 1800 ˚C and 2000 ˚C ie. at the similar conditions to provide control samples.

5.2.2 Characterization

After heating, the samples were allowed to cool under vacuum and were then taken from the furnace and dispersed in ethanol (Aldrich) for high resolution transmission microscopy (HRTEM) imaging and Raman spectral studies. Samples for HRTEM were made by dropping the suspension on a mesh of copper lacey carbon grids. HRTEM images were taken with a JEOL 2010F operating at 200kV. The point to point resolution was ~2Å. Samples for Raman spectroscopy were thin films formed by their dispersion on glass slides. Raman spectra were taken with a Jabin-Yvon Horiba T64000 micro-Raman spectrometer. Excitation was provided by an Ar-Kr laser at 1.5 mW incident power. An excitation wavelength of 514.5nm was used.

5.3 Results and Discussion

5.3.1 HRTEM images

An HRTEM image of NPC pyrolyzed at 800 °C is shown in figure **5.1**. It is a globally amorphous carbon lacking of long range order. The HRTEM images of NPC/SWNT prior to high temperature treatment (figure **4.13**) showed that SWNT bundles were covered with this type of amorphous carbon.

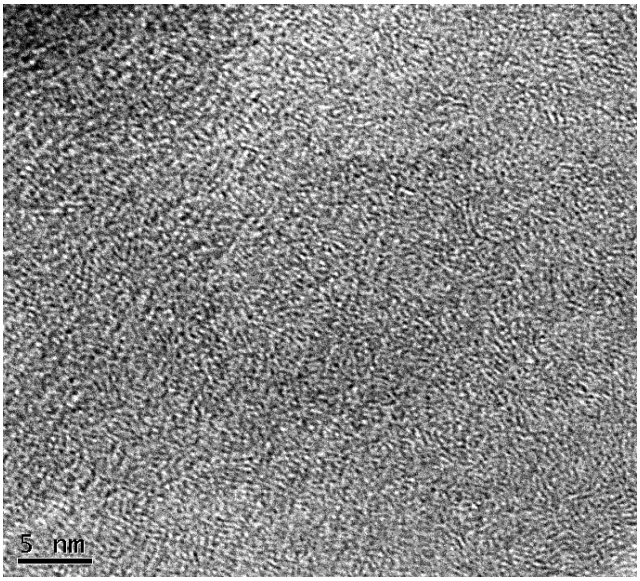

Figure **5.1** HRTEM image of PFA-NPC before HTT.

When the NPC was heated at 1200 ˚C, short range order of approximately 2 nm along the *a* axis and approximately 5 Å in *c* axis direction was observed (figure **5.2**a). No specific orientation preference could be found in this sample. When the NPC/SWNT nanocomposite was treated at this temperature, again very little ordering happened except at very short ranges (figure **5.2**b). A higher magnification image (figure **5.2**c) showed

evidence for a nascent templating effect of SWNT, in which the graphene sheets derived from the NPC did prefer to orient either along the nanotube axis or along the circumference. The blurring of the sidewall of the SWNT suggests the disruption of the SWNT when it was surrounded by NPC. However, some SWNTs also remained fully intact at 1200 ˚C if they were not interacting with the NPC (figure **5.2**d).

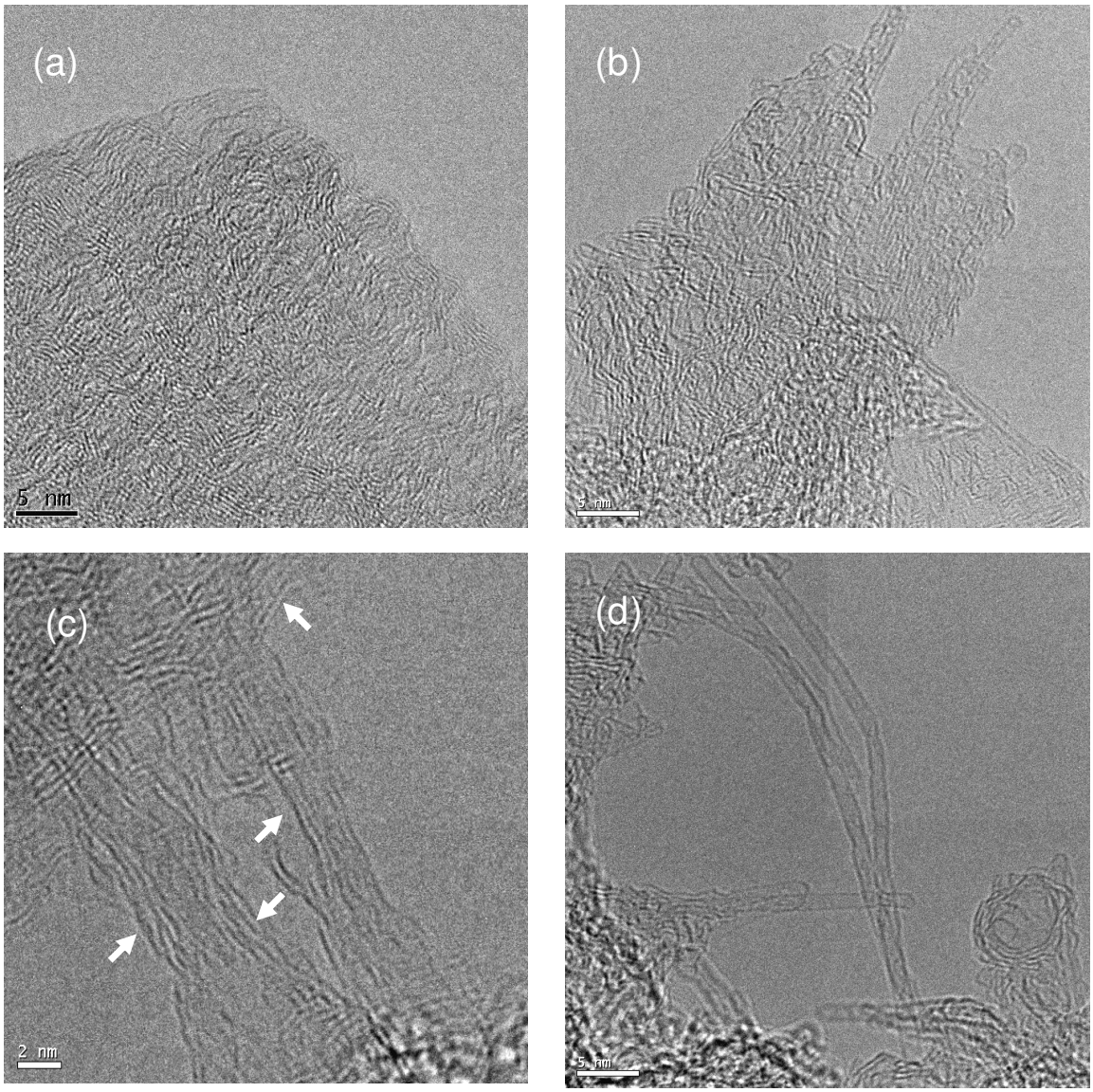

Figure **5.2** HRTEM images of (a) pure NPC treated at 1200˚C; (b)-(d) NPC/SWNT treated at 1200˚C. The arrows are pointed to the graphene sheets derived from NPC oriented along the SWNT axis or circumference.

When NPC/SWNT was heated at 1400 ˚C, large SWNTs with diameters > 2 nm appeared (figure **5.3**a), showing that the coalescence of neighboring SWNTs started at this temperature. At the same time, however, multilayer carbon shells were observed in this sample. It is noteworthy that these multilayer shells are not like the multi-wall nanotubes (MWNTs), which have pairs of graphitic shells as shown in TEM images. They come from graphitization of NPC. The extent of graphitization of NPC/SWNT increases with HTT (figure **5.3**a-c). Some double-wall nanotubes (DWNTs) and MWNTs appeared when HTT was conducted at temperatures higher than 1600 ˚C. Pure NPC also showed the trend of increasing order with temperature, but the structure was very different from that of graphite. Compared with the randomly aligned graphene sheets in the pure NPC treated at 1800 ˚C (figure **5.3**d), the NPC in the nanocomposite carbon exhibited a higher preference for ordering along the SWNT axis with increasing temperature.

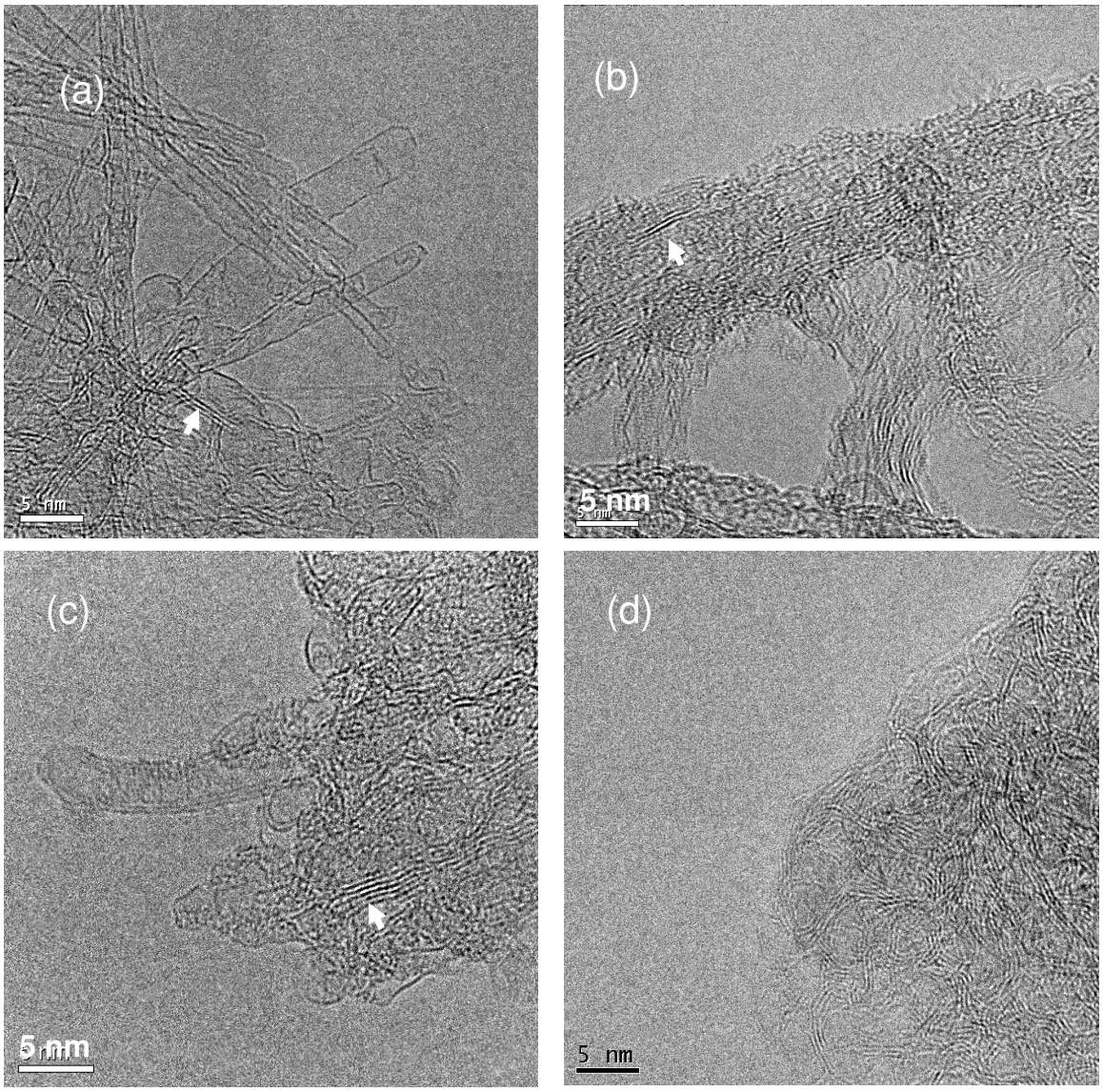

Figure **5.3** HRTEM images of NPC/SWNT treated at (a) 1400˚C; (b) 1600˚C; (c) 1800˚C and (d) pure NPC annealed at 1800˚C. The arrows are pointed to the multilayer carbon shells come from NPC graphitization.

Significant changes in the structure of the NPC were obtained when it was heated at 2000 ˚C (figure **5.4**a). Both the size of the graphene sheets and extent of their layering, increased compared with the sample heated at 1800 ˚C. Similarly, the NPC in the nanocomposite carbon was even more ordered. In contrast with pure NPC, the orientation

of the graphene sheets of NPC in contact with the SWNTs appeared to be exclusively along nanotube axis (figure **5.4**b, c), indicating a templating effect of SWNTs. These graphene sheets could be considered to be graphitic nanoribbons (GNR). It was also observed that when confined by the GNRs, the walls of the large SWNTs and some DWNTs collapsed into graphene sheets, with the result that the ends of these large SWNTs became "bulbs". When purified HiPco SWNTs in the absence of the NPC were treated at the same conditions, only multi-wall nanotubes (MWNTs) were found due to their broad diameter distribution. [141] However, in this nanocomposite carbon, since the SWNT bundles were segregated by NPC, the massive bond rearrangement taking place between neighboring SWNTs was reduced, resulting in lowered rates of formation of MWNTs. It is reasonable to assume that the stress accumulated at the boundary of the SWNTs and the NPC would apply significant and increasing pressure at the interface with increasing temperature. At 2000 ˚C the magnitude of the stress becomes large enough to collapse the SWNTs and DWNTs into graphene sheets. In the same sample we observed that some SWNTs with less NPC surrounding them survived intact even at 2000 ˚C (figure **5.4**d). There was also some amorphous carbon noted on the surface of other SWNTs in NPC/SWNT treated at 2000 ˚C. It was, however, obviously a different structure of carbon than that we have seen in the original NPC, so we attribute the source of this carbon to be from the so called "wipe-off" carbon atoms, which are derived from the SWNTs.

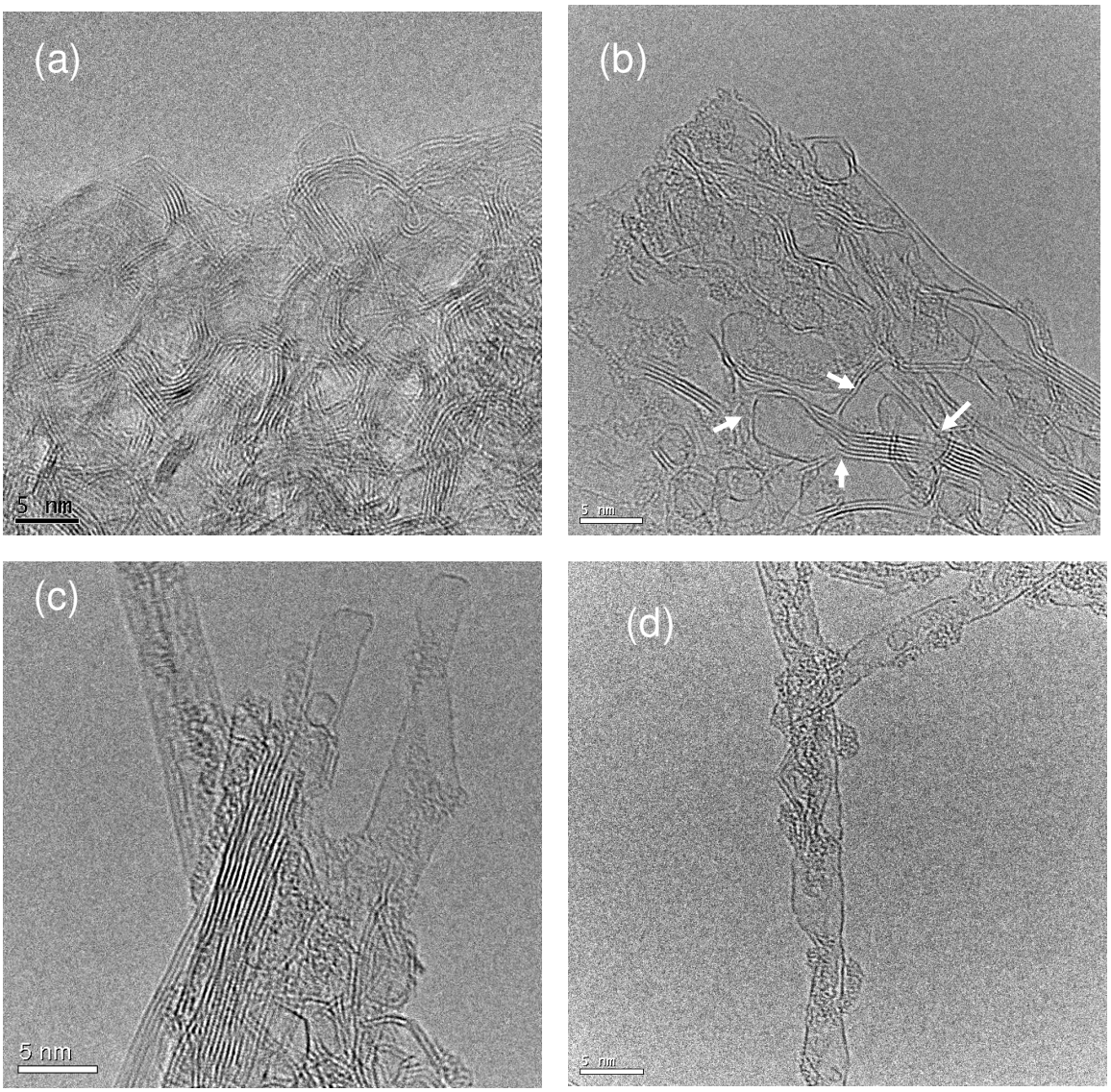

Figure **5.4** HRTEM images of (a) pure NPC and (b-d) NPC/SWNT each annealed at 2000 ˚C. The arrows are pointed to the "neck" between GNC and nanobulbs.

To summarize these results: the HRTEM images showed that the NPC alone behaved as a "non-graphitizing" carbon with only low levels of ordering and with no preferential orientation even after treatment at high temperatures. However, in the presence of the SWNTs, at high temperature (2000 ^{o}C) the NPC did begin to graphitize and did so with a strong preference along the tube wall and in parallel to the tube axis.

Other phenomena such as nanonbulb formation were also observed at the tube end. The imaging strongly suggested that solid state reaction chemistry between NPC and SWNTs does take place at the elevated temperature.

5.3.2 Raman spectra

Although HRTEM imaging provides clear pictures of the nanostructure deformation of NPC/SWNT, it is not by any means a method for obtaining statistically average behaviors. By contrast, Raman spectroscopy is quite sensitive to the subtle changes in the environment of the SWNTs and the spectra of bulk samples do provide "average" properties. Raman spectra of NPC/SWNT after HTTs are shown in figure **5.5**. For comparison, all the spectra were normalized by the highest intensity feature that of the G band at ~1590 cm^{-1}.

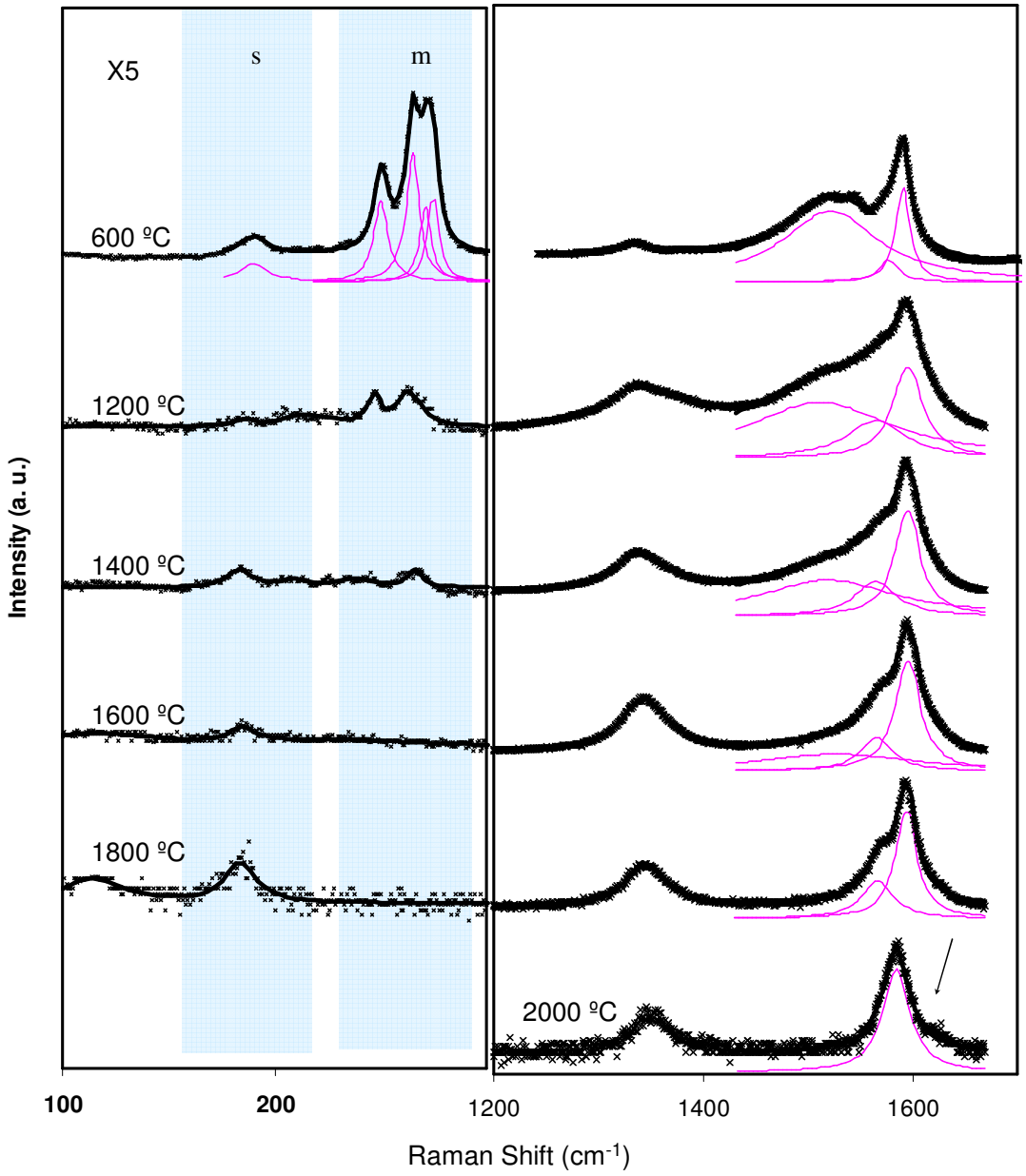

Figure 5.5 Raman spectra of NPC/SWNT after HTT. All the spectra were normalized with the strongest G bands. The RBM features from metallic tubes and semiconducting tubes are marked as "m" and "s" respectively. RBM of NPC/SWNT treated at 2000 ˚C was not shown because it was too weak to recognize.

In the NPC/SWNT nanocomposite before heat treatment, there are 3 main peaks at 250, 275, 273 cm^{-1} and a relatively weak peak at ~190 cm^{-1}. On the basis of Kataura plot [111, 112] and Eq **2.26**, [110] these peaks arise from the metallic SWNTs with diameters between 0.85 - 1 nm and the semi-conducting tubes SWNTs having diameters of approximately 1.3 nm. The RBMs of the SWNTs decayed dramatically when NPC/SWNT was heated at 1200 ˚C and there was also a sudden increase in the D band intensity at the same time. These changes showed that a dramatic increase in defect concentration in the SWNTs had taken place. It is noteworthy that in reports dealing with SWNT coalescence, Raman spectra observation, the same methodology used here, there was no observation of an increase in defects during or after the coalescence of SWNTs took place. [139, 143] This indicates that either defects did not form during SWNT coalescence or that the defects were annealed immediately at times less than experiment time (~15min). Clearly, based on the experiments detailed here defects did form during the coalescence of the SWNTs with NPC and the defects were persistent in time. From HRTEM images, we noted that some disruption of the SWNT walls was found at the boundary of the SWNTs and the NPC. Therefore it is evident that SWNTs coalesce with neighboring NPC and the process lead to formation of “defective” SWNTs even at temperatures as low as 1200 ˚C. The reason for reaction to form defects in the SWNTs must be that the NPC is a lower energy form of carbon than the small diameter SWNTs but it may also have sites at edges that are highly reactive. When the NPC is in contact with carbon at the surface of a small diameter SWNT a reaction pathway becomes available with a low enough activation energy barrier for carbon to transfer from the SWNT to a site on the NPC which is more thermodynamically stable. This leaves a

vacancy on SWNT surface. By comparison defect formation at the surface of the SWNT by evaporation of a carbon atom to vacuum has a set of large energy barriers to prevent it from occurring and it is wholly thermodynamically unfavorable.

Pressure accumulation on the boundary can also lead to a weakening of the RBM. Significantly, in a paper it was reported that the RBM of the SWNTs suddenly disappeared at pressures higher than 1.5GPa. [109] In natural graphite/glassy carbon composites, the stress on the boundary due to thermal expansion of graphite can be as high as kilobars.[151] Due to the orders of magnitude smaller size of the SWNTs compared to the micron-sized natural graphite particles and due to the stronger volume change that accompanies the thermal treatment of NPC, the stress at the boundary of SWNTs and NPC is expected to be orders of magnitude larger than that at the boundary of graphite and glassy carbon; thus it could very well be in the GPa range. Such a high stress would provide the force necessary to deform the SWNT and to affect the intensity of this vibrational mode.

A new band at approximately 120 cm^{-1} corresponding to the double-sized SWNT could not be identified until the HTT was taken to 1800 ˚C. This is because the intensities of the RBMs are known to decrease with tube diameter, which makes the RBM of the coalesced tubes too weak to observe. Thus the RBMs disappeared completely when the sample was treated at 2000 ˚C. Although small numbers of double-sized SWNTs survived at this temperature, they were highly defective and had no contribution to RBM.

The G band of the SWNTs actually contains several components. In order to evaluate the thermal evolution of the NPC/SWNT nanocomposite in detail, curve fitting with Lorentzians of the band intensities was carried out for the G band from all the

samples. The resultant Raman parameters are listed in Table **5.1**. A minimum number of Lorentzian curves were used to fit the data in every case.

Table 5.1. Raman factors of tangential mode of NPC/SWNT treated at different HTT temperature.

HTT temperature (˚C)	G band (cm^{-1})		D band (cm^{-1})	I_D/I_G
	ω	FWHM	Ω	
Before annealing	1591	16.2	1335	0.04
1200	1596	35.1	1340	0.18
1400	1595	28.9	1339	0.22
1600	1596	29.1	1343	0.36
1800	1594	25.0	1345	0.33
2000	1584	30.9	1350	0.54

ω: Raman frequency

FWHM: frequency width at half maximum

I_D/I_G: Intensity ratio of D band over G band.

The most intensive component of the G band near 1590 cm^{-1} is associated with the ordered sp^2 hybridized carbon vibration along the nanotube axis. [115] Broadening of this component was observed after heat treatment, even for an HTT of 1200 ˚C, which was a sign of more disorder in the graphene structure of SWNT walls. The broadening of the G band, the intensity increase in the D band, and the decrease in the RBM confirmed the formation of defects on SWNT walls due to heat treatment. Another change in the G band component near 1590 cm^{-1} was a shift to higher frequency (in wavenumbers) after HTTs in the range from 1200-1800 ˚C. It has been well established that both the tangential mode and the RBM shift toward higher frequency with increasingly higher pressure. [109, 152] Since there is significant volume shrinkage of the NPC upon heating, this will cause further stress accumulation at the boundary of the SWNT and the NPC. From the molecular point of view, this deformation of the NPC at high temperature may

apply pressure directly to the SWNT. Therefore we attribute the G band upshifts also to stress accumulation at the boundary between SWNT and NPC.

When NPC/SWNT was heated at 2000 ˚C, the RBM became too weak to record, and the G band reduced to only one component at ~1584 cm^{-1}, showing now that graphitic carbon was the predominant in the sample. The full width at half the maximum (FWHM) of the G band is ~31 cm^{-1}. Usually, the G band of well-ordered graphite or MWNTs with inner diameter larger than 3-5 nm is located at approximately 1582 cm^{-1} with a FWHM of ~18 cm^{-1}. The shift of G band to higher frequency (in wavenumbers) was found in some samples with extremely small crystal sizes. [113, 115] Additionally, there is also a small shoulder located at ~1620 cm^{-1} with the main G band, which is usually assigned as D′ or G^* band. This feature is associated with the edge planes of the graphene sheets. [153] The upshift and broadening of the G band compared to graphite, and the appearance of the D′ band, together with the increase in the intensity of the D band, confirmed the finite lateral size of the GNR layers and that there are only a limited number of layers of in any GNR stack, both of which were consistent with the HRTEM images.

The narrow shoulder of the G band - in the vicinity of 1570cm^{-1} is related to the vibration along the circumference of the SWNT and this frequency is diameter dependent. [154] The circumferential frequency was observed to downshift slightly upon heating, an observation similar to that of heat treatment of the DWNTs. [142] It could be evidence for small tubes coalescencing or decomposing. The broad shoulder of the G band with a maximum at ~1520 cm^{-1} is associated with the energy separation ($E_{11} = E_{c1} - E_{v1}$) between the first pair of electronic density of states (DOS) singularities in the

valence (*v*) and conduction (*c*) bands of the metallic nanotubes. [105] This feature of metallic tubes decreased gradually with increasing HTT and vanished completely when the HTT was done at 1800 ˚C or higher. It is consistent with the change of RBM, in which the signature of the metallic tubes disappeared in HTT of 1800 ˚C. It shows that smaller nanotubes are less thermally stable than are the larger nanotubes.

5.4 Summary and conclusions

In summary, the SWNTs and the NPC affect each other during high temperature heat treatment. From a thermodynamic point of view, both the NPC and the SWNT are metastable structures. Thus there is a free energy driving force for transforming them toward the more stable structure of graphitic carbon at high temperature. The free energy can be released only if there is a pathway with a low enough activation barrier for the transformation to happen in experimental time. However, the final products of high temperature heat treatment of either NPC or SWNTs when not in contact with each other,and when done on each separately are detectably different from each other because their morphologies are so different in their starting states. The 1D SWNTs transform to 1D MWNTs or 1D GNRs; the NPC transforms to semi 2D GNRs. However, the pathways available to the NPC and SWNTs when they are present together and in contact with one another in the NPC/SWNT nanocomposite and treated at high temperature are quite different than those available to either component. As a result the deformations and structural outcomes at high temperature lead to new morphologies in the NPC/SWNT nanocomposite.

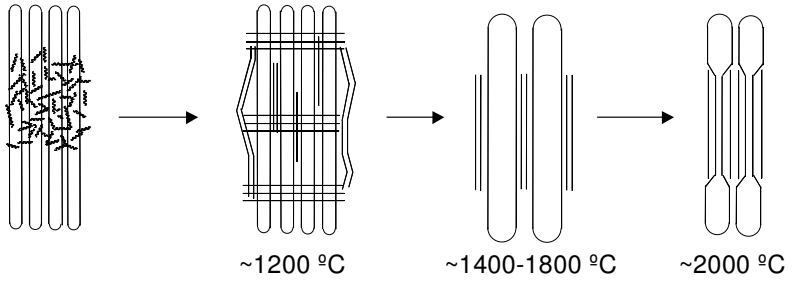

Figure **5.6** Scheme of NPC/SWNT nanocomposite deformation under HTT.

Figure **5.6** outlines the transformation of the NPC/SWNT nanocomposite due to high temperature treatment. When the NPC/SWNT was heated at ~1200 ˚C, the NPC was partially graphitized. The orientation of the NPC was only slightly affected by SWNTs and with most nanodomains lying mostly parallel along nanotube axis, but many also lying across the circumference at an angle to the axis. Although the SWNTs remained intact when treated alone at this temperature, at the interface of SWNT and NPC new reaction pathways, thermodynamics and stress accumulation caused deformation of NPC caused chemistry the disruption of SWNT walls. When HTT was done in the range of 1400-1800 ˚C, the SWNTs started to coalesce into double diameter tubes. With a further increase in the HTT, the extent of graphitization of the NPC increased and the formation of graphene sheets along nanotube axis became dominant. At approximately 2000 ˚C, the NPC was completely graphitized into GNRs because of the template effect of SWNTs. At the same time, forces induced by NPC confinement collapsed SWNTs and DWNTs into GNRs, but when the ends of the tubes not in contact with the GNRs, they bulged to produce the “nanobulbs” that were observed.

Chapter 6

Properties of SWNT/ NPC nanocomposites prepared with SA-SWNT

6.1 Introduction

The sulfonic acid functionalized SWNT (SA-SWNT) is compatible with both of FA and PFA, thus it becomes possible to prepare SWNT/NPC nanocomposites containing individual SWNTs. In Chapter 4, the PFA-SWNT was separated from its FA suspension for characterization. If it was kept in FA and the FA continued to polymerize, a uniform dispersion of isolated SWNT in PFA could be obtained because PFA-SWNT was compatible with both FA and PFA. In this Chapter, SWNT/NPC nanocomposites with low SWNT concentrations were prepared with such a protocol. Two important characteristics, the extent and rate of gas adsorption and the mechanical properties of the SWNT/NPC nanocomposites were investigated.

The results shown in Chapter 3, indicate that the mass transfer and adsorption rates in the SWNT/NPC composites was higher than that of the original PFA-NPC. The adsorption experiments revealed that the exterior surface of SWNT bundles was the most important factor for modifying the behavior of the NPC and in increasing the mass transfer rate. However, the extent of this augmentation in rate was not large when the SWNT concentration in the composite was lower than 50 wt%. This is because most of the nanotubes were confined in bundles and as such they had much less exterior surface exposed for transport Schematics of the structures of the NPC, the SWNT/NPC composite, and the SWNT/NPC nanocomposite are shown in figure **6.1**. It is clear that isolated individual SWNTs can provide much more exterior surface than the SWNT bundles at the same mass, thus with the nanocomposite it may be possible to obtain higher augmentation of the rate at lower SWNT loading. In this chapter, the SWNT/NPC nanocomposite was prepared by ultrasonicating SA-SWNT in FA followed by pyrolysis. The FA polymerization was catalyzed in situ by the sulfonic acid groups on SWNT. Pore size distribution (PSD) and mass transfer rates for the SWNT/NPC nanocomposites were studied by CH_3Cl adsorption.

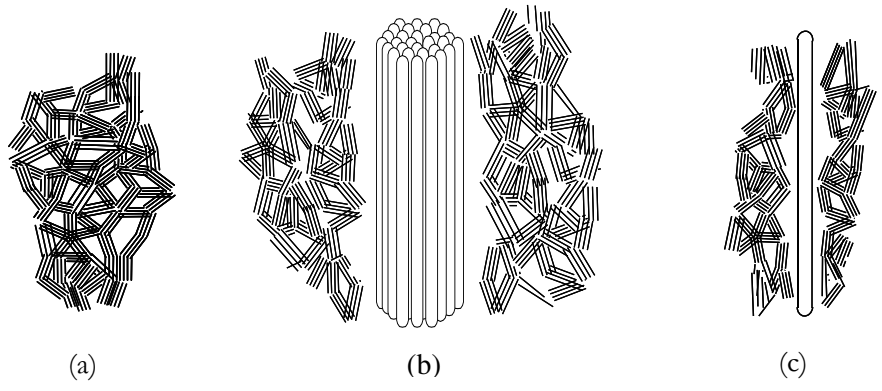

Figure **6.1** Schematic structure of (a) NPC, (b) SWNT/NPC composite with SWNT bundle; and (c) SWNT/NPC nanocomposite with individual SWNT.

In the research on SWNT composites, mechanical properties reinforcement is one of the most active areas of focus due to the small size and remarkable mechanical properties of SWNTs. [12, 60, 90-92, 155-157] Since pyrolyzed PFA is often used as a binder in CC composites, [8, 48, 49, 149] enhancement of mechanical properties might be of interest in such applications. To study the effect of individual SWNT in improving mechanical properties of pyrolyzed PFA, SWNT/NPC nanocomposite fibers were prepared and their tensile strength was tested.

6.2 Mass transfer rate in SWNT/NPC nanocomposites

6.2.1 Preparation of SWNT/NPC nanocomposites

The SWNT/NPC nanocomposites used for mass transfer study were prepared by adding ~0.5 - 3 mg SA-SWNT in 15 ml FA and dispersed with the ultrasonic processor (PGC Scientifics, 130W) at 70% of the maximum power amplitude. A cycle of 5 sec of ultra-sonication followed by a 15 sec pause was used. After 3 days, the mixture was poured in a quartz boat and pyrolyzed in flowing Ar at 600 °C for 8 h. As a control sample, NPC from FA (FA-NPC) was pyrolyzed at the same conditions. The resulting carbon samples were ground into powder for CH_3Cl adsorption to study the PSD and mass transfer rate.

6.2.2 CH_3Cl adsorption

The PSD of the nanocomposite carbon in the range of 4 - 300 Å was obtained by CH_3Cl adsorption under 4.5 - 650 torr and -25 - 30 °C. The mass transfer rate was studied with the transient uptake between 40 and 60 torr at 30 °C.

6.2.3 Results and discussion

The PSD and pore volume of the SWNT/NPC nanocomposites and the NPC from FA are shown in figure **6.2**. Since a very small amount of SA-SWNT was added to form the nanocomposite, there was not much difference between the PSD of the nanocomposites and that of FA-NPC. All of them had the same PSD with a maximum at ~5 Å.

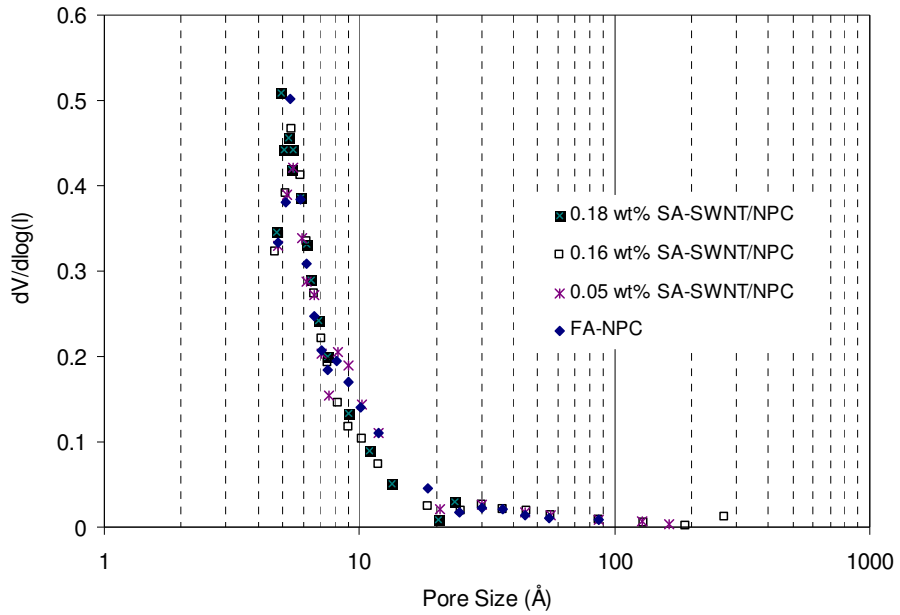

(a)

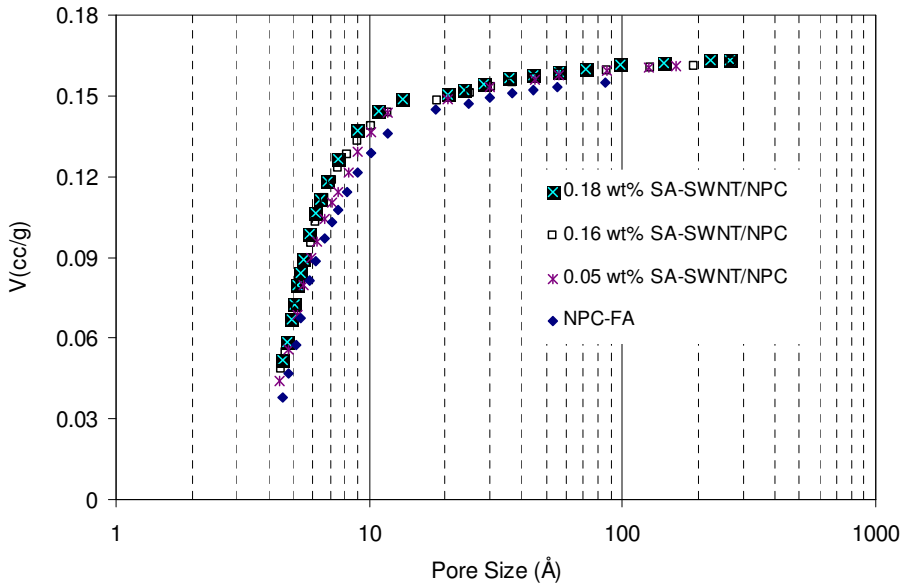

(b)

Figure **6.2** (a) PSD and (b) cumulative pore volume of nanocomposite carbon prepared from SA-SWNT/FA and FA-NPC.

Close observation of the accumulative pore volume with respect to pore size (figure **6.2**b) revealed small difference among them. These changes were plotted as the evolution of the ultramicropore, micropore and mesopore volumes versus SA-SWNT concentrations in nanocomposites (figure **6.3**). It can be found that the ultramicropore volume increased linearly with the SA-SWNT concentration while the micropore volume decreased linearly. The mesopore volume remained nearly constant with increasing nanotube concentrations.

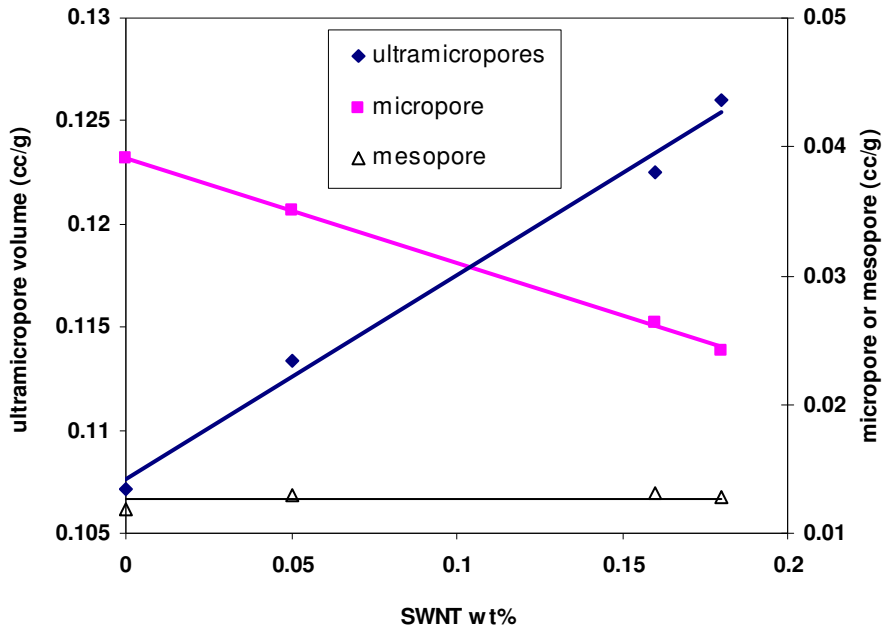

Figure **6.3** Ultramicropore (l < 7 Å), micropore (7 Å < l < 2 nm) and mesopore (2 nm < l < 30 nm)) volume evolution with SWNT concentration in nanocomposite carbon prepared from SA-SWNT dispersed in FA.

When the SWNT bundles are split, or exfoliated, more groove sites and exterior surface will be available on pairs of tubes and thin bundles compared with the original large bundles. Since SA-SWNTs were exfoliated and their thin bundles or isolated

nanotube structures survived pyrolysis, the SWNT/NPC nanocomposite displayed increased volumes of ultramicropores compared to those composites described in Chapter 3 with the same amount of SWNT. When SA-SWNT concentration was very small in the nanocomposites, agglomeration of SWNTs was minimized and the ultramicropores generated by the presence of the SWNTs increased linearly with their concentration in the nanocomposites. However, it did not mean that the increase was brought on only by the ultramicroporosity of the SWNTs. The slope of ultramicropore volume with respect to SWNT concentration was ~0.1 cc/wt% SWNT, corresponding to a value of 10 cc of ultramicropore volume created by each 1 g increase in SWNT content. Such a pore volume if it were to be pictured as being around each isolated SWNT, which it is now, would require an average void width of ~2.6 nm around each isolated SWNT. No such empty space around the SWNTs exits; and even if it did, it would not contribute to ultra-microporosity because the dimensions are too large. Therefore, the inclusion of ultra-microporosity from SWNTs was not the only reason for the change in behavior of the nanocomposite carbon.

The ultramicropores in NPC arise from the spacing between turbostratic layers, which are tortuous and corrugated channels containing many narrow necks. These necks at front of ink-bottle pores make part of the pores the lie with less accessible for gas molecules due to super slow mass transfer through them; and wholly inaccessible when they are blocked. With the incorporation of the SWNTs, the connectivity of the pore network within nanocomposites was enhance thereby increasing overall accessibility in the material,, thus the measurable ultramicropore volume of the nanocomposites was

increased. This effect was not so significant in SWNT/NPC composites prepared by solution blending in Chapter 3 because the SWNTs were not well enough to produce this effect through the majority of the solid since most of them remained confined in bundles.

The linear decrease of microporosity can arise in principal from two factors: the covering of SWNTs with NPC as described in Chapter 3; and by the improvement of ultramicropore connectivity. The first factor is not significant because the mesopore volume decreased with SWNT concentration with a slope of ~0.09 cc/wt%, suggesting that a mesopore volume of ~9 cc from per gram SWNTs was covered by NPC, which was too high for SWNTs. The second factor is more important factor in the apparent decrease in microporosity. When the ultramicropores are poorly connected, the mass transfer rate to them and within them is quite slow; therefore in experimental time the sample and the adsorbing gas do not reach true equilibrium. Hence measured mass uptake arises mostly from adsorption in the larger micropores and this mass will be lower than the "true" equilibrium value. For the micropore volume, the counting is not significantly affected by the mass transfer rate; but for the ultramicropores, an undercounting may occur due to the high resistance in these slit pores. When better transport through the sample is created with the inclusion of the SWNTs, within experimental time the sample comes much closer to the true equilibrium condition and all of the pores, especially the ultramicropores are well counted. That the mesoporosity did not change and remained constant suggested that the size of NPC microdomains did not change even after including the SA-SWNT, is a natural result of the low concentrations of SWNTs being deployed.

The increase in the mass transfer rate within the SWNT/NPC nanocomposites confirmed that the ultramicropores contributed from SWNTs played an important role (figure **6.4**). Since the data was taken between 40 to 60 torr under 30 °C, it was associated with the mass transfer through the ultramicropores with sizes between 5.85 Å and 6.18 Å. For FA-NPC, the mass transfer was controlled by both the resistance at the pore mouth and the diffusion in the ultramicropores. But for the SWNT/NPC nanocomposites, the barrier model can fit all of the date well, even for the nanocomposite with only 0.05 wt% SA-SWNT. This indicates that the diffusion through the ultramicropores in the nanocomposites was very fast so that the diffusion resistance became negligible. This was a result of improved pore network connectivity with the straight pores provided by SWNTs. At the same time, the pore mouth mass transfer coefficient k_b increased sharply by adding SA-SWNT. With only 0.05 wt% SA-SWNT in nanocomposite carbon, k_b increased by more than a factor of two. The effect the same extent of rate augmentation in the original SWNT/NPC composites, we needed a SWNT concentration of ~60 wt% (figure **3.10**) because most of the SWNTs were confined in bundles!

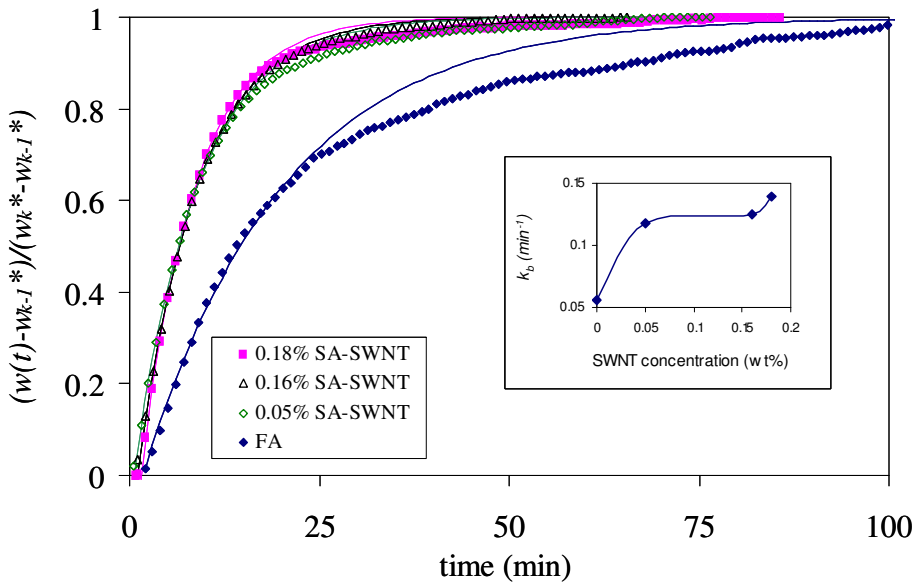

Figure **6.4** Normalized transient uptake $\frac{w(t)-w_{k-1}*}{w_k*-w_{k-1}*}$ of SWNT/NPC nanocomposite carbon and NPC-FA from 40 torr to 60 torr under 30 °C, where *w(t)* was the uptake at time *t*, w_k* was the equilibrium uptake at 60 torr, w_{k-1}*was the equilibrium uptake at 40 torr. All of them were fitted with barrier model and the pore mouth mass transfer constant k_b versus SWNT concentration was shown in inset.

6.3 Mechanical properties of SWNT/NPC nanocomposites

6.3.1 Preparation of SWNT/NPC nanocomposite fibers

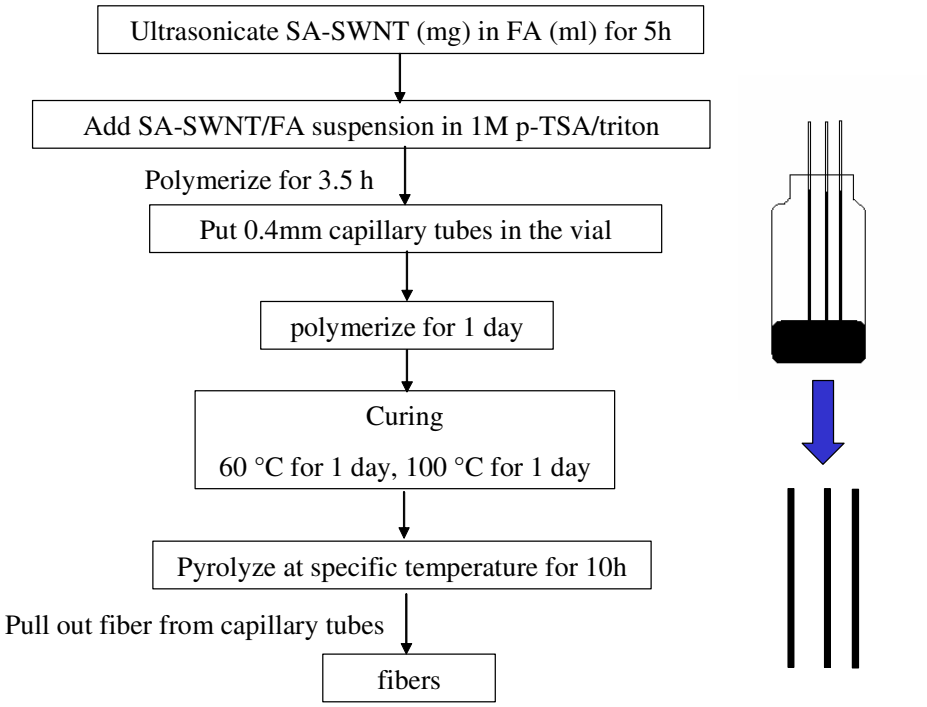

Figure **6.5** Scheme of preparation of SWNT/NPC nanocomposite fibers

The SWNT/NPC nanocomposite fibers were prepared with the process shown in figure **6.5**. In this process, 3 mg SA-SWNT were added to ~3 g FA and dispersed with the ultrasonic processor (PGC Scientifics, 130W) for 5 h. at 50% of the maximum power amplitude while the vial in which this was done was kept in an ice bath. A cycle of 5 sec of ultrasonication followed by a 5 sec pause was used. Then the 2.5 ml suspension was added to a 2.5 ml 1M p-TSA/triton solution with a syringe pump. The addition rate was

5.0 ml/h. The mixture was polymerized while stirring in an ice bath for 3.5 h before dipping the open ends of the capillary tubes into it. Capillary forces drew the mixture into the tubes. After 1 day of polymerization at room temperature, the capillary tubes with SWNT/PFA inside were put in oven at 60 °C for 1 day and 100 °C for another day to cure. Due to volume shrinkage, the resulting polymeric fibers could be pulled out of the capillary tubes after curing for measurements. They had diameters between 0.32 - 0.34 mm.

Carbon fibers were prepared by heating under flowing Ar at 300 – 600 °C the polymeric fibers so formed within the capillary tubes. The pyrolysis step was done at a specific temperature for 10 h. To avoid deformation of the capillary tubes and fracture of fibers, a very slow heating rate of 1 °C /min was used and the cooling rate was also kept low. After pyrolysis, the carbon fibers were pulled out of capillary tubes. The average diameter of carbon fibers decreased with increasing pyrolysis temperature, and it was ~0.25 mm at 600 °C.

To obtain carbon fibers at higher temperature, the fibers prepared at 600 °C were further pyrolyzed at 800, 1200, 1400 and 1600 °C for 10 h. The “Red Devil” (R. D. Webb Inc.) vacuum furnace was used for heat treatment above 1200 °C. Further Diameter shrinkage was not significant when pyrolysis temperature was raised to higher than 600 °C and the average value remained fixed at ~ 0.24 mm. As a control sample, polymeric PFA and carbonaceous NPC fibers were prepared with the same process.

6.3.2 Mechanical properties measurement

The SWNT/NPC nanocomposite fibers and NPC-PFA fibers were tested with an Instron 4202 at room temperature. The fibers were clamped with Instron fiber clamps and the maximum capacity is 5N; 10 kN Instron 2527 Dynacell was used to bring in strain forces. A testing length of 20 mm and a loading rate of 0.3 mm/min were used for fibers prepared at 500 ºC and below. A testing length of 10 mm and a loading rate of 0.2 mm/min were used for fibers prepared at 600 ºC and above.

6.3.3 Characterization

An SEM image of the fracture surface of the SA-SWNT/PFA fibers was taken with the Hitachi S3000-H SEM operated 5 kV. The bulk SWNT/NPC nanocomposite carbon was prepared with the same polymerization process as those of the nanocomposite fibers and was pyrolyzed at 800 ºC for 8 h. The carbon was ground in ethyl alcohol to make a suspension and it was dropped on the holey carbon-coated grids for TEM study. HRTEM images were taken with JEOL 2010F under 200 kV.

6.3.4 Results and discussions

The typical stress-strain profile of polymeric and carbon fibers are shown in figure **6.6**. It can be seen that the PFA and its nanocomposite fibers cured at 100 °C had a yield region, whereas the fibers tested after pyrolysis were quite brittle, and displayed properties attributable to unreinforced glassy carbon.

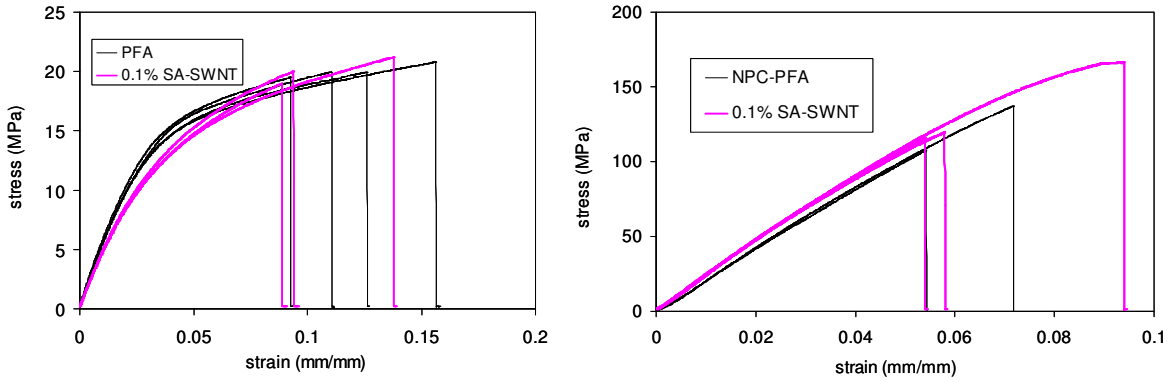

(a) (b)

Figure **6.6** Typical tensile stress-strain profiles of (a) PFA fibers and 0.1wt% SA-SWNT/PFA fibers cured at 100 °C; (b) NPC-PFA fibers and 0.1wt% SA-SWNT/NPC fibers pyrolyzed at 600 °C.

The Young's moduli of the NPC and SWNT/NPC nanocomposite fibers were calculated from their stress-strain profiles and compared in figure **6.7**. For the polymer fibers, the fibers with SA-SWNT had lower Young's modulus than the pure PFA fibers. However, SEM image of the fracture cross-section of this nanocomposite fiber did not show obvious voids or defects (figure **6.8**), indicating that the SA-SWNT was well dispersed in PFA. So the weakening effect may actually come from "defects" on SWNT. Although strong bonding between SWNT and PFA could be obtained through the sulfonic acid groups on SWNT walls, the functionalization is also known to disrupt the periodicity of the carbon network, thus diminishing the SWNTs strength.

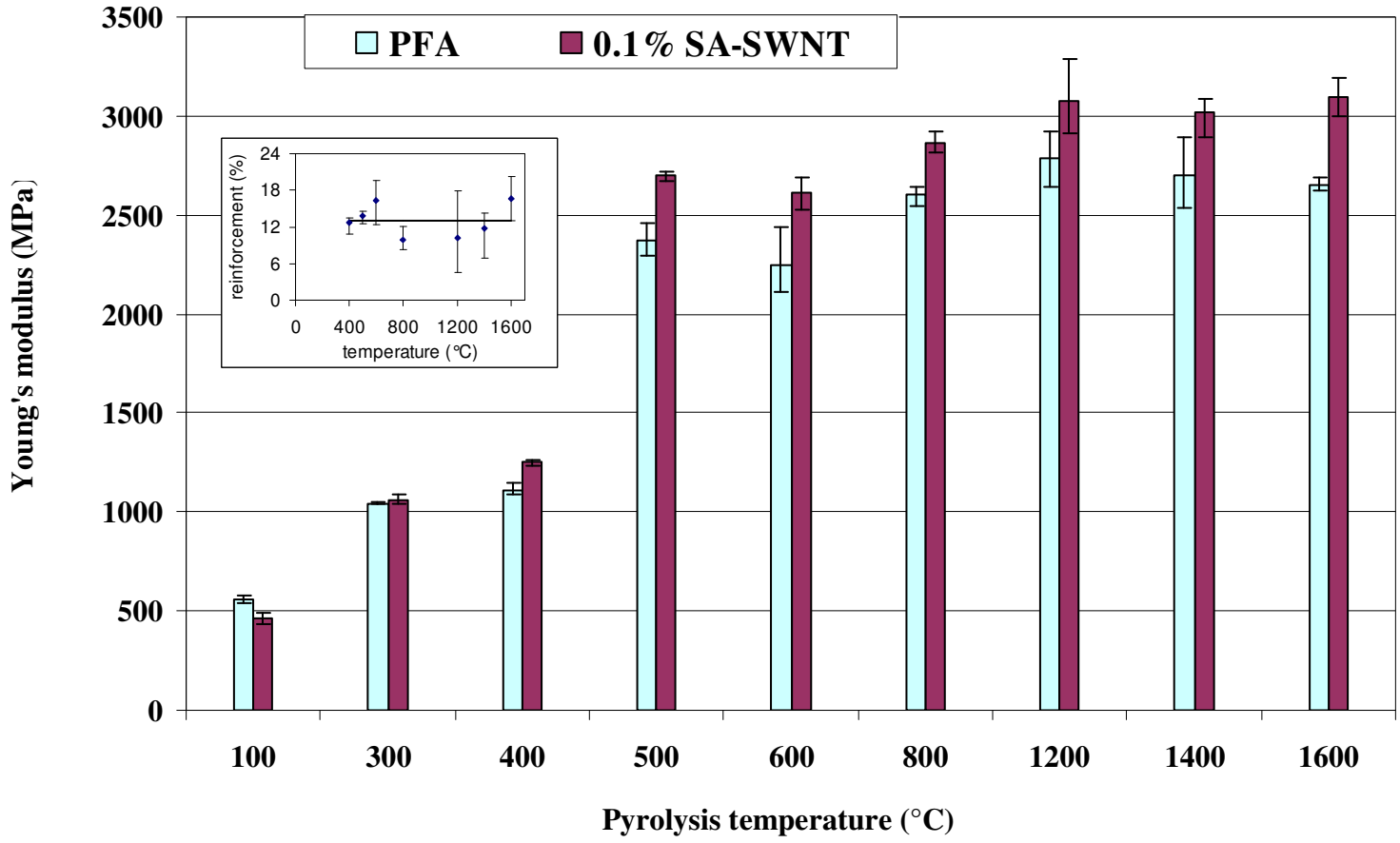

Figure **6.7** Young's moduli of the NPC-PFA and 0.1% SWNT/NPC nanocomposite fibers pyrolyzed at different temperature. Sample prepared at 100 °C were PFA and SA-SWNT/PFA fibers. The enhancement of SWNT for the fibers pyrolyzed at 400 – 1600 °C is shown in the inset.

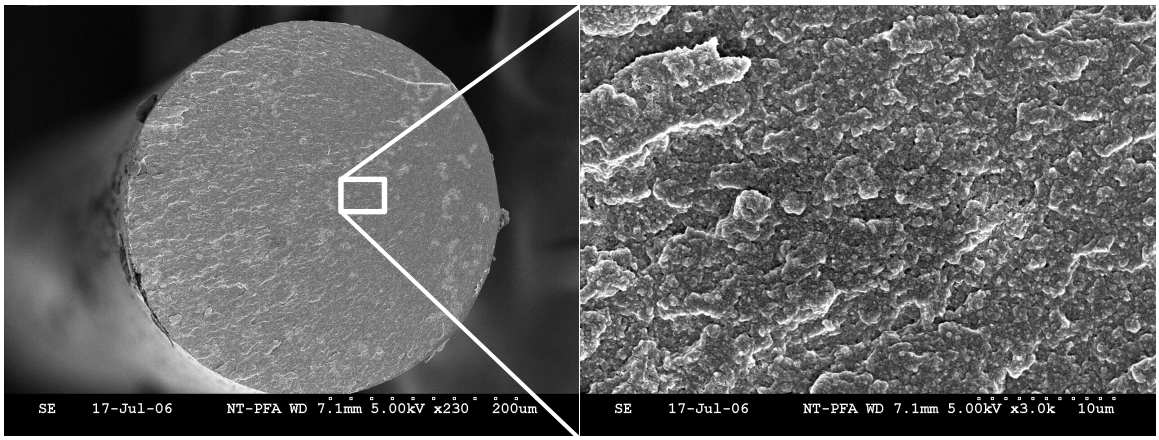

Figure **6.8** SEM image of SA-SWNT/PFA nanocomposite fiber at the fracture cross-section.

Upon pyrolysis, the functional groups were cleaved from SWNTs and their integrity was restored, resulting in SWNT reinforcement of the NPC matrix. The enhancement of the nanocomposite fibers treated at 400 – 1600 ºC was approximately constant with an average value of ~13 %, as shown in the inset of figure **6.7**.

The TEM image of the SWNT/NPC nanocomposite carbon prepared at 800 ºC showed finitely-size graphitic domains and nanobulbs (figure **6.9**). Based on results of the study in Chapter 5, it was easy to tell these were collapsed SWNTs arising from confinement by the NPC. Because the SWNT:NPC ratio here was orders of magnitude lower than that of NPC/SWNT nano-composites studied in Chapter 5, the SWNTs suffered more pressure from confinement of NPC at the same temperature. So the SWNTs collapsed at much lower temperature. However, the enhancement of nanocomposite fibers did not decrease with increasing temperature, showing these "collapsed" SWNTs still had strong mechanical properties and the ability to reinforce the NPC matrix.

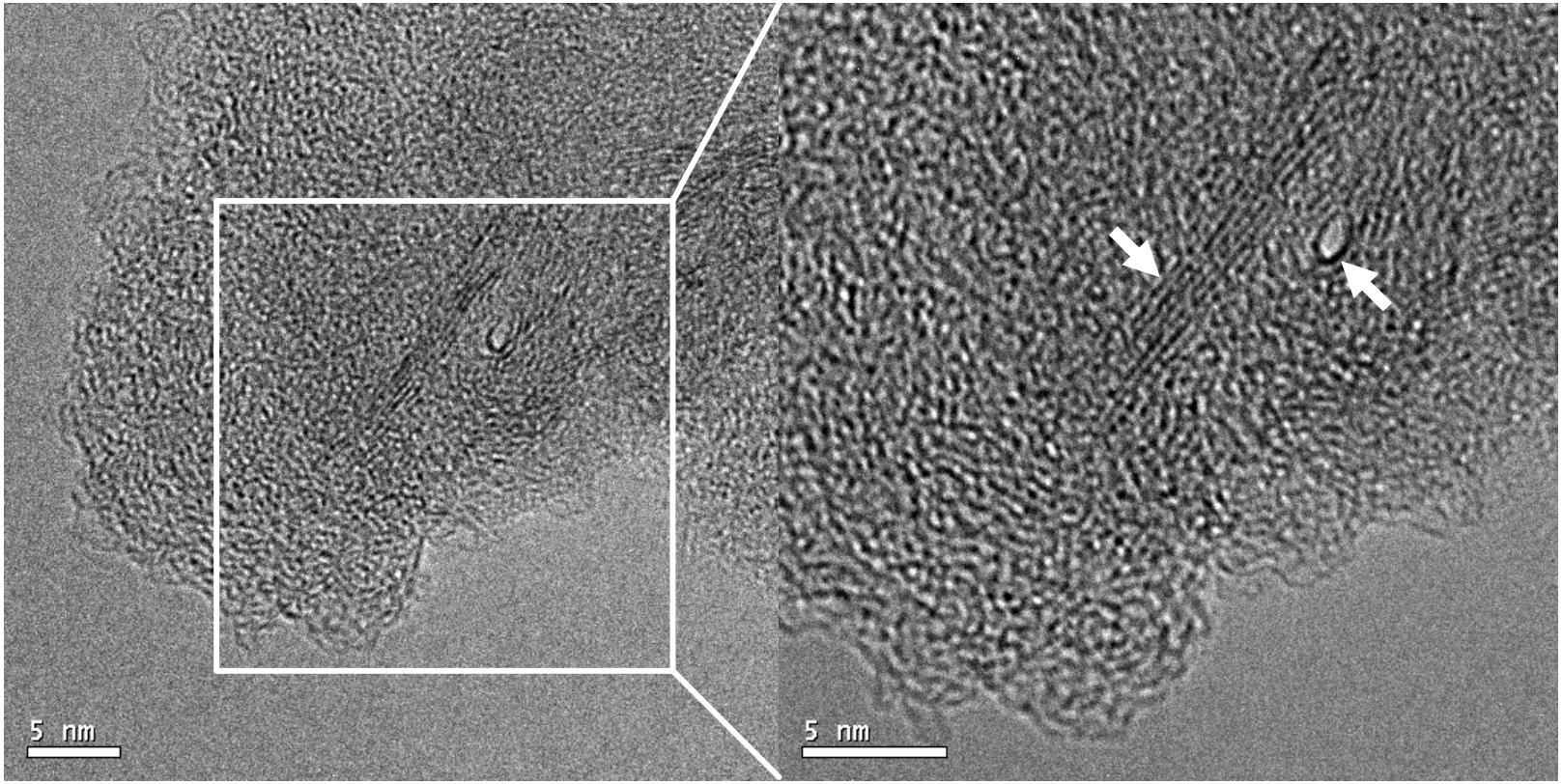

Figure **6.9** HRTEM image of SWNT/NPC nanocomposite carbon. The white arrows were pointed to the finite graphitic domain and the nanobulb from collapsed SWNTs.

The fracture strengths of NPC and SWNT/NPC nanocomposite fibers prepared at 600 °C or below are shown in figure **6.10**. With pyrolysis temperature increasing, the fibers were converted from polymer to carbon, and their fracture strength increased. The reinforcement effect of the SWNTs also increased with temperature. When the pyrolysis temperature was lower than 400 °C, the nanocomposite fibers had lower fracture strength than that of NPC. By 500 °C they had achieved the same strength as that of NPC and their fracture strength became higher than that of NPC at 600 °C. This indicated the expected enhancements due to inclusion of the SWNTs were recovered with increasing temperature.

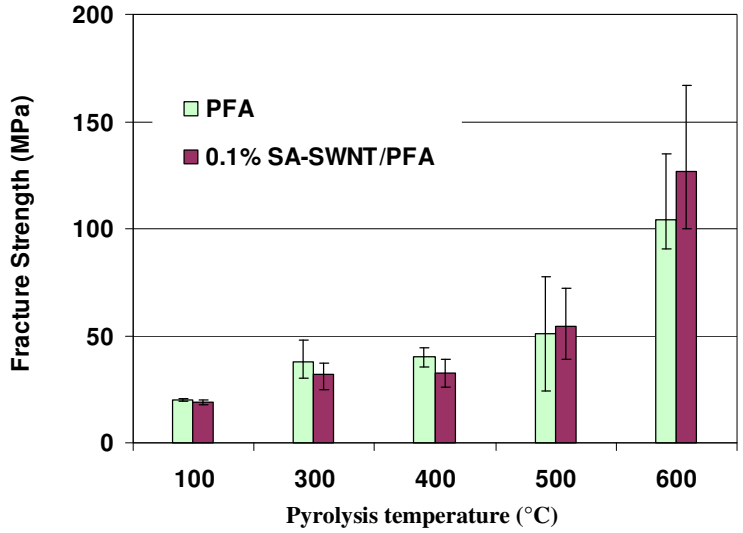

Figure **6.10** Fracture strength of PFA, SA-SWNT/PFA fibers cured at 100 °C, and NPC, SWNT/NPC nanocomposite fibers pyrolyzed at 300-600 °C.

According to the Halpin-Tsai's equation, in which the fibers are assumed to be uniformly distributed in the matrix, but not bonded with it, the tensile modulus of a composite with randomly oriented fibers can be approximated by [12]

$$\frac{Y_C}{V_f} \approx \left[\frac{3}{8}\eta_L(\zeta+1)+\frac{15}{8}\right]Y_m \qquad (\mathbf{6.1})$$

where Y_C is the modulus of the composite, Y_m is the matrix modulus, V_f is the volume percentage of fiber, ζ is the aspect ratio of the fiber $\zeta = 2l/D$, and

$$\eta_L = \frac{Y_f/Y_m - 1}{Y_f/Y_m + \zeta} \qquad (\mathbf{6.2})$$

Eq **6.1** is valid when the SWNT concentration is very low in the composites.

Assuming $Y_f \approx 500$ GPa for SWNT, and $Y_m \approx 2.5$ GPa for NPC, $\frac{Y_f}{Y_m}$ is ~200 and assuming that the SWNTs were isolated or in very thin bundles, that the average bundle diameter was ~4 nm, and that the SWNTs length was ~ 1μm with a ζ of ~500, then $\frac{Y_C}{V_f}\Big/Y_m$ is estimated to be ~55. Experimentally, the 0.1% SWNT/NPC was prepared from ~0.1 wt% SA-SWNT/FA. Counting in the addition of p-TSA/triton solution, the weight loss upon pyrolysis and the density difference between SWNT and NPC, V_f was ~ 0.16% thus $\frac{Y_C}{V_f}\Big/Y_m$ of the experiments was ~80 which is in good agreement with the estimated value derived by calculation. That the enhancement was slightly higher experimentally than the calculation based on the Halpin-Tsai's model, indicates that the SWNTs were well dispersed in the nanocomposite fibers as individual tubes or at least as very thin bundles. It also suggests that the interaction between SWNT and NPC strengthened the nanocomposite structure.

6.4 Summary and conclusions

SWNT/NPC nanocomposites with isolated SWNTs were prepared with SA-SWNT. The nanocomposite carbon had a significant higher mass transfer rate within it and the pore mouth mass transfer coefficient k_b increased by more than 2 times with addition only 0.05 wt% SWNT. Similar enhancements in mass transfer without surface functionalization of the SWNTs had required adding the SWNTs at concentrations of ~60 wt% in SWNT/NPC because these remained as SWNT bundles. These data show the extraordinary potential for structural modifications that can be achieved with low concentrations of the isolated SWNTs.

Assuming that the SWNTs were isolated or in a thin bundle, the Halpin-Tsai's equation gave the Young's moduli reinforcement just slightly lower than the actual experimental values, indicating that the dispersion of SA-SWNT in NPC matrix was very good and that there was strong interaction between the SWNTs and the NPC.

The enhancement in both the mass transfer rate and Young's modulus revealed the advantage of carefully preparing SWNT nanocomposites with rational the chemistry of surface functionalization, and by doing so we can see that the properties of host material can be greatly improved even with small levels of doping by the SWNTs.

Chapter 7

Summary and future work

In this thesis, the novel CC composites and nanocomposites with SWNT and NPC were prepared and characterized in order to investigate their structure properties and characteristics. The SWNT/NPC composites containing SWNT bundles showed higher mass transfer rates than PFA-NPC, but only at a very high concentration. The percolation threshold for these SWNT/NPC composites occurred at SWNT concentrations higher than 50 wt%. This was because the SWNTs were not well dispersed and most of them were confined into large bundles within the carbon matrix.

To improve matters, a PFA grafted SWNT (PFA-SWNT) was designed and synthesized with the intent of separating the tubes within the bundles and improving the compatibility of the SWNTs with the PFA. Intimate contact between NPC phase and surfaces of the individual SWNTs was found in the nanocomposite carbon formed by the pyrolysis of the PFA-SWNT. Characterization of the NPC/SWNT treated at 1200 – 2000 ºC indicated that there is a templating effect of SWNTs on NPC leading to local graphitization at the nanoscale even at low temperatures (>1400 ºC) thus confirming the

strong interaction between the two types of carbon.

Improvement in both gas adsorption properties and mechanical properties were obtained in the SWNT/NPC nanocomposites that were prepared from well dispersed, individual and functionalized SWNTs in FA. With only 0.05 wt% SWNTs in NPC, the nanocomposite had a mass transfer rate a factor of two times higher than that of NPC. To achieve a similar enhancement in rate using unfunctionalized SWNTs required as much as ~60 wt% SWNTs in a composite. This is because prior to functionalization the SWNTs are in bundles. The functionalization of the SWNTs successfully separated the bundles into individual tubes and much improved the dispersion of SWNTs in FA and in PFA. The Young's moduli of the SWNT/NPC nanocomposite fibers increased by a factor slightly higher than Halpin-Tsai's prediction, indicating that the strong interaction arising from the templating effect of SWNT strengthened the NPC matrix.

This work can be the beginning of several interesting future studies. Firstly, the strategies developed in this thesis can be used to prepare novel CC composites with SWNTs. Since SWNTs ideally have extraordinary mechanical and electronic properties with small size and low density, it is highly possible for them to replace carbon fibers in traditional CC composites. The functionalization of the SWNTs can lead to a new category of CC materials for further study and for future applications. This work has provided a way to prepare novel CC composites with SWNTs by doping them into the carbon precursor. Secondly, the processibility of SWNTs can be improved by functionalization. By designing the functional groups on SWNTs to be compatible with the host material, good dispersion and strong interaction between SWNT and the matrix can be obtained. This strategy can be extended to other of host materials, including

polymers, metals, etc. Thirdly, the integrity of the functionalized SWNTs can be recovered by heat treatment. Covalent functionalization is not always preferred in nanocomposite preparation because it disrupts the periodicity of walls of the SWNTs by creating defects, thereby diminishing their ideal properties, especially their electronic properties. However, it was found in this thesis that the integrity of SWNTs can be restored even at low temperature by pyrolysis, when they are embedded in a reactive carbon matrix. This provides a way to produce nanocomposites with high interaction between the SWNTs and the matrix while simultaneously rejuvenating the SWNTs. Fourthly, the SWNTs do have a templating effects on NPC graphitization at nanoscale with only low to medium temperature treatments. This phenomenon is quite interesting from the perspective of fundamental carbon science. Although PFA-NPC has been widely used for years, its structural evolution with temperature has not been fully understood. This study which shows conclusively the SWNT templating effect, may be helpful to understand to the structure and reactivity of the PFA-NPC. Additionally, the formation of an inter-phase between the SWNTs and the carbon matrix may enhance macroscopic mechanical properties of a composite by preventing or delaying the SWNTs from pulling out from the matrix. It will definitely be interesting to study novel CC composites made from functionalized SWNTs. Finally, the technique of probing the NPC structure with gas adsorption properties can be applied to other microporous materials. Much of the work on microporous materials is limited to measurements of surface area and pore size distribution (PSD). However, the rate of mass transfer and connectivity within the pore network are also very important factors controlling the behavior and performance of adsorbents, catalyst supports and membranes. Studies that combine mass

transfer properties with detailed PSD data lead to new insight that can result in the rational design and synthesis of new composites and nanocomposites containing SWNTs.

BIBLIOGRAPHY

1. Foley, H. C., Carbogenic Molecular-Sieves - Synthesis, Properties and Applications. *Microporous Materials* **1995,** 4, (6), 407-433.
2. Schmitt, J. L.; Walker, P. L., Carbon Molecular Sieve Supports for Metal Catalysts.1. Preparation of System-Platinum Supported on Polyfurfuryl Alcohol Carbon. *Carbon* **1971,** 9, (6), 791-796.
3. Schmitt, J. L.; Walker, P. L., Carbon Molecular-Sieve Supports for Metal Catalysts.2. Selective Hydrogenation of Hydrocarbons over Platinum Supported on Polyfurfuryl Alcohol Carbon. *Carbon* **1972,** 10, (1), 87-&.
4. Rajagopalan, R.; Ponnaiyan, A.; Mankidy, P. J.; Brooks, A. W.; Yi, B.; Foley, H. C., Molecular sieving platinum nanoparticle catalysts kinetically frozen in nanoporous carbon. *Chemical Communications* **2004**, (21), 2498-2499.
5. Shiflett, M. B.; Foley, H. C., Ultrasonic deposition of high-selectivity nanoporous carbon membranes. *Science* **1999,** 285, (5435), 1902-1905.
6. Rajagopalan, R.; Merritt, A.; Tseytlin, A.; Foley, H. C., Modification of macroporous stainless steel supports with silica nanoparticles for size selective carbon membranes with improved flux. *Carbon* **2006,** 44, (10), 2051-2058.
7. Li, J.; Wang, X. Y.; Huang, Q. H.; Gamboa, S.; Sebastian, P. J., Studies on preparation and performances of carbon aerogel electrodes for the application of supercapacitor. *Journal of Power Sources* **2006,** 158, (1), 784-788.
8. Jenkins, J. M. K., K., *Polymeric carbons - carbon fibre, glass and char*. Cambridge University Press: Cambridge, 1976.
9. Tans, S. J.; Devoret, M. H.; Dai, H. J.; Thess, A.; Smalley, R. E.; Geerligs, L. J.; Dekker, C., Individual single-wall carbon nanotubes as quantum wires. *Nature* **1997,** 386, (6624), 474-477.
10. Treacy, M. M. J.; Ebbesen, T. W.; Gibson, J. M., Exceptionally high Young's modulus observed for individual carbon nanotubes. *Nature* **1996,** 381, (6584), 678-680.
11. Thostenson, E. T.; Ren, Z. F.; Chou, T. W., Advances in the science and technology of carbon nanotubes and their composites: a review. *Composites Science and Technology* **2001,** 61, (13), 1899-1912.
12. Coleman, J. N.; Khan, U.; Blau, W. J.; Gun'ko, Y. K., Small but strong: A review of the mechanical properties of carbon nanotube-polymer composites. *Carbon* **2006,** 44, (9), 1624-1652.
13. Juntgen, H.; Knoblauch, K.; Harder, K., Carbon Molecular-Sieves - Production from Coal and Application in Gas Separation. *Fuel* **1981,** 60, (9), 817-822.
14. Sonobe, N.; Kyotani, T.; Tomita, A., Formation of Graphite Thin-Film from Polyfurfuryl Alcohol and Polyvinyl Acetate Carbons Prepared between the Lamellae of Montmorillonite. *Carbon* **1991,** 29, (1), 61-67.
15. Kyotani, T.; Yamada, H.; Sonobe, N.; Tomita, A., Heat-Treatment of Polyfurfuryl Alcohol Prepared between Taeniolite Lamellae. *Carbon* **1994,** 32, (4), 627-635.

16. Mariwala, R. K.; Foley, H. C., Evolution of Ultramicroporous Adsorptive Structure in Poly(Furfuryl Alcohol)-Derived Carbogenic Molecular-Sieves. *Industrial & Engineering Chemistry Research* **1994,** 33, (3), 607-615.
17. Acharya, M.; Strano, M. S.; Mathews, J. P.; Billinge, J. L.; Petkov, V.; Subramoney, S.; Foley, H. C., Simulation of nanoporous carbons: a chemically constrained structure. *Philosophical Magazine B-Physics of Condensed Matter Statistical Mechanics Electronic Optical and Magnetic Properties* **1999,** 79, (10), 1499-1518.
18. Mariwala, R. K.; Foley, H. C., Calculation of Micropore Sizes in Carbogenic Materials from the Methyl-Chloride Adsorption-Isotherm. *Industrial & Engineering Chemistry Research* **1994,** 33, (10), 2314-2321.
19. Smith, M. A.; Foley, H. C.; Lobo, R. F., A simple model describes the PDF of a non-graphitizing carbon. *Carbon* **2004,** 42, (10), 2041-2048.
20. Morenocastilla, C.; Mahajan, O. P.; Jung, H. J.; Vannice, M. A.; Walker, P. L., Carbon Catalyst Supports.1. Preparation and Character of Iron-Carbon Systems. *Carbon* **1980,** 18, (1), 49-49.
21. Stevens, M. G.; Foley, H. C., Alkali metals on nanoporous carbon: New solid-base catalysts. *Chemical Communications* **1997**, (6), 519-520.
22. Kane, M. S.; Kao, L. C.; Mariwala, R. K.; Hilscher, D. F.; Foley, H. C., Effect of porosity of carbogenic molecular sieve catalysts on ethylbenzene oxidative dehydrogenation. *Industrial & Engineering Chemistry Research* **1996,** 35, (10), 3319-3331.
23. Iijima, S., Helical Microtubules of Graphitic Carbon. *Nature* **1991,** 354, (6348), 56-58.
24. Iijima, S.; Ichihashi, T., Single-Shell Carbon Nanotubes of 1-Nm Diameter. *Nature* **1993,** 363, (6430), 603-605.
25. Bethune, D. S.; Kiang, C. H.; Devries, M. S.; Gorman, G.; Savoy, R.; Vazquez, J.; Beyers, R., Cobalt-Catalyzed Growth of Carbon Nanotubes with Single-Atomic-Layerwalls. *Nature* **1993,** 363, (6430), 605-607.
26. Oberlin, A.; Endo, M.; Koyama, T., Filamentous Growth of Carbon through Benzene Decomposition. *Journal of Crystal Growth* **1976,** 32, (3), 335-349.
27. Radushkevich, L. V. L., V. M., O strukture ugleroda, obrazujucegosja pri termiceskom razlozenii okisi ugleroda na zeleznomkontakte. *Zurn Fisic Chim* **1952,** 26, 88-95.
28. Lu, J. P., Elastic properties of single and multilayered nanotubes. *Journal of Physics and Chemistry of Solids* **1997,** 58, (11), 1649-1652.
29. Gao, G. H.; Cagin, T.; Goddard, W. A., Energetics, structure, mechanical and vibrational properties of single-walled carbon nanotubes. *Nanotechnology* **1998,** 9, (3), 184-191.
30. Popov, V. N.; Van Doren, V. E.; Balkanski, M., Elastic properties of single-walled carbon nanotubes. *Physical Review B* **2000,** 61, (4), 3078-3084.
31. Heer, W. A. d., Nanotubes and the Pursuit of Applications. *MRS Bulletin* **2004,** 29, (4), 281-285.
32. Dai, H. J., Carbon nanotubes: Synthesis, integrations, and properties. *Acc. Chem. Res.* **2002,** 35, (12), 1035-1044.
33. Samsonidze, G. G. S., R.; Kobayashi,N.; Gruneis,A.; Jiang,J.; Jorio,A. Chou,S. G.; Dresselhaus,G.; DresselhausM. S., Family behavior of the optical transition energies

in single-wall carbon nanotubes of smaller diameters. *Applied Physics Letters* **2004,** 85, (23), 5703-5705.
34. Dresselhaus, M. S. D., G.; Eklund, P. C., *Science of fullerenes and carbon nanotubes*. Academic Press: San Diego, 1996.
35. Dresselhaus, M. S.; Dresselhaus, G.; Saito, R.; Jorio, A., Raman spectroscopy of carbon nanotubes. *Physics Reports-Review Section of Physics Letters* **2005,** 409, (2), 47-99.
36. Berber, S.; Kwon, Y. K.; Tomanek, D., Unusually high thermal conductivity of carbon nanotubes. *Physical Review Letters* **2000,** 84, (20), 4613-4616.
37. Skoulidas, A. I.; Ackerman, D. M.; Johnson, J. K.; Sholl, D. S., Rapid transport of gases in carbon nanotubes. *Physical Review Letters* **2002,** 89, (18), -.
38. Ackerman, D. M.; Skoulidas, A. I.; Sholl, D. S.; Johnson, J. K., Diffusivities of Ar and Ne in carbon nanotubes. *Molecular Simulation* **2003,** 29, (10-11), 677-684.
39. Holt, J. K.; Park, H. G.; Wang, Y. M.; Stadermann, M.; Artyukhin, A. B.; Grigoropoulos, C. P.; Noy, A.; Bakajin, O., Fast mass transport through sub-2-nanometer carbon nanotubes. *Science* **2006,** 312, (5776), 1034-1037.
40. Journet, C.; Maser, W. K.; Bernier, P.; Loiseau, A.; delaChapelle, M. L.; Lefrant, S.; Deniard, P.; Lee, R.; Fischer, J. E., Large-scale production of single-walled carbon nanotubes by the electric-arc technique. *Nature* **1997,** 388, (6644), 756-758.
41. Thess, A.; Lee, R.; Nikolaev, P.; Dai, H. J.; Petit, P.; Robert, J.; Xu, C. H.; Lee, Y. H.; Kim, S. G.; Rinzler, A. G.; Colbert, D. T.; Scuseria, G. E.; Tomanek, D.; Fischer, J. E.; Smalley, R. E., Crystalline ropes of metallic carbon nanotubes. *Science* **1996,** 273, (5274), 483-487.
42. Nikolaev, P.; Bronikowski, M. J.; Bradley, R. K.; Rohmund, F.; Colbert, D. T.; Smith, K. A.; Smalley, R. E., Gas-phase catalytic growth of single-walled carbon nanotubes from carbon monoxide. *Chemical Physics Letters* **1999,** 313, (1-2), 91-97.
43. Girifalco, L. A.; Hodak, M.; Lee, R. S., Carbon nanotubes, buckyballs, ropes, and a universal graphitic potential. *Physical Review B* **2000,** 62, (19), 13104-13110.
44. O'Connell, M. J.; Boul, P.; Ericson, L. M.; Huffman, C.; Wang, Y. H.; Haroz, E.; Kuper, C.; Tour, J.; Ausman, K. D.; Smalley, R. E., Reversible water-solubilization of single-walled carbon nanotubes by polymer wrapping. *Chemical Physics Letters* **2001,** 342, (3-4), 265-271.
45. Buckley, J. D. E., D. D., *Carbon-carbon materials and composites*. Noyes Publications: Park Ridge, NJ, 1993.
46. Wagner, H. D.; Lourie, O.; Feldman, Y.; Tenne, R., Stress-induced fragmentation of multiwall carbon nanotubes in a polymer matrix. *Applied Physics Letters* **1998,** 72, (2), 188-190.
47. Andrews, R.; Jacques, D.; Rao, A. M.; Rantell, T.; Derbyshire, F.; Chen, Y.; Chen, J.; Haddon, R. C., Nanotube composite carbon fibers. *Applied Physics Letters* **1999,** 75, (9), 1329-1331.
48. Hishiyam.Y; Inagaki, M.; Kimura, S.; Yamadas, S., Graphitization of Carbon-Fiber - Glassy Carbon Composites. *Carbon* **1974,** 12, (3), 249-&.
49. Reiswig, R. D.; Levinson, L. S.; Orourke, J. A., Graphitisation of Polyfurfuryl Alcohol. *Carbon* **1968,** 6, (1), 124-&.
50. Morley, J. G., Fibrous composites with multiple and variable-shear-strength interfaces. *Composites* **1971**, (Jun), 80-84.

51. Shaffer, M. S. P.; Fan, X.; Windle, A. H., Dispersion and packing of carbon nanotubes. *Carbon* **1998,** 36, (11), 1603-1612.
52. Pirlot, C.; Willems, I.; Fonseca, A.; Nagy, J. B.; Delhalle, J., Preparation and characterization of carbon nanotube/polyacrylonitrile composites. *Advanced Engineering Materials* **2002,** 4, (3), 109-114.
53. Kymakis, E.; Amaratunga, G. A. J., Optical properties of polymer-nanotube composites. *Synthetic Metals* **2004,** 142, (1-3), 161-167.
54. Hwang, G. L.; Hwang, K. C., Carbon nanotube reinforced ceramics. *Journal of Materials Chemistry* **2001,** 11, (6), 1722-1725.
55. Kuzumaki, T.; Miyazawa, K.; Ichinose, H.; Ito, K., Processing of carbon nanotube reinforced aluminum composite. *Journal of Materials Research* **1998,** 13, (9), 2445-2449.
56. Dong, S. R.; Tu, J. P.; Zhang, X. B., An investigation of the sliding wear behavior of Cu-matrix composite reinforced by carbon nanotubes. *Materials Science and Engineering a-Structural Materials Properties Microstructure and Processing* **2001,** 313, (1-2), 83-87.
57. Jiang, L. Q.; Gao, L.; Sun, J., Production of aqueous colloidal dispersions of carbon nanotubes. *Journal of Colloid and Interface Science* **2003,** 260, (1), 89-94.
58. Kowbel, W.; Liu, H. L.; Tsou, H. T., Fiber-Matrix Interactions in Brittle Matrix Composites. *Metallurgical Transactions a-Physical Metallurgy and Materials Science* **1992,** 23, (4), 1051-1062.
59. Curran, S.; Davey, A. P.; Coleman, J.; Dalton, A.; McCarthy, B.; Maier, S.; Drury, A.; Gray, D.; Brennan, M.; Ryder, K.; de la Chapelle, M. L.; Journet, C.; Bernier, P.; Byrne, H. J.; Carroll, D.; Ajayan, P. M.; Lefrant, S.; Blau, W., Evolution and evaluation of the polymer nanotube composite. *Synthetic Metals* **1999,** 103, (1-3), 2559-2562.
60. Chang, T. E.; Kisliuk, A.; Rhodes, S. M.; Brittain, W. J.; Sokolov, A. P., Conductivity and mechanical properties of well-dispersed single-wall carbon nanotube/polystyrene composite. *Polymer* **2006,** 47, (22), 7740-7746.
61. Bahr, J. L.; Mickelson, E. T.; Bronikowski, M. J.; Smalley, R. E.; Tour, J. M., Dissolution of small diameter single-wall carbon nanotubes in organic solvents? *Chemical Communications* **2001**, (2), 193-194.
62. Haggenmueller, R.; Gommans, H. H.; Rinzler, A. G.; Fischer, J. E.; Winey, K. I., Aligned single-wall carbon nanotubes in composites by melt processing methods. *Chemical Physics Letters* **2000,** 330, (3-4), 219-225.
63. Park, C.; Ounaies, Z.; Watson, K. A.; Crooks, R. E.; Smith, J.; Lowther, S. E.; Connell, J. W.; Siochi, E. J.; Harrison, J. S.; Clair, T. L. S., Dispersion of single wall carbon nanotubes by in situ polymerization under sonication. *Chemical Physics Letters* **2002,** 364, (3-4), 303-308.
64. Jia, Z. J.; Wang, Z. Y.; Xu, C. L.; Liang, J.; Wei, B. Q.; Wu, D. H.; Zhu, S. W., Study on poly(methyl methacrylate)/carbon nanotube composites. *Materials Science and Engineering a-Structural Materials Properties Microstructure and Processing* **1999,** 271, (1-2), 395-400.
65. Kojima, Y.; Fukumori, K.; Usuki, A.; Okada, A.; Kurauchi, T., Gas Permeabilities in Rubber Clay Hybrid. *Journal of Materials Science Letters* **1993,** 12, (12), 889-890.

66. Kojima, Y.; Usuki, A.; Kawasumi, M.; Okada, A.; Fukushima, Y.; Kurauchi, T.; Kamigaito, O., Mechanical-Properties of Nylon 6-Clay Hybrid. *Journal of Materials Research* **1993,** 8, (5), 1185-1189.
67. Kojima, Y.; Usuki, A.; Kawasumi, M.; Okada, A.; Kurauchi, T.; Kamigaito, O., Sorption of Water in Nylon-6 Clay Hybrid. *Journal of Applied Polymer Science* **1993,** 49, (7), 1259-1264.
68. LeBaron, P. C.; Wang, Z.; Pinnavaia, T. J., Polymer-layered silicate nanocomposites: an overview. *Applied Clay Science* **1999,** 15, (1-2), 11-29.
69. Nakashima, N.; Tomonari, Y.; Murakami, H., Water-soluble single-walled carbon nanotubes via noncovalent sidewall-functionalization with a pyrene-carrying ammonium ion. *Chemistry Letters* **2002**, (6), 638-639.
70. O'Connell, M. J.; Bachilo, S. M.; Huffman, C. B.; Moore, V. C.; Strano, M. S.; Haroz, E. H.; Rialon, K. L.; Boul, P. J.; Noon, W. H.; Kittrell, C.; Ma, J. P.; Hauge, R. H.; Weisman, R. B.; Smalley, R. E., Band gap fluorescence from individual single-walled carbon nanotubes. *Science* **2002,** 297, (5581), 593-596.
71. Strano, M. S.; Moore, V. C.; Miller, M. K.; Allen, M. J.; Haroz, E. H.; Kittrell, C.; Hauge, R. H.; Smalley, R. E., The role of surfactant adsorption during ultrasonication in the dispersion of single-walled carbon nanotubes. *Journal of Nanoscience and Nanotechnology* **2003,** 3, (1-2), 81-86.
72. Star, A.; Steuerman, D. W.; Heath, J. R.; Stoddart, J. F., Starched carbon nanotubes. *Angewandte Chemie-International Edition* **2002,** 41, (14), 2508-+.
73. Bandyopadhyaya, R.; Nativ-Roth, E.; Regev, O.; Yerushalmi-Rozen, R., Stabilization of individual carbon nanotubes in aqueous solutions. *Nano Letters* **2002,** 2, (1), 25-28.
74. Sun, Y. P.; Fu, K. F.; Lin, Y.; Huang, W. J., Functionalized carbon nanotubes: Properties and applications. *Accounts of Chemical Research* **2002,** 35, (12), 1096-1104.
75. Huang, W. J.; Fernando, S.; Lin, Y.; Zhou, B.; Allard, L. F.; Sun, Y. P., Preferential solubilization of smaller single-walled carbon nanotubes in sequential functionalization reactions. *Langmuir* **2003,** 19, (17), 7084-7088.
76. Kim, U. J.; Furtado, C. A.; Liu, X. M.; Chen, G. G.; Eklund, P. C., Raman and IR spectroscopy of chemically processed single-walled carbon nanotubes. *Journal of the American Chemical Society* **2005,** 127, (44), 15437-15445.
77. Yang, C. W.; Hu, X. G.; Wang, D. L.; Dai, C. S.; Zhang, L.; Jin, H. B.; Agathopoulos, S., Ultrasonically treated multi-walled carbon nanotubes (MWCNTs) as PtRu catalyst supports for methanol electrooxidation. *Journal of Power Sources* **2006,** 160, (1), 187-193.
78. Mickelson, E. T.; Huffman, C. B.; Rinzler, A. G.; Smalley, R. E.; Hauge, R. H.; Margrave, J. L., Fluorination of single-wall carbon nanotubes. *Chemical Physics Letters* **1998,** 296, (1-2), 188-194.
79. Banerjee, S.; Wong, S. S., Functionalization of carbon nanotubes with a metal-containing molecular complex. *Nano Letters* **2002,** 2, (1), 49-53.
80. Holzinger, M.; Vostrowsky, O.; Hirsch, A.; Hennrich, F.; Kappes, M.; Weiss, R.; Jellen, F., Sidewall functionalization of carbon nanotubes. *Angewandte Chemie-International Edition* **2001,** 40, (21), 4002-+.
81. Kamaras, K.; Itkis, M. E.; Hu, H.; Zhao, B.; Haddon, R. C., Covalent bond formation to a carbon nanotube metal. *Science* **2003,** 301, (5639), 1501-1501.

82. Georgakilas, V.; Kordatos, K.; Prato, M.; Guldi, D. M.; Holzinger, M.; Hirsch, A., Organic functionalization of carbon nanotubes. *Journal of the American Chemical Society* **2002,** 124, (5), 760-761.
83. Coleman, K. S.; Bailey, S. R.; Fogden, S.; Green, M. L. H., Functionalization of single-walled carbon nanotubes via the Bingel reaction. *Journal of the American Chemical Society* **2003,** 125, (29), 8722-8723.
84. Dyke, C. A.; Tour, J. M., Unbundled and highly functionalized carbon nanotubes from aqueous reactions. *Nano Letters* **2003,** 3, (9), 1215-1218.
85. Dyke, C. A.; Tour, J. M., Solvent-free functionalization of carbon nanotubes. *Journal of the American Chemical Society* **2003,** 125, (5), 1156-1157.
86. Hudson, J. L.; Casavant, M. J.; Tour, J. M., Water-soluble, exfoliated, nonroping single-wall carbon nanotubes. *Journal of the American Chemical Society* **2004,** 126, (36), 11158-11159.
87. Bahr, J. L.; Yang, J. P.; Kosynkin, D. V.; Bronikowski, M. J.; Smalley, R. E.; Tour, J. M., Functionalization of carbon nanotubes by electrochemical reduction of aryl diazonium salts: A bucky paper electrode. *Journal of the American Chemical Society* **2001,** 123, (27), 6536-6542.
88. Price, B. K.; Hudson, J. L.; Tour, J. M., Green chemical functionalization of single-walled carbon nanotubes in ionic liquids. *Journal of the American Chemical Society* **2005,** 127, (42), 14867-14870.
89. Usrey, M. L.; Lippmann, E. S.; Strano, M. S., Evidence for a two-step mechanism in electronically selective single-walled carbon nanotube reactions. *Journal of the American Chemical Society* **2005,** 127, (46), 16129-16135.
90. Frankland, S. J. V.; Caglar, A.; Brenner, D. W.; Griebel, M., Molecular simulation of the influence of chemical cross-links on the shear strength of carbon nanotube-polymer interfaces. *Journal of Physical Chemistry B* **2002,** 106, (12), 3046-3048.
91. Geng, H. Z.; Rosen, R.; Zheng, B.; Shimoda, H.; Fleming, L.; Liu, J.; Zhou, O., Fabrication and properties of composites of poly(ethylene oxide) and functionalized carbon nanotubes. *Advanced Materials* **2002,** 14, (19), 1387-1390.
92. Gao, J. B.; Itkis, M. E.; Yu, A. P.; Bekyarova, E.; Zhao, B.; Haddon, R. C., Continuous spinning of a single-walled carbon nanotube-nylon composite fiber. *Journal of the American Chemical Society* **2005,** 127, (11), 3847-3854.
93. Dyke, C. A.; Tour, J. M., Covalent functionalization of single-walled carbon nanotubes for materials applications. *Journal of Physical Chemistry A* **2004,** 108, (51), 11151-11159.
94. Horvath, G.; Kawazoe, K., Method for the Calculation of Effective Pore-Size Distribution in Molecular-Sieve Carbon. *Journal of Chemical Engineering of Japan* **1983,** 16, (6), 470-475.
95. Srinivasan, R.; Auvil, S. R.; Schork, J. M., Mass-Transfer in Carbon Molecular-Sieves - an Interpretation of Langmuir Kinetics. *Chemical Engineering Journal and the Biochemical Engineering Journal* **1995,** 57, (2), 137-144.
96. Nguyen, C.; Do, D. D., Dual Langmuir kinetic model for adsorption in carbon molecular sieve materials. *Langmuir* **2000,** 16, (4), 1868-1873.
97. Fitzer, E.; Schafer, W., Effect of Crosslinking on Formation of Glasslike Carbons from Thermosetting Resins. *Carbon* **1970,** 8, (3), 353-&.

98. Crank, J., *The Mathematics of Diffusion*. Clarendon Press: Oxford, 1995.
99. Li, Z.; Yang, R. T., Concentration profile for linear driving force model for diffusion in a particle. *Aiche Journal* **1999,** 45, (1), 196-200.
100. Williams, D. B. C., C. B., *Transmission Electron Microscopy*. Plenum Press: New York, 1996.
101. Wittke, J. H., GLG 510 - Course Overview 2.1 Effects of Electron Bombardment, URL http://www4.nau.edu/microanalysis/Microprobe/Interact-Effects.html. In 2006.
102. Goldstein, J. I., *Scanning electron microscopy and X-ray microanalysis: a text for biologists, materials scientists, and geologists*. 2nd ed.; Plenum Press: New York, 1992; p 820.
103. Rafailov, P. M.; Jantoljak, H.; Thomsen, C., Electronic transitions in single-walled carbon nanotubes: A resonance Raman study. *Physical Review B* **2000,** 61, (23), 16179-16182.
104. Rao, A. M.; Richter, E.; Bandow, S.; Chase, B.; Eklund, P. C.; Williams, K. A.; Fang, S.; Subbaswamy, K. R.; Menon, M.; Thess, A.; Smalley, R. E.; Dresselhaus, G.; Dresselhaus, M. S., Diameter-selective Raman scattering from vibrational modes in carbon nanotubes. *Science* **1997,** 275, (5297), 187-191.
105. Pimenta, M. A.; Marucci, A.; Empedocles, S. A.; Bawendi, M. G.; Hanlon, E. B.; Rao, A. M.; Eklund, P. C.; Smalley, R. E.; Dresselhaus, G.; Dresselhaus, M. S., Raman modes of metallic carbon nanotubes. *Physical Review B* **1998,** 58, (24), 16016-16019.
106. Bandow, S.; Asaka, S.; Saito, Y.; Rao, A. M.; Grigorian, L.; Richter, E.; Eklund, P. C., Effect of the growth temperature on the diameter distribution and chirality of single-wall carbon nanotubes. *Physical Review Letters* **1998,** 80, (17), 3779-3782.
107. Henrard, L.; Hernandez, E.; Bernier, P.; Rubio, A., van der Waals interaction in nanotube bundles: Consequences on vibrational modes. *Physical Review B* **1999,** 60, (12), R8521-R8524.
108. Alvarez, L.; Righi, A.; Guillard, T.; Rols, S.; Anglaret, E.; Laplaze, D.; Sauvajol, J. L., Resonant Raman study of the structure and electronic properties of single-wall carbon nanotubes. *Chemical Physics Letters* **2000,** 316, (3-4), 186-190.
109. Venkateswaran, U. D.; Rao, A. M.; Richter, E.; Menon, M.; Rinzler, A.; Smalley, R. E.; Eklund, P. C., Probing the single-wall carbon nanotube bundle: Raman scattering under high pressure. *Physical Review B* **1999,** 59, (16), 10928-10934.
110. Rao, A. M.; Chen, J.; Richter, E.; Schlecht, U.; Eklund, P. C.; Haddon, R. C.; Venkateswaran, U. D.; Kwon, Y. K.; Tomanek, D., Effect of van der Waals interactions on the Raman modes in single walled carbon nanotubes. *Physical Review Letters* **2001,** 86, (17), 3895-3898.
111. Kataura, H.; Kumazawa, Y.; Maniwa, Y.; Umezu, I.; Suzuki, S.; Ohtsuka, Y.; Achiba, Y., Optical properties of single-wall carbon nanotubes. *Synthetic Metals* **1999,** 103, (1-3), 2555-2558.
112. Strano, M. S., Probing chiral selective reactions using a revised Kataura plot for the interpretation of single-walled carbon nanotube spectroscopy. *Journal of the American Chemical Society* **2003,** 125, (51), 16148-16153.
113. Wang, Y.; Alsmeyer, D. C.; Mccreery, R. L., Raman-Spectroscopy of Carbon Materials - Structural Basis of Observed Spectra. *Chemistry of Materials* **1990,** 2, (5), 557-563.
114. Kurti, J.; Zolyomi, V.; Gruneis, A.; Kuzmany, H., Double resonant Raman

phenomena enhanced by van Hove singularities in single-wall carbon nanotubes. *Phys Rev B* **2002,** 65, 165433 (1-9).
115. Eklund, P. C.; Holden, J. M.; Jishi, R. A., Vibrational-Modes of Carbon Nanotubes - Spectroscopy and Theory. *Carbon* **1995,** 33, (7), 959-972.
116. Tuinstra, F.; Koenig, J. L., Raman Spectrum of Graphite. *Journal of Chemical Physics* **1970,** 53, (3), 1126-&.
117. Ferrari, A. C.; Robertson, J., Resonant Raman spectroscopy of disordered, amorphous, and diamondlike carbon. *Physical Review B* **2001,** 64, (7), -.
118. Calbi, M. M.; Cole, M. W.; Gatica, S. M.; Bojan, M. J.; Stan, G., Colloquium: Condensed phases of gases inside nanotube bundles. *Reviews of Modern Physics* **2001,** 73, (4), 857-865.
119. Saito, A.; Foley, H. C., Curvature and Parametric Sensitivity in Models for Adsorption in Micropores. *Aiche Journal* **1991,** 37, (3), 429-436.
120. Talapatra, S.; Zambano, A. Z.; Weber, S. E.; Migone, A. D., Gases do not adsorb on the interstitial channels of closed-ended single-walled carbon nanotube bundles. *Physical Review Letters* **2000,** 85, (1), 138-141.
121. Stan, G.; Bojan, M. J.; Curtarolo, S.; Gatica, S. M.; Cole, M. W., Uptake of gases in bundles of carbon nanotubes. *Physical Review B* **2000,** 62, (3), 2173-2180.
122. Stephan, C.; Nguyen, T. P.; de la Chapelle, M. L.; Lefrant, S.; Journet, C.; Bernier, P., Characterization of singlewalled carbon nanotubes-PMMA composites. *Synthetic Metals* **2000,** 108, (2), 139-149.
123. Feng, W.; Bai, X. D.; Lian, Y. Q.; Liang, J.; Wang, X. G.; Yoshino, K., Well-aligned polyaniline/carbon-nanotube composite films grown by in-situ aniline polymerization. *Carbon* **2003,** 41, (8), 1551-1557.
124. Tang, B. Z.; Xu, H. Y., Preparation, alignment, and optical properties of soluble poly(phenylacetylene)-wrapped carbon nanotubes. *Macromolecules* **1999,** 32, (8), 2569-2576.
125. Lin, Y.; Zhou, B.; Fernando, K. A. S.; Liu, P.; Allard, L. F.; Sun, Y. P., Polymeric carbon nanocomposites from carbon nanotubes functionalized with matrix polymer. *Macromolecules* **2003,** 36, (19), 7199-7204.
126. Hill, D. E.; Lin, Y.; Rao, A. M.; Allard, L. F.; Sun, Y. P., Functionalization of carbon nanotubes with polystyrene. *Macromolecules* **2002,** 35, (25), 9466-9471.
127. Yao, Z. L.; Braidy, N.; Botton, G. A.; Adronov, A., Polymerization from the surface of single-walled carbon nanotubes - Preparation and characterization of nanocomposites. *Journal of the American Chemical Society* **2003,** 125, (51), 16015-16024.
128. Li, H. M.; Cheng, F. O.; Duft, A. M.; Adronov, A., Functionalization of single-walled carbon nanotubes with well-defined polystyrene by "click" coupling. *Journal of the American Chemical Society* **2005,** 127, (41), 14518-14524.
129. Buffa, F.; Hu, H.; Resasco, D. E., Side-wall functionalization of single-walled carbon nanotubes with 4-hydroxymethylaniline followed by polymerization of epsilon-caprolactone. *Macromolecules* **2005,** 38, (20), 8258-8263.
130. Choura, M.; Belgacem, N. M.; Gandini, A., Acid-catalyzed polycondensation of furfuryl alcohol: Mechanisms of chromophore formation and cross-linking. *Macromolecules* **1996,** 29, (11), 3839-3850.
131. Principe, M.; Ortiz, P.; Martinez, R., An NMR study of poly(furfuryl alcohol)

prepared with p-toluenesulphonic acid. *Polymer International* **1999,** 48, (8), 637-641.
132. Davis, V. A.; Ericson, L. M.; Parra-Vasquez, A. N. G.; Fan, H.; Wang, Y. H.; Prieto, V.; Longoria, J. A.; Ramesh, S.; Saini, R. K.; Kittrell, C.; Billups, W. E.; Adams, W. W.; Hauge, R. H.; Smalley, R. E.; Pasquali, M., Phase Behavior and rheology of SWNTs in superacids. *Macromolecules* **2004,** 37, (1), 154-160.
133. Richter, E.; Subbaswamy, K. R., Theory of size-dependent resonance Raman scattering from carbon nanotubes. *Physical Review Letters* **1997,** 79, (14), 2738-2741.
134. Strano, M. S.; Dyke, C. A.; Usrey, M. L.; Barone, P. W.; Allen, M. J.; Shan, H. W.; Kittrell, C.; Hauge, R. H.; Tour, J. M.; Smalley, R. E., Electronic structure control of single-walled carbon nanotube functionalization. *Science* **2003,** 301, (5639), 1519-1522.
135. Saito, Y.; Hata, K.; Takakura, A.; Yotani, J.; Uemura, S., Field emission of carbon nanotubes and its application as electron sources of ultra-high luminance light-source devices. *Physica B-Condensed Matter* **2002,** 323, (1-4), 30-37.
136. Jorio, A.; Saito, R.; Hafner, J. H.; Lieber, C. M.; Hunter, M.; McClure, T.; Dresselhaus, G.; Dresselhaus, M. S., Structural (n, m) determination of isolated single-wall carbon nanotubes by resonant Raman scattering. *Physical Review Letters* **2001,** 86, (6), 1118-1121.
137. Nikolaev, P.; Thess, A.; Rinzler, A. G.; Colbert, D. T.; Smalley, R. E., Diameter doubling of single-wall nanotubes. *Chemical Physics Letters* **1997,** 266, (5-6), 422-426.
138. Fang, S. L.; Rao, A. M.; Eklund, P. C.; Nikolaev, P.; Rinzler, A. G.; Smalley, R. E., Raman scattering study of coalesced single walled carbon nanotubes. *Journal of Materials Research* **1998,** 13, (9), 2405-2411.
139. Yudasaka, M.; Ichihashi, T.; Kasuya, D.; Kataura, H.; Iijima, S., Structure changes of single-wall carbon nanotubes and single-wall carbon nanohorns caused by heat treatment. *Carbon* **2003,** 41, (6), 1273-1280.
140. Metenier, K.; Bonnamy, S.; Beguin, F.; Journet, C.; Bernier, P.; de La Chapelle, M. L.; Chauvet, O.; Lefrant, S., Coalescence of single-walled carbon nanotubes and formation of multi-walled carbon nanotubes under high-temperature treatments. *Carbon* **2002,** 40, (10), 1765-1773.
141. Kim, U. J.; Gutierrez, H. R.; Kim, J. P.; Eklund, P. C., Effect of the tube diameter distribution on the high-temperature structural modification of bundled single-walled carbon nanotubes. *Journal of Physical Chemistry B* **2005,** 109, (49), 23358-23365.
142. Kim, Y. A.; Muramatsu, H.; Hayashi, T.; Endo, M.; Terrones, M.; Dresselhaus, M. S., Thermal stability and structural changes of double-walled carbon nanotubes by heat treatment. *Chemical Physics Letters* **2004,** 398, (1-3), 87-92.
143. Gutierrez, H. R.; Kim, U. J.; Kim, J. P.; Eklund, P. C., Thermal conversion of bundled carbon nanotubes into graphitic ribbons. *Nano Letters* **2005,** 5, (11), 2195-2201.
144. Lopez, M. J.; Rubio, A.; Alonso, J. A., Deformations and thermal stability of carbon nanotube ropes. *Ieee Transactions on Nanotechnology* **2004,** 3, (2), 230-236.
145. Ruoff, R. S.; Tersoff, J.; Lorents, D. C.; Subramoney, S.; Chan, B., Radial Deformation of Carbon Nanotubes by Van-Der-Waals Forces. *Nature* **1993,** 364, (6437), 514-516.
146. Qian, D.; Dickey, E. C.; Andrews, R.; Rantell, T., Load transfer and deformation mechanisms in carbon nanotube-polystyrene composites. *Applied Physics Letters* **2000,** 76, (20), 2868-2870.
147. Barber, A. H.; Cohen, S. R.; Wagner, H. D., Measurement of carbon nanotube-

polymer interfacial strength. *Applied Physics Letters* **2003,** 82, (23), 4140-4142.
148. Yi, B.; Rajagopalan, R.; Foley, H. C.; Kim, U. J.; Liu, X. M.; Eklund, P. C., Catalytic polymerization and facile grafting of poly(furfuryl alcohol) to single-wall carbon nanotube: Preparation of nanocomposite carbon. *Journal of the American Chemical Society* **2006,** 128, (34), 11307-11313.
149. Hishiyam.Y; Yamada, S., Graphitization of Carbon-Fiber and Glassy Carbon Composite. *Carbon* **1973,** 11, (6), 689-689.
150. Rellick, G. S.; Chang, D. J.; Zaldivar, R. J., Mechanisms of Orientation and Graphitization of Hard-Carbon Matrices in Carbon Carbon Composites. *Journal of Materials Research* **1992,** 7, (10), 2798-2809.
151. Kamiya, K.; Inagaki, M., Thermal-Expansion of Natural Graphite Imbedded in Glassy Carbon. *Carbon* **1973,** 11, (4), 429-430.
152. Merlen, A.; Toulemonde, P.; Bendiab, N.; Aouizerat, A.; Sauvajol, J. L.; Montagnac, G.; Cardon, H.; Petit, P.; San Miguel, A., Raman spectroscopy of open-ended Single Wall Carbon Nanotubes under pressure: effect of the pressure transmitting medium. *Physica Status Solidi B-Basic Solid State Physics* **2006,** 243, (3), 690-699.
153. Katagiri, G.; Ishida, H.; Ishitani, A., Raman-Spectra of Graphite Edge Planes. *Carbon* **1988,** 26, (4), 565-571.
154. Kasuya, A.; Sasaki, Y.; Saito, Y.; Tohji, K.; Nishina, Y., Evidence for size-dependent discrete dispersions in single-wall nanotubes. *Physical Review Letters* **1997,** 78, (23), 4434-4437.
155. Moniruzzaman, M.; Winey, K. I., Polymer nanocomposites containing carbon nanotubes. *Macromolecules* **2006,** 39, (16), 5194-5205.
156. Pichot, V.; Badaire, S.; Albouy, P. A.; Zakri, C.; Poulin, P.; Launois, P., Structural and mechanical properties of single-wall carbon nanotube fibers. *Physical Review B* **2006,** 74, (24), -.
157. Lau, K. T.; Gu, C.; Hui, D., A critical review on nanotube and nanotube/nanoclay related polymer composite materials. *Composites Part B-Engineering* **2006,** 37, (6), 425-436.

VITA

Bo Yi

Education

- Aug. 2001- present Ph.D candidate in Pennsylvania State University
- May. 2001 M.S in Department of Chemical Engineering in Tsinghua University, Beijing, China.
- May. 1998 B.E in Department of Chemical Engineering in Tsinghua University, Beijing, China.

Awards and Honors

- Academic Excellence Fellowship in Chemical Engineering, Penn State University (2001).
- Graduate School Fellowship of Penn State University (2001)
- Excellent Student Fellowship, Tsinghua University, 1994 – 1997, 2002.

Publications

- B. Yi, R. Rajagopalan, H. C. Foley, U. J. Kim, X. Liu, and P. C. Eklund, "Catalytic Polymerization and Facile Grafting of Poly(furfuryl alcohol) to Single-Wall Carbon Nanotube: Preparation of Nanocomposite Carbon" J. Am. Chem. Soc. 2006, 128(34) 11307 – 11313.
- B. Yi, R. Rajagopalan, C. L. Burket, H. C. Foley, X. Liu, and P. C. Eklund, "Deformation of Nanoporous Carbon/Single-Wall Carbon Nanotube nanocomposite at high temperature" submitted.
- B.A. Samuel, M. A. Haque, B. Yi, R. Rajagopalan, H. C. Foley, "Mechanical Testing of Pyrolyzed Poly(furfuryl alcohol) Nanofibers" Nanotechnology 2007, 18, 115704 (8pp).
- R. Rajagopalan, A. Ponnaiyan, P. J. Mankidy, A. W. Brooks, B. Yi and H. C. Foley "Molecular sieving platinum nanoparticle catalysts kinetically frozen in nanoporous carbon" Chemical communications 2004, 21, 2498-2499.
- Y. Gogotsi, A. Nikitin, H. Ye, W. Zhou, J. E. Fischer, B. Yi, H. C. Foley and M. W. Barsoum, "Nanoporous carbide-derived carbon with tunable pore size" Nature materials 2003, 2(9), 591-594.